DEVELOPMENT AND APPLICATION OF ADJOINT TOOLS FOR THE WRF MODEL: A CASE STUDY OF HURRICANE IRMA (2017)

by
Zhaoxiangrui He

A thesis submitted in partial fulfillment of
the requirements for the degree of

Master of Science
(Atmospheric and Oceanic Sciences)

at the
UNIVERSITY OF WISCONSIN – MADISON
2018

Approved by:_____

Michael C. Morgan

Professor, Department of Atmospheric and Oceanic Sciences

Date:_____

Abstract

While tropical cyclones (TCs) are among the most dangerous and devastating natural hazards, TC intensity forecasts remain a particularly challenging problem in tropical weather prediction. To reduce deaths and damages caused by TCs, it is beneficial to gain greater understanding of the factors that govern TCs intensity and intensity tendency. In this study, the forward and adjoint of a numerical weather prediction model are used to assess the sensitivities of intensity to kinematic and thermodynamic variables. Specifically, this study will reveal how changes in horizontal wind, potential temperature, and water vapor mixing ratio distributions at the initial time of a 24h TC simulation influence TC simulated intensity. These sensitivities of intensity are used to construct optimal perturbations to the simulations. The consequences of these perturbations to the TC simulation are evaluated and described.

In the sensitivity study, the Weather Research and Forecast (WRF) forward model and WRFPLUS adjoint model are used to study initial condition sensitivities of the intensity forecast of Atlantic Hurricane Irma (2017) for three 24h periods beginning 0000 UTC on 05, 09, and 10 September 2017. Sensitivities to horizontal winds show that a stronger primary circulation in the rainband regions associated with cyclonic vorticity spiraling back against the vortex flow would enhance the intensity of hurricane. The results further suggest that a stronger secondary circulation, at the initial time, would not lead to a more intense hurricane 24h later. Sensitivities to temperature and water vapor mixing ratio suggest that an increase of equivalent potential temperature throughout the depth of the troposphere in the eye, and in the rainband regions from lower- to mid-troposphere could intensify the hurricane. This is presumed to be a consequence of the fact that sensible and latent heating in the eye would decrease the downdraft thus decrease the central pressure; sensible and latent heating in the rainband region would enhance the convection and the inflow above the boundary layer. Mid-level entrainment and low-level transport of high-entropy air within the eye to the eyewall could enhance convection in the eyewall; transport of rainband air of increased entropy and higher angular momentum from the rainband to the eyewall by the enhanced inflow could enhance convection in the eyewall and spin up the primary circulation in the rainband regions. The sensitivities in the eyewall region are small, because the air is already warm and saturated in that region.

Optimal perturbations, perturbations designed to elicit a specific change in the final time intensity utilizing minimum initial energy, were introduced to the initial conditions of the nonlinear simulations and a comparison of the outputs of the control and perturbed simulations was performed. It was found that the intensified (weakened) cyclone shifts southward (northward) along the track of the control cyclone. Secondly, the evolved initial optimal perturbations rotate cyclonically around the control TC with the period of 48h as a wave number one disturbance, similar to a vortex Rossby wave. For this case, perturbations to horizontal winds are more influential than perturbations of temperature and water vapor mixing ratio for changes of TC intensity; perturbations to a weakening hurricane behave more linearly than those designed to intensify it. Furthermore, perturbations of horizontal winds and potential temperature, as well as total energy of optimal perturbations propagate upward during the simulation periods.

Acknowledgements

I would first like to thank my thesis advisor Prof. Morgan. The door to Prof. Morgan office was always open whenever I ran into a trouble spot or had a question about my research or writing. He consistently and patiently allowed this paper to be my own work, but steered me in the right the direction whenever he thought I needed it.

Next, my thanks go to the entire AOS department faculty. Specifically, I would like to thank Prof. Martin and Dr. Hoover. I am gratefully indebted to them for their very valuable intuition and advice for the research, as well as comments on this thesis. Furthermore, Prof. Liu helped me getting used to the life in Madison and showed me the fun and taste of science.

I would also like to thank my friends in the AOS department. Coda Phillips for his patient and careful help in Python programming; Craig Oswald and Zoe Brooke-Zibton for their discussion and help in using adjoint model and GEMPAK; Dee VanRuyven for her patient and considerate suggestions about graduate student academics; Pete Pokrandt for his assistance in computer and the Internet.

Finally, I must express my very profound gratitude to family for providing me with unfailing support and continuous encouragement throughout my years of study and through the process of researching and writing this thesis. This accomplishment would not have been possible without them. Thank you.

Table of Contents

1. Introduction

a. Tropical cyclones

1) DEFINITIONS AND IMPACTS

A tropical cyclone (TC) is warm-core, non-frontal, synoptic-scale cyclone, originating over tropical or subtropical waters, with organized deep convection and a closed surface wind circulation about a well-defined center (United States National Hurricane Center, NHC). The term hurricane is used for Northern Hemisphere TCs east of the International Dateline to the Greenwich Meridian with maximum sustained surface wind (using the U.S. 1-minute average) of 64 kt (119 kmh^{-1}) or more (Hart, 2006). It is observed that most intense Atlantic hurricanes occur typically during August to October and are formed from African easterly waves. Understanding TC dynamics and improving TC forecast skill are important research foci since TCs bring annually considerable loss of life, property damage, and disruption of commerce. Pielke et al. (2008) estimates that annual damage of hurricanes is about $10 billion. Improvement in forecast intensity and track could mitigate social disruption and economic impact as evacuations could be more targeted, recovery efforts better staged prior to TC impacts, and property better secured.

2) TC PREDICTABILITY

Tropical cyclone track forecasts have seen considerable improvement over the last few decades while intensity forecasts remain a longstanding challenge with only modest improvement over a similar time interval. Indeed, in the latest annual NHC verification report (Cangialosi, 2018), the mean NHC official track forecast errors in the Atlantic basin for the 2017 hurricane season were smaller than the previous 5-yr means at all forecast times and the 2017 official track forecasts set records for track accuracy at all forecast times. Intensity forecasts errors, on the other hand, were higher than the 2016 values from 24 to 72 h, but decreased at the 96- and 120-h forecast times. Cangialosi (2018) notes that despite interannual variability of intensity forecast errors, there has been a notable decrease in such errors over the last seven years, with forecasts in the current decade being more skillful than those of the last decade. An even more vexing forecast challenge has been TC rapid intensification (RI) defined as an increase in the maximum sustained winds of a TC of at least $15ms^{-1}$ in a 24h period. Intensity change is the focus of the present research.

While it is now widely understood that the maximum potential intensity (MPI) of long-lasting TCs is controlled mostly by environmental thermodynamic conditions (*e.g.*, Emanuel 1986; Emanuel 1988; DeMaria and Kaplan 1994), TC intensification is believed to be governed by complex physical and dynamical processes (Judt and Chen 2016; hereafter JCB16) affected by multiscale interactions between the TC environment, the mean TC vortex, and internal convective processes (*e.g.*, Rogers 2010; Guimond et al. 2010; Rogers et al. 2015). The predictability of TC intensity and intensity change is dependent in part, on whether intensification is controlled to a greater extent by environmental or internal processes. For instance, a recent TC predictability study showed that the mean TC vortex and the wavenumber 1 asymmetry, which are predominantly controlled by the TC environment, are predictable for much longer (7 days) than small-scale structures, which are controlled by internal convective processes with predictability limits of 12h (JCB16). JCB16 also found that the highest forecast uncertainty occurs during RI.

3) TC STRUCTURE

A tropical cyclone has three conspicuous regions: the eye, the eyewall, and its (spiral) rainbands; and two well-developed wind patterns: a horizontal, primary (tangential wind) circulation and a secondary "in-up-and-out", thermally direct, radial-vertical circulation. The eye is a warm and nearly calm wind region near the cyclone center. In well-developed TCs the eye is manifest as a clear, or nearly clear region on visible satellite imagery and as a local maximum in brightness temperature on infrared imagery. The eye is associated with weak subsidence. The eyewall is a ring of intense, outwardly and upwardly sloping convection some tens of kilometers from the cyclone center where the strongest, cyclonic, tangential winds are found. The primary (*i.e.* azimuthal) circulation is strongest in the eyewall regions, and decreases with radius and height. The TC primary circulation can extend hundreds of kilometers from the eye and diminishes with height in accord with thermal wind balance for a gradient wind, hydrostatic warm-core vortex. In fact, the TC primary circulation becomes anticyclonic near the tropopause (about 15 km above the surface) beyond 200 km radius, which is due to the loss of angular momentum in the low-level inflow (Smith 2006). The secondary circulation is characterized by a low- and mid-level inflow, and upper-level outflow and represents the response to both diabatic heating and momentum forcing, including surface

friction. The secondary circulation transports high absolute angular momentum inward to spin-up the TC primary circulation. Air spirals into the storm at low levels with much of the inflow in the boundary layer 0.5-1 km deep. Air spirals out at upper levels 5-100 km from the center (Smith 2006). At larger radii from the cyclone center, there are spiral bands of convective cloud referred to as spiral (rain) bands. Despite their presence in most TCs, these spiral bands remain enigmatic features of tropical cyclones to the present date with many extant theories on their formation.

Malkus (1958) proposed a model of the TC eye which assumes that the air within the eye comes from the eyewall at upper-levels, descends with exchange of properties (*e.g.*, acquires angular momentum) through the mid-levels, and flows out at lower-levels. Since the low-level outflow has large angular momentum, low-level divergence increases. This process further maintains the upper-level descent and associated compressional warming of the eye. The low-level divergence and the surface friction make the wind speed in the eye small. Riehl and Malkus (1961) found that the eyewall consists of "hot towers", which transport moist, warm air upward in the inner core, and while covering only a small fraction of the eyewall contribute ultimately to the most vertical mass and heat flux in the tropical cyclone. Hot towers together with oceanic heat source in the eyewall produce a large, outward-directed, horizontal pressure gradient.

4) TC INTENSITY AND INTENSITY CHANGE

Six environmental conditions favorable for tropical cyclone formation were identified by Gray (1975):

1. large lower-tropospheric relative vorticity,
2. a location sufficiently removed poleward of the equator to provide a significant value of planetary vorticity;
3. relatively weak vertical wind shear (less than 5 ms^{-1} between 500 and 200 hPa);
4. sea surface temperature is greater than 26°C down to a depth of 60 m;
5. conditional instability between the surface and the 500 hPa level; and
6. large values of lower-to-middle tropospheric relative humidity

While Gray's focus was on tropical *cyclogenesis* (as opposed to the intensity change of an already existing TC), for existing TCs, conditions (3) – (6) are considered key by operational forecasters for identifying environments favorable for existing TCs to further intensify.

Sea surface temperature (SST) is perhaps the most obvious factor governing TC intensity and intensity change: Bender and Ginis (2000) found that a decrease of SST induced by Ekman upwelling underneath the TC circulation could be detrimental to TC intensity for slow moving TCs. Further, SST cooling could slow the deepening rate of TCs. In addition, Bender and Ginis (2000) found that use of a coupled model was able to improve the intensity forecasts.

While it has been recognized that sea surface temperature (SST) plays a role in the formation and intensification of TCs (Palmén 1948; Miller 1958), SST alone is not a good predictor of whether a specific TC will undergo intensification (Demaria and Kaplan, 1994). The ultimate energy source of tropical cyclones is the thermodynamic disequilibrium of the tropical ocean and the overlying tropical atmosphere. Riehl (1954) was among the first to describe TCs as heat engines and showed that for air ascending in the eyewall to be warmer than that of the far environment (a condition for conversion of potential to kinetic energy) the inflowing air had to acquire enthalpy from the underlying sea surface. Malkus and Riehl (1960) developed a model of inflow layer air spiraling into the steady-state TC near the ocean surface. They found that transfer of the sensible and latent heat from the ocean to the atmosphere in the core determines the pressure gradient along the trajectory, such that changes of moist entropy (θ_e) and changes the surface pressure (p_s) satisfy: $-\delta p_s = 2.5\delta\theta_e$.

Tropical cyclone energetics have been idealized more recently as those of a Carnot heat engine (Fig. 1.1). As such, the thermal efficiency of a TC depends on sea surface temperature (SST, heat source temperature) and mean (upper-tropospheric) outflow temperature (heat sink temperature). The most important assumption is that boundary-layer air parcels are conditionally neutral to displacement along the angular momentum surfaces of the TC. Therefore, the thermodynamics are reversible. In this Carnot idealization, air parcels acquire heat through fluxes of sensible and latent heat along an inflow, expansion leg (B) that is assumed to be isothermal. During this expansion, air parcels are losing angular momentum due to surface friction. The air parcels then ascend moist adiabatically within the eyewall and flare

outward along nearly congruent moist adiabats and angular momentum surfaces (C). At large radii it is assumed that air parcels lose enough heat through radiative cooling (D) to return to their ambient θ_e value and that angular momentum is restored. The cycle is closed during an assumed adiabatic compression leg (A) along an absolute vortex surface (angular momentum surface). The work done by the heat engine is assumed to be converted into kinetic energy that is dissipated ultimately in the frictional boundary layer. As a consequence, this thermodynamic cycle is linked to the boundary layer wind field (Riemer et al. 2010).

Using this Carnot cycle idealization, Emanuel (1988) derived a formula of maximum potential intensity (MPI). In his derivation, he applied Bernoulli's principle and assumed pseudo-adiabatic processes in deep convection within the eyewall and the outflows, then integrated the energy along the streamlines (*i.e.*, absolute vortex lines). Two additional assumptions were also used, the first is that there is no radial temperature gradient in the atmospheric mixed layer; the second is that no dissipation occurs except within the inflow (*i.e.*, surface friction) and at large radii in the outflow. Further modifications of Emanuel's model include effects of a subcloud-layer (Emanuel 1995a), surface exchange coefficients (Emanuel 1995b), and dissipative heating (Bister and Emanuel 1998). Emanuel (1999) provided a formula of thermal efficiency in terms of maximum wind speed, exchange coefficients of enthalpy and momentum, and difference of specific enthalpies of air at saturation at sea surface and ambient boundary layer. The formula for TC maximum potential intensity of hurricane gives a quantitative expression for the maximum intensity of TCs given the thermodynamic states of both the environment and the underlying sea. While there are competing approaches to estimate TC MPI (*e.g.*, Miller 1958, and Holland 1997) which unlike Emanuel's approach, depend on ambient CAPE, Camp and Montgomery (2001) found that Emanuel's MPI approach provided a better estimate of maximum intensity. The shortcomings of Emanuel's model may be due to the ignored asymmetric dynamics of TCs. We note that the MPI as formulated by Emanuel does not account for the necessary work done in the development of the expansive outflow anticyclone as it is assumed that the anticyclone is fully developed and at steady state in this theory (Rappin et al. 2011). In part, because this outflow work is done at the expense of the energy gained in the inflow from surface fluxes of sensible and latent heat, the MPI truly represents an upper bound on intensity. In fact, on average, only 55% of MPI is achieved by

TCs. Furthermore, only about 20% of hurricanes achieve 80% or more of their expected MPI (DeMaria and Kaplan 1994). Furthermore, Persing et al. (2013) found that the intensification rate in the 3-D model is smaller than in the axisymmetric model, because of the lack of convection organization into annular rings, so the axisymmetric model is overly efficient.

Advances in the understanding of intensity change require knowledge of not only those mechanisms that define MPI, but also those that limit intensity (Persing et al. 2003) or could potentially disrupt (or "frustrate", Reimer et al., 2010) the Carnot cycle upon which the MPI theory is based. Camp and Montgomery (2001) suggest that the reason that most TCs fail to reach their MPI is due to the secondary eyewalls and convectively generated vorticity anomalies. Emanuel et al. (2004) showed that wind shear is the main uncertainty for intensity prediction. The ventilation of the TC core by dry environmental air at mid-levels was perhaps the earliest idea on how TC intensity could be constrained by vertical shear (Riehl and Malkus, 1961). Mixing of low θ_e air into the eyewall at mid-levels is thought to be particularly effective because the minimum of θ_e is usually located at this level. Riemer et al. (2010) suggest that this frustration of eyewall θ_e constitutes a "dilution of the fuel burnt in the TC engine" and thus reduces the amount of work produced in the thermodynamic cycle available for kinetic energy increase and concomitant pressure falls. Riemer et al. (2010) proposed a new hypothesis for intensity modification of a TC interacting with vertical shear. They suggest that the energy cycle is frustrated at the inflow layer. Strong and persistent downdrafts in the TC rainband region transport the low θ_e air (characteristic of the low-to-mid-troposphere of the tropical atmosphere), into the boundary layer (inflow region) of the storm, significantly depressing near-core BL θ_e values. Latent and sensible heat fluxes from the warm ocean surface do not recover θ_e values completely, as compared to the undiluted inflow. As a consequence, air parcels in the eyewall start rising with reduced θ_e values. They demonstrated that the dilution process is capable of leading to intensity changes of tens of ms^{-1} (and hPa), without the vortex being sheared apart.

An alternate view of the impact of shear involves the disruption of the TC potential vorticity structure (PV) by the shear. DeMaria (1996) suggest that as the vertical wind shear tilts the PV, the positive temperature perturbations associated with tilted PV could stabilize the mid-troposphere by increases in temperature near the center of the TC. The mid-troposphere

warming could inhibit convection and development of the TC, thus reducing intensity of the TC. More recent work (Jones 2000) has demonstrated that the temperature anomalies associated with vortex tilt also *decrease* stability locally and thus may *enhance* convection.

Cram et al. (2007) calculated Lagrangian air parcel trajectories and studied the transport and mixing processes within a mature and vertically sheared hurricane. They found transport and mixing from the low-level eye to the eyewall. This process could strengthen the hurricane since the air from the eye has high equivalent potential temperature (θ_e). Moreover, there is low-level inflow bypassing the eyewall and entering the eye and acquiring high entropy from sea. In the mid- to upper-level, the eye exchanges air with the eyewall. In addition, there is entrainment from the mid- to upper-level environment with lower θ_e into mid-level eyewall.

Outside the radius of maximum winds, the TC primary circulation is spun up by radial advection of momentum by in flowing air; in the eyewall, the primary circulation is spun up by the mean vertical advection of momentum from the boundary layer, and by radial and vertical eddy momentum fluxes (Montgomery and Smith 2017).

Emanuel (1986) proposed the wind-induced surface heat exchange (WISHE) mechanism, which is self-induced heat transfer from the ocean for intensification and maintenance of TCs. This model resembles a Carnot engine, which is also mentioned by Ooyama (1982). The energy sources are the sensible and latent heat transfer from the ocean; the energy sinks are the surface friction and upper-level cold air. This theory represents a positive feedback between the surface wind speed and the surface heat fluxes in a neutral (to symmetrically unstable) environment. Stronger inflow could induce stronger sea surface sensible and latent heat (*i.e.* moist enthalpy) fluxes, then the heat enhances cumulus convection and the secondary circulation. Heating of condensed water in the precipitation clouds which falls out as rain keeps the neutrality of the atmosphere. The heat transfer from the sea surface would be redistributed by the cumulus convection to keep the environment conditionally neutral and strengthen the secondary circulation. Specifically, condensed water in the mid-troposphere re-evaporates then cools the mid-level atmosphere, then downdrafts import low-entropy air into the boundary layer at a rate that exceeds the enthalpy flux from the ocean surface. When the entropy of the mid-tropospheric air is large enough, the low-entropy flux into the boundary layer by downdrafts is weakened, and the hurricane intensifies (Emanuel

1991). The WISHE mechanism could maintain TCs in steady state without the CISK (Convective Instability of the Second Kind) mechanism of Charney and Elliasen (1964) and stored convective energy (CAPE). Rotunno and Emanuel (1987) verified Emanuel's theories (Emanuel 1986) using a numerical model. Moreover, they showed that WISHE is crucial for TC development and structure. Their modelling results suggested that the horizontal size of a TC is determined by initial disturbance size.

A vortex is inertially stable if the absolute angular momentum increases outward. For an axisymmetric vortex with cyclonic absolute vorticity, larger cyclonic relative vorticity means a more inertially stable vortex. Inertial stability substantially influences the formation and size of eye of a TC, as well as latent heating. Schubert and Hack (1982) found that in a high inertial stability region, the vortex has a stronger stiffening effect, and a weaker secondary circulation and adiabatic cooling, thus net latent heating in the cumulus convection is larger. Since the inertial stability is the largest just inside the radius of maximum wind (RMW), heating in the vicinity of the RMW would accelerate the tangential wind the most inside the RMW, then decrease the RMW. They also found that the formation of an eye could stabilize the TC. Later, Hack and Schubert (1986) verified their theory through numerical modeling. Vigh and Schubert (2009) showed that rapid intensification happens when some eyewall convection appears inside the radius of maximum wind. Formation of an eye could remove diabatic heating from the high-inertial-stability region, then the TC tends to steady state as the core becomes more mature.

b. Adjoint sensitivities and their applications to tropical cyclone studies

Many of the questions surrounding the competing mechanisms of TC intensity change can be framed in the context of sensitivity of the intensity to the variables or processes. Adjoint sensitivity analysis allows for the efficient quantification of how intensity changes are related to changes in the initial conditions or forecast trajectory. In this thesis, we diagnose, describe, and interpret the adjoint sensitivity of the intensity of a simulated TC to the forecast trajectory of the simulation with a focus on the sensitivity to the initial conditions. We briefly review a background on adjoint sensitivities and the results of their applications to TC relevant

problems. A more comprehensive description of adjoint models and related tools is found in Chapter 2.

1) ADJOINT SENSITIVITIES

Use of an adjoint model to solve variational problems was proposed by Le Dimet and Talagrand (1986). They presented the adjoint algorithm to implement the four-dimensional variational data assimilation (4DVAR) which is to minimize a cost function defined as the difference between an observation and the model state representation of the observation. The adjoint of a numerical weather prediction (NWP) model is a tool used to evaluate the sensitivity of some variables to changes in the model state and boundary conditions at earlier times (Errico 1997). The adjoint of an NWP model is defined as the transpose of the tangent linear model (TLM) which is the linearized version of NWP model. The (adjoint-derived) sensitivity is defined as the gradient of the response function (hereinafter R) with respect to the model state. R can be any differentiable function of the model final state; for the purposes of this study, the response functions will be defined to describe the TC intensity. The adjoint model integrates the sensitivity at the final time backwards to calculate the sensitivity at the initial time. The sensitivity at the initial time quantifies the (potential) impacts of the initial condition perturbations on R. The impacts can be estimated as the inner product of the initial condition perturbations and the sensitivity at initial time. In fact, a constraint of adjoint dynamics requires the inner product of the sensitivity and perturbations of variables is invariant while integrating equations backwards. As a consequence, the adjoint-based data assimilation methods like 4DVAR, unlike other data assimilation methods, links the changes of variables to the dynamical equations and relates the initial and final state by atmospheric intrinsic dynamics. More generally, adjoint models enable the identification of the dynamical causes and relationships between different variables.

The concept of sensitivity is very useful to study the influence of the synoptic features which are responsible for evolution of synoptic systems. Studies using adjoint models in this fashion have investigated the most important dynamical processes for the evolution of midlatitude and their associated forecast errors (e.g., Langland et al. 1995, Vukićević and Raeder 1995, Langland and Errico 1996, Langland et al. 2002, Kleist and Morgan 2005b, and Doyle et al. 2014) and tropical cyclone dynamics including steering and intensity change (e.g.,

Wu et al. 2007, Hoover and Morgan 2011, Ito et al. 2011, Chu et al. 2011, Doyle et al. 2012, and Hoover 2015). Many of these studies will be discussed in greater depth in the next section.

The tangent linear model is demonstrated to be valid within 24h (Talagrand and Courtier 1987). Errico and Raeder (1999) tested the linearity of the tangent linear model with moist physics. The linearity holds well in TLM and AM, although sensitivities are larger in moist models, and sensitivities to moist variables are larger than other variables. Linearity holds well where dry dynamics are primary, but poor where moist physics (*e.g.* convection) are dominant. Therefore, it is legitimate to treat the synoptic processes as quasi-linear, and use the tangent linear and adjoint models to study sensitivities.

The sensitivity data output directly from an adjoint model does not include sensitivity to variables that may be of practical dynamical utility in synoptic analysis. Langland (1995) inferred sensitivity to QGPV from sensitivity to the zonal and meridional wind, and temperature. Arbogast (1998) proposed a variational minimization technique to compute sensitivity to potential vorticity (PV) and unbalanced flow within a two-dimensional, steady baroclinic environment. Kleist and Morgan (2005a) derived expressions of sensitivity to vorticity and divergence from sensitivities to the horizontal wind. In this thesis, the suggestions of Arbogast and Kleist and Morgan to calculate the sensitivity to derived variables from the sensitivity to model variables is used.

Evolution of perturbations could be examined in the NLM numerical simulations by perturbing the initial conditions. The resulting perturbed output can be analyzed and differences in the forecast trajectories diagnosed. Optimal perturbations are a way to calculate the smallest changes of variables at the initial time with respect to specific change of response function. As described in Chapter 2, the smallest change here means the smallest change as measured by some form of the perturbation energy (*e.g.* kinetic energy) in some subset of the model domain.

2) ADJOINT APPLICATIONS TO TROPICAL CYCLONE DYNAMICS

Adjoint models have been used in a limited fashion to study TC dynamics. These models have been applied to address the three central issues in TC predictability: those of track (*e.g.*, DeMaria and Jones 1993, Wu et al. 2007, Hoover and Morgan 2010 and 2011), intensity change (*e.g.*, Chu et al 2011, Komaromi et al. 2011, Doyle et al. 2012), and genesis (Hoover

2015). One of the earliest studies using an adjoint model was the study of DeMaria and Jones (1993) who used a barotropic adjoint model to improve the hurricane track forecasts.

Chu et al. (2011) studied sensitivities of the intensity of Typhoon Sinlaku (2008) to horizontal wind, water vapor mixing ratio, and temperature. They found that the most sensitive region during rapid intensification is the storm core and its vicinity through the depth of the troposphere. In addition, sensitivity to moisture is the most significant, which was verified by an idealized targeted observation experiment.

The adjoint-derived sensitivity steering vector (ADSSV; Wu et al. 2007), diagnoses the sensitivity of TC steering flow to the non-divergent wind. The components of the ADSSV are defined as sensitivities with respect to vorticity of the volume averaged zonal and meridional components of the 850-300 hPa deep-layer flow over a volume centered at the TC position. The ADSSV is expressed as: $(\partial R_1 / \partial \zeta, \partial R_2 / \partial \zeta)$, where R_1 and R_2 are the TC centered area averaged zonal wind and meridional wind components over the 850-300-hPa deep-layer respectively, and ζ is the relative vorticity. ADSSV was shown to be useful for the study of binary TC interactions. Wu et al. (2009) found that ADSSV signals were in good agreement with quantitative evaluation based on the PV diagnosis. Further, ADSSV signals could capture features of the TC-trough interaction.

The ADSSV was modified by Hoover and Morgan (2010, 2011). Hoover and Morgan (2010) found that the response functions define by Wu et al. (2007) could not produce sensitivities to steering flow if the perturbations to the initial conditions changed the locations of the TCs at the final time. They overcame this problem by proposing an alternate response function for steering flow, which was defined as the deep-layer average of environmental wind diagnosed as the average flow in a response function box attributed to vorticity distributions outside the response function box. The response functions defined in this way were insensitive to the location of the perturbed TC location *so long as the TC remained in the targeted box*. Aside from the results for the specific cases considered in the manuscript, the significance of Hoover and Morgan (2011) is that it points to the necessity of properly defining response functions to capture the intended forecast aspect of interest.

Hoover (2015) studied East Pacific tropical cyclogenesis using cases from 2004 to 2010 and identified the cases which could grow barotropically in the environment of the low-level

East Pacific jet. Sensitivities of vortex intensity to vorticity were shown to have structures which tilt barotropically upshear, relative to the low-level westerly jet – a signature of barotropic growth. Most cases exhibit barotropic growth structures typified by strong low-level jets with large meridional shear, especially at jet level.

Ito et al. (2011) used a *f*-plane, cloud-permitting, nonhydrostatic, axisymmetric adjoint model to study effects of surface friction and surface sensible and latent heat fluxes on TC intensity. The importance of this contribution is that it represents the first fine-scale adjoint-based sensitivity analysis to understanding of hurricane inner core dynamics and thermodynamics and their relationship to the variability at the sea surface. They defined a hurricane intensity response function as the tangential velocity at the top of boundary layer in the eyewall. They found that an increase of inflow would increase the tangential velocity, which is due to the centrifugal force. They observed a dipole structure of sensitivities to vertical velocity, potential temperature and mixing ratio. These structures can be explained respectively by the continuity equation, buoyancy force and condensation terms of the adjoint model: perturbation of the radial wind is compensated by radial differential vertical motions; increases of potential temperature (increased buoyancy) increases vertical velocity; and increases of water vapor increase potential temperature via condensation, then increase vertical velocity. The sensitivities are positive (negative) in interior (exterior) of the verification region, and related to the surface and exterior of the hurricane. Moreover, sensitivities to momentum fluxes (sensible and latent heat fluxes) are negative (positive) within a certain radius, and could be positive (negative) beyond the radius. Sensitivities to sensible and latent heat fluxes have almost the same magnitude. Sensitivities to heat fluxes and SST are found to be large beneath the eyewall region.

Doyle et al. (2012) conducted a study of the sensitivity and predictability of tropical cyclogenesis using an adjoint model and adjoint-derived optimal perturbations. In their study of Typhoon Nuri, for a response function defined as the kinetic energy per unit mass in a box centered at the cyclone location, adjoint diagnostics indicated that the intensity of Nuri was most sensitive to perturbations in the moisture and temperature fields and to a lesser degree the wind fields. More specifically, they found that increases in the primary circulation, as well as increases of potential temperature and water vapor in the rainband regions of the TC could

intensify the hurricane. In addition, sensitivities to water vapor and vorticity both slope inward toward the cyclone center with maxima in the lower- to mid-troposphere. Optimal perturbations of vorticity and water vapor grew from a sloped structure to a vertical orientation. Moreover, the total energy of the optimal perturbations is largest in the lower-level at the initial time, and grows rapidly throughout the troposphere with maximum in the upper-level, which is consistent with the "bottom-up" mechanism of tropical cyclogenesis (*e.g.*, Ritchie and Holland 1997, Montgomery and Enagonio 1998). Furthermore, from the power spectrum of optimal perturbations of wind, they found that the peak of energy shifts upscale from convective scale to the scale of the vortex, which is consistent with the upscale vortex cascade mechanism. In the following work, we expand upon the work of Doyle et al. (2012) and use an adjoint model and adjoint-informed optimal perturbations to study the dynamics of TC intensification rather than the sensitivity of cyclogenesis.

Brown and Hakim (2015) used ensemble sensitivity analysis (Torn and Hakim, 2008) to evaluate TC intensity sensitivities defined as the normalized correlation between cost function and input variables. They selected a set of rapidly intensifying hurricanes from an ensemble Kalman filter data assimilation system. Through a compositing of the cases studied, they found that an increase of primary circulation at the radius of maximum wind in the lower-troposphere and decrease of tangential wind in the eye could intensify the hurricanes since inertial stability and thermal efficiency were enhanced. Enhancement of secondary circulation would intensify the hurricanes, especially in the boundary layer and near the upper-level outflow. Vertical wind shear was verified to be detrimental for TC intensification. Moreover, increase of humidity in the spiral rainband regions and the core from boundary layer to mid-troposphere could strengthen the hurricanes. An increase of potential temperature in the core especially at mid-level could intensify the hurricanes, since subsidence is increased in the eye. Using their ensemble sensitivities, Brown and Hakim created initial condition perturbations designed to intensify (weaken) the individual cases they considered. They evaluated the actual changes in their cost (response) function compared with the prescribed changes. They found that the predicted changes and actual changes have better agreement for weakening perturbations than intensifying perturbations. They found that dry perturbations play a larger role in fully perturbed changes than moist perturbations. Furthermore, they found that cases

with only moist variables perturbed have less eyewall convective activity.

c. Objectives and outline

In this thesis, the nonlinear model (WRFV3.8) and adjoint model (WRFPLUS V3.8.1) are used to study forecast sensitivity fields related to hurricane intensity for Hurricane Irma (2017). Our object is to: apply adjoint model and optimal perturbation methods to study TC intensity; identify how wind, temperature, and water vapor mixing ratio changes could influence the intensity of Hurricane Irma; and describe the evolution of perturbations optimally designed to influence TC intensity change. To enhance the interpretation of the results, a variational method was developed to diagnose sensitivities to vorticity and divergence from the sensitivities to the zonal and meridional wind components on the native WRF model grids using a quasi-Newton method as a minimizer.

The outline of this thesis is as follows: Chapter 2 introduces the concepts of an adjoint model, optimal perturbations, and application of the quasi-Newton method to solve a Poisson-type equation; Chapter 3 presents a synoptic overview of Hurricane Irma (2017) focusing on three 24h periods during Irma's lifecycle; Section 4 describes the numerical models, simulation methodology, and data used in this research. Section 5 describes and interprets adjoint sensitivities to horizontal winds, potential temperature, mixing ratio, vorticity, and divergence. Chapter 6 discusses results of optimal perturbation experiments – the evolution of optimal perturbations, and compares results of optimal perturbation with respect to kinetic, dry, and total energy norm. Chapter 7 presents discussion and summarizes the conclusions.

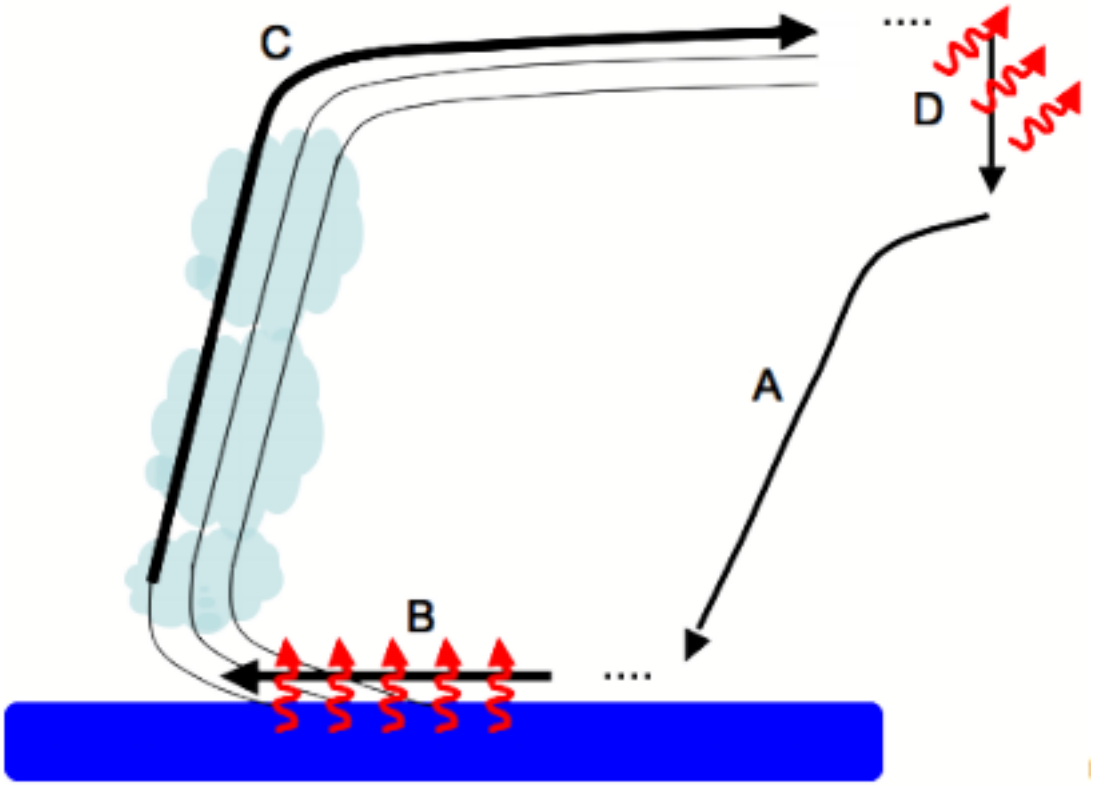

Figure 1.1. The hurricane Carnot cycle in radius-height coordinates of an axisymmetric. The storm center is to the left and the dark blue region indicates the ocean. Thick black arrows denote the hypothesised path of air parcels and contours depict isentropes of θ_e. Red arrows denote sensible and latent heat flux from sea surface to the air. Air spirals toward the storm center in branch B, acquires entropy from the ocean surface. It then ascends adiabatically and flows out near the storm top to some large radius in branch C. The excess entropy is lost by long-wave radiation in branch C. (Adapted from Riemer et al. 2010)

2. Methods

In this chapter, we formally define the notion of an adjoint operator and introduce the concept of an adjoint model as it relates to corresponding nonlinear and tangent linear models. We also define what is meant by a *sensitivity gradient* and how the sensitivity to the initial conditions of a forecast model is calculated using an adjoint model. The chapter concludes with a derivation of adjoint-informed optimal initial perturbations and the development of a variational technique to calculate sensitivities of vorticity, divergence, shearing and stretching deformation from sensitivities to the horizontal wind field. Section 2a, 2b, and 2c are adapted from class notes of Prof. Michael C. Morgan.

a. Adjoint operator defined

The adjoint of a linear operator, **L**, is the linear operator **L*** if **L*** satisfies the relation:

$$\left\langle \mathbf{x}, \mathbf{L}\mathbf{y} \right\rangle_{\mathrm{m}} = \left\langle \mathbf{L}^{*}\mathbf{x}, \mathbf{y} \right\rangle_{\mathrm{n}}$$

where **x** and **y** are vectors in $\mathbb{R}^m$ and $\mathbb{R}^n$ respectively, and $\left\langle \ , \ \right\rangle_{\mathrm{m}} = \left\langle \ , \ \right\rangle_{\mathrm{n}}$ denote inner products in $\mathbb{R}^m$ and $\mathbb{R}^n$ respectively. This definition of an adjoint operator, coupled with the recognition that the *adjoint* of a linear operator is the *transpose of the matrix representation of that operator*, provides a powerful, practical means of analytically and numerically generating adjoints for continuous and discrete operators.

b. Nonlinear model, tangent linear model and adjoint model

A nonlinear NWP model is expressed as a system of equations:

$$\frac{d\mathbf{x}}{dt} = F(\mathbf{x}) \text{ with } \mathbf{x}(t_0) = \mathbf{x}_0$$

where $F(\mathbf{x})$ represents the dynamical and thermodynamical processes within the forecast model as well as diagnostic relationships between model variables (*i.e.*, ideal gas law). Integrating the model from an initial time (t_0) to a final time (t_f) results in a solution:

$$\mathbf{x}(t_f) = \mathbf{x}_f = M(\mathbf{x}_0),$$

where M is a nonlinear operator (the "model"), which maps an input state ($\mathbf{x}_0$) at time t_0 forward to the forecast state ($\mathbf{x}_f$) valid at final time t_f.

A response function, R, is any differentiable function of the model final state defined at that final time. An adjoint-based forecast sensitivity study involves calculating the gradient of the response function with respect to the model state at the final time, $\frac{\partial R}{\partial \mathbf{x}_0}$. Before considering the notion of an adjoint model, we consider what happens to R when we introduce an initial condition perturbation, $\mathbf{x}_0'$, to a control initial condition, $\bar{\mathbf{x}}_0 : \bar{\mathbf{x}}_0 \rightarrow \bar{\mathbf{x}}_0 + \mathbf{x}_0'$. We anticipate that a change to the initial state will lead to a change in the final state, $\bar{\mathbf{x}}_f \rightarrow \bar{\mathbf{x}}_f + \mathbf{x}'_f$; and consequently, a change in the response function, ΔR:

$$\Delta R = R(\bar{\mathbf{x}}_f - \mathbf{x}'_f) - R(\bar{\mathbf{x}}_f) = R(\bar{\mathbf{x}}_f) + < \frac{\partial R}{\partial \mathbf{x}_f}, \mathbf{x}'_f > - R(\bar{\mathbf{x}}_f) + \text{H.O.T.}$$

We define a *linear* estimate of ΔR as δR:

$$\Delta R \cong < \frac{\partial R}{\partial \mathbf{x}_f}, \mathbf{x}'_f > \quad = \delta R$$

There should be some link between our final perturbation $\mathbf{x}'_f$ and the initial condition perturbation, $\mathbf{x}'_0$. We formulate an equation describing the evolution of perturbations by linearizing the nonlinear equation about a basic state defined by the forecast trajectory, $\bar{\mathbf{x}}_t$, $t_0 \leq t \leq t_f$.

$$\frac{d\bar{\mathbf{x}}}{dt} + \frac{d\mathbf{x}'}{dt} = F(\bar{\mathbf{x}} + \mathbf{x}') = F(\bar{\mathbf{x}}) + \left.\frac{\partial F}{\partial \mathbf{x}}\right|_{\bar{\mathbf{x}}} \mathbf{x}' + H.O.T., \text{ that is}$$

$$\frac{d\mathbf{x}'}{dt} = \left.\frac{\partial F}{\partial \mathbf{x}}\right|_{\bar{\mathbf{x}}} \mathbf{x}' \text{ with } \mathbf{x}'(t_0) = \mathbf{x}'_0$$

The solution to this system may be written:

$$\mathbf{x}'(t_f) = \mathbf{L}\mathbf{x}'(t_0) = \mathbf{L}\mathbf{x}'_0$$

where $\mathbf{L}$, a function of the basic state, is the resolvant matrix or the *tangent linear model* (TLM) which integrates initial *perturbations* forward in time. With this result, we may estimate the change in R attributed to a perturbations of the initial state (and again make use of the definition of the adjoint):

$$\delta R = <\frac{\partial R}{\partial \mathbf{x}_f}, \mathbf{x}'_f> = <\frac{\partial R}{\partial \mathbf{x}_f}, \mathbf{L}\mathbf{x}'_0> = <\mathbf{L}^* \frac{\partial R}{\partial \mathbf{x}_f}, \mathbf{x}'_0> \quad \text{or}$$

$$\delta R = <\mathbf{L}^* \frac{\partial R}{\partial \mathbf{x}_f}, \mathbf{x}'_0> = <\frac{\partial R}{\partial \mathbf{x}_0}, \mathbf{x}'_0>.$$

We again arrive at the result:

$$\frac{\partial R}{\partial \mathbf{x}_0} = \mathbf{L}^* \frac{\partial R}{\partial \mathbf{x}_f}.$$

The sensitivity gradient we seek is determined by integrating the adjoint model from the final time (t_f) *to the initial time* (t_0) *with the sensitivity of the response function with respect to the model final state the initial condition* (*i.e., the input*) *of the adjoint model.*

Consider a real differentiable function of an NWP model forecast state, $R(\mathbf{x}_f)$, called the *response function*. A perturbation to the initial model state $\delta \mathbf{x}_0$, will result in a change of the response function at final time is defined by inner product of sensitivity evaluated at the final time and a change (perturbation) to the output state, $\delta \mathbf{x}_f$:

$$\Delta R = R(\mathbf{x}_f + \delta \mathbf{x}_f) - R(\mathbf{x}_f) \cong \left\langle \frac{\partial R}{\partial \mathbf{x}_f}, \delta \mathbf{x}_f \right\rangle$$

Sensitivity, in the context of this thesis, is defined as the gradient of a response function with respect to the model state, $\partial R / \partial \mathbf{x}_0$.

c. Optimal perturbation

To test, ultimately, the interpretation of the forecast sensitivities as well as the assumptions of linearity, adjoint-informed initial condition perturbations are created to add to our control initial conditions to evaluate their impact on the response function and to diagnose their evolution. These perturbations are "optimal" in the sense that they represent the smallest perturbation to the model input (as measured by a quadratic norm) that can produce a prescribed change to a linear or linearized response function, ΔR. The formulation of Errico (1997) and Hoover and Morgan (2010) is used in calculating the optimal perturbation. Here the quadratic norm used to measure the initial condition perturbation is the energy norm (reference) defined as:

$$T = \frac{1}{2}\left\langle \delta \mathbf{x}_0, \mathbf{W}\delta \mathbf{x}_0 \right\rangle = \frac{1}{2}\int_0^1 \iint_{\Re} \left(u'^2 + v'^2 + \frac{c_p}{T_{ref}} T'^2 + \frac{L}{c_p T_{ref}} q_v'^2 + \frac{RT_{ref}}{p_0'^2} p'^2 \right) d\Re d\eta$$

In this definition of the norm, $\delta \mathbf{x}_0$ is the vector representing the perturbations of the modeled atmospheric components of the state vector; its components $\delta \mathbf{x}_0 = \left(\mathbf{u}', \mathbf{v}', \mathbf{T}', \mathbf{q}_v', \mathbf{p}'\right)$ are the horizontal components of the wind, the temperature, the water vapor mixing ratio, and the perturbation pressure. The weights given to those components are given by a reference temperature and pressure, T_{ref} and p_{ref}; as well as the dry air gas constant, R; the specific heat of air at constant pressure, c_p; and the specific heat of vaporization, L. The integration is taken over the depth of the atmosphere and over the model domain, R. The discrete form of this expression may be expressed by the matrix **W**. The total energy of the initial condition perturbation, $\delta\mathbf{x}_0$, is calculated as:

$$T = \frac{1}{2}\left\langle \delta \mathbf{x}_0, \mathbf{W}\delta \mathbf{x}_0 \right\rangle,$$

where the energy norm matrix is a diagonal matrix whose elements depend on the type of energy being calculated. For an initial condition perturbation with only perturbations to the horizontal flow field, **W**, would provide a measure of the kinetic energy per unit mass, and be a matrix with just 1 along the diagonal. For a perturbation including also the temperature as well, *i.e.*, the dry air energy (kinetic energy plus the internal energy per unit mass), **W**, and moist air energy (KE+IE+latent energy). Explicitly, to calculate kinetic energy, we use the diagonal weighting matrix, **W**, with entries of 1 along the diagonal. To calculate dry air energy, we use the diagonal weighting matrix, **W**, with entries of 1 along the diagonal for those entries that weight the wind components, and $\frac{c_p}{\overline{T}}$ for those that weight the temperature (where c_p is the specific heat capacity of dry air at constant pressure, and $\overline{T}$ denotes a fixed reference state absolute temperature. In the calculation, we calculate the perturbations to initial state that minimize change of energy. This energy could be kinetic energy, kinetic energy plus internal energy, or kinetic energy combined with internal energy and latent energy.

To find the minimum of T, subject to the constraint that the initial condition perturbation, $\delta\mathbf{x}_0$, results in a change in the response function, $\Delta R = \left\langle \frac{\partial R}{\partial \mathbf{x}_0}, \delta\mathbf{x}_0 \right\rangle$, we use the method of Lagrange multipliers. We define the Lagrangian, L:

$$L = T + \lambda\left(\Delta R - \left\langle \frac{\partial R}{\partial \mathbf{x}_0}, \delta\mathbf{x}_0 \right\rangle \right)$$

where $\lambda \in \mathrm{R}$ is the Lagrange multiplier. The minimum of L, is found at the location where:

$$\frac{\partial L}{\partial \delta\mathbf{x}_0} = \mathbf{W}\delta\mathbf{x}_0 - \lambda\frac{\partial R}{\partial \mathbf{x}_0} = 0 \text{ or } \delta\mathbf{x}_0 = \lambda\mathbf{W}^{-1}\frac{\partial R}{\partial \mathbf{x}_0} \text{ and}$$

$$\frac{\partial L}{\partial \lambda} = \Delta R - \left\langle \frac{\partial R}{\partial \mathbf{x}_0}, \delta\mathbf{x}_0 \right\rangle = 0 \text{ or } \Delta R = \left\langle \frac{\partial R}{\partial \mathbf{x}_0}, \delta\mathbf{x}_0 \right\rangle.$$

Substituting in $\delta\mathbf{x}_0$, $\Delta R = \left\langle \frac{\partial R}{\partial \mathbf{x}_0}, \lambda\mathbf{W}^{-1}\frac{\partial R}{\partial \mathbf{x}_0} \right\rangle = \lambda\left\langle \frac{\partial R}{\partial \mathbf{x}_0}, \mathbf{W}^{-1}\frac{\partial R}{\partial \mathbf{x}_0} \right\rangle$, yields: $\lambda = \frac{\Delta R}{\left\langle \frac{\partial R}{\partial \mathbf{x}_0}, \mathbf{W}^{-1}\frac{\partial R}{\partial \mathbf{x}_0} \right\rangle}$.

The initial condition perturbation is thus:

$$\delta\mathbf{x}_0 = \Delta R \frac{\mathbf{W}^{-1}\frac{\partial R}{\partial \mathbf{x}_0}}{\left\langle \frac{\partial R}{\partial \mathbf{x}_0}, \mathbf{W}^{-1}\frac{\partial R}{\partial \mathbf{x}_0} \right\rangle}.$$

d. Sensitivities to derived variables

For any response function, the sensitivities of those response functions to the model state **x** (which includes the zonal wind (*u)*, meridional wind (*v)*, vertical motion (*w)*, temperature (*T)*, dynamical pressure perturbation (*p')*, and dry air mass in the column (μ), and specific humidity (q_v)) are direct outputs of the WRF adjoint. While these sensitivities are easily interpretable, for the purposes of synoptic case studies it is desirable to evaluate the sensitivities with respect to Galilean invariant kinematic features of flow such as vorticity and divergence (ζ and δ respectively; Kleist and Morgan 2005a). In this way, the sensitivities can be directly related to synoptic features (*e.g.*, vorticity extrema associated with upper-

tropospheric "short waves"). These sensitivities are directly calculable from the sensitivities to the horizontal wind components:

$$\nabla^2\hat{\zeta} = -\left(\frac{\partial \hat{v}}{\partial x} - \frac{\partial \hat{u}}{\partial y}\right) \text{ and } \nabla^2\hat{\delta} = -\left(\frac{\partial \hat{u}}{\partial x} + \frac{\partial \hat{v}}{\partial y}\right),$$

where the "hat"-symbol is a shorthand representation of the sensitivity of R with respect to the hatted variable (*e.g.* $\hat{\mathbf{a}} = \frac{\partial R}{\partial \mathbf{a}}$). Kleist and Morgan (2005a) promoted the use of "sensitivity vectors" which allow for the vector depiction of sensitivities to the horizontal wind to enhance synoptic interpretation of the forecast sensitivity fields. To calculate these sensitivities from the adjoint model output, we notice that they require the solution of a Poisson-type equation, $\nabla^2 g = h(x,y)$, which has a unique solution (g) for a given distribution of (h) and prescribed boundary conditions. We note that for this problem the boundary conditions that are applied typically are homogeneous, Dirichlet conditions, *i.e.*, $g = g^b = 0$ along the boundary.

Rather than employ the widely-used technique of successive over-relaxation (SOR) to solve this Poisson-type equation, we adopt a faster, and efficient variational approach, wherein we minimize an objective or cost function, J:

$$J = \frac{1}{2}\left\langle \left(\nabla^2 g - h\right), \left(\nabla^2 g - h\right) \right\rangle,$$

to obtain the solution, $g(x,y)$. The minimization algorithm chosen is a variant of the quasi-Newton method that requires a gradient with respect to the function, g, easily derivable as:

$$\nabla_g J = \nabla^2\left(\nabla^2 g - h\right).$$

The function, g, that satisfies, $\nabla_g J = 0$, yields the desired minimum of J, and hence our solution.

We solve for the sensitivities on the native WRF model Arakwawa C-grid – chosen to be a Lambert conformal grid. As this is a discretized problem, the map factors at each grid point within the domain must be considered when derivatives and Laplacians are evaluated. Horizontal discretization of the model onto a $nx \times ny$ Cartesian grid where $x \rightarrow x_i$, $i = 0$ to nx and $y \rightarrow y_j$, $j = 0$ to ny grid allows the discretized Poisson equation in the grid space of the

model to be written: $m_{i,j}\nabla^2 g_{i,j} = h_{i,j}$ where $m_{i,j}$ are the map factors at the model cross points, ∇^2 is the discretized Laplacian operator:

$$\nabla^2 g \cong \nabla^2 g_{i,j} = \frac{g_{i+1,j} - 2g_{i,j} + g_{i-1,j}}{(\Delta x)^2} + \frac{g_{i,j+1} - 2g_{i,j} + g_{i,j-1}}{(\Delta y)^2}, \text{ or}$$

$$\nabla^2 g_{i,j} = A_1 g_{i,j-1} + A_2 g_{i-1,j} + A_3 g_{i,j} + A_4 g_{i+1,j} + A_5 g_{i,j+1}.$$

The coefficients, A_m, are numbered according to their position relative to the gridpoint (i,j), point number 3 (Fig. 2.1). The zonal (meridional) grid spacing is nominally Δx (Δy).

Next, the boundary conditions are incorporated into the discretized Laplacian operator. Consider the northwestern most point within the domain, (i = 1, j = ny-1). At this point, the discretized equation is written:

$$\nabla^2 g_{1,ny-1} = A_1 g_{i,j-1} + A_2 g^b_{i-1,j} + A_3 g_{i,j} + A_4 g_{i+1,j} + A_5 g_{i,j+1} = \frac{h_{i,j}}{m_{i,j}}.$$

Because g_b is known, as is the righthand-side, h, we can rewrite the discretized equation at that point as:

$$\nabla^2 g_{1,ny-1} = A_1 g_{1,ny-2} + A_3 g_{1,j} + A_4 g_{2,ny-1} + A_5 g_{1,ny} = \frac{h_{1,ny-1}}{m_{i,j}} - A_2 g^b_{0,j} = \tilde{h}_{1,ny-1}.$$

In general, the Poisson equation with boundary conditions incorporated may be written as the linear equation:

$$\mathbf{Lg} = \tilde{\mathbf{h}},$$

where **L** represents a banded matrix operator that calculates the Laplacian at all points in the domain, making use of the prescribed boundary conditions and **g** and **h** are vectors with elements described by the values of g and modified h at all *interior* gridpoints. Then we solve this Poisson-type equation by minimizing the cost function, J:

$$J = \frac{1}{2}\left\langle (\mathbf{Lg} - \tilde{\mathbf{h}}), (\mathbf{Lg} - \tilde{\mathbf{h}}) \right\rangle,$$

through the quasi-Newton method.

As a background to Newton's method, consider the one-dimensional problem, $f(x) = 0$. If the gradient of the function, in this case its first derivative is known, a search for

the zeros of the function, x_i, $i = 1$ to n, $f(x_i) = 0$, proceeds with a first guess and an evaluation of $f(x_{(n)})$ and $f'(x_{(n)})$:

$$x_{(n+1)} = x_{(n)} - \frac{f(x_{(n)})}{f'(x_{(n)})}.$$

Like Newton's method, the quasi-Newton methods represent a set of iterative numerical techniques to search for the stationary point of a multi-dimensional function. These methods are used if the gradient (for zeros) or the Hessian (for extrema) of the function are unavailable or too expensive to compute at every iteration.

The optimization algorithm chosen for this study was the Limited-memory Broyden-Fletcher-Goldfarb-Shanno, a quasi-Newton method that approximates the Broyden–Fletcher–Goldfarb–Shanno (BFGS) algorithm using a limited amount computer memory. The BFGS algorithm uses approximations to the Hessian to search for the minimum, while, L-BGFS stores only a few vectors that represent the approximation implicitly. This reduced storage of the approximation to the Hessian makes this algorithm well-suited for a problem of large dimension – such as the problem at hand. The particular implementation used in this work was coded in Python and available from the SciPy.org library as: *scipy.optimize.fmin_l_bfgs_b* (Zhu et. al, 1997). Because of the size the problem being solved, **L** is a band matrix (i.e. a sparse matrix whose non-zero entries are in a diagonal band). With the help of a sparse matrix storing method (*scipy.sparse.bsr_matrix*), we can reduce its storage and speed-up the calculation by storing only the non-zero elements.

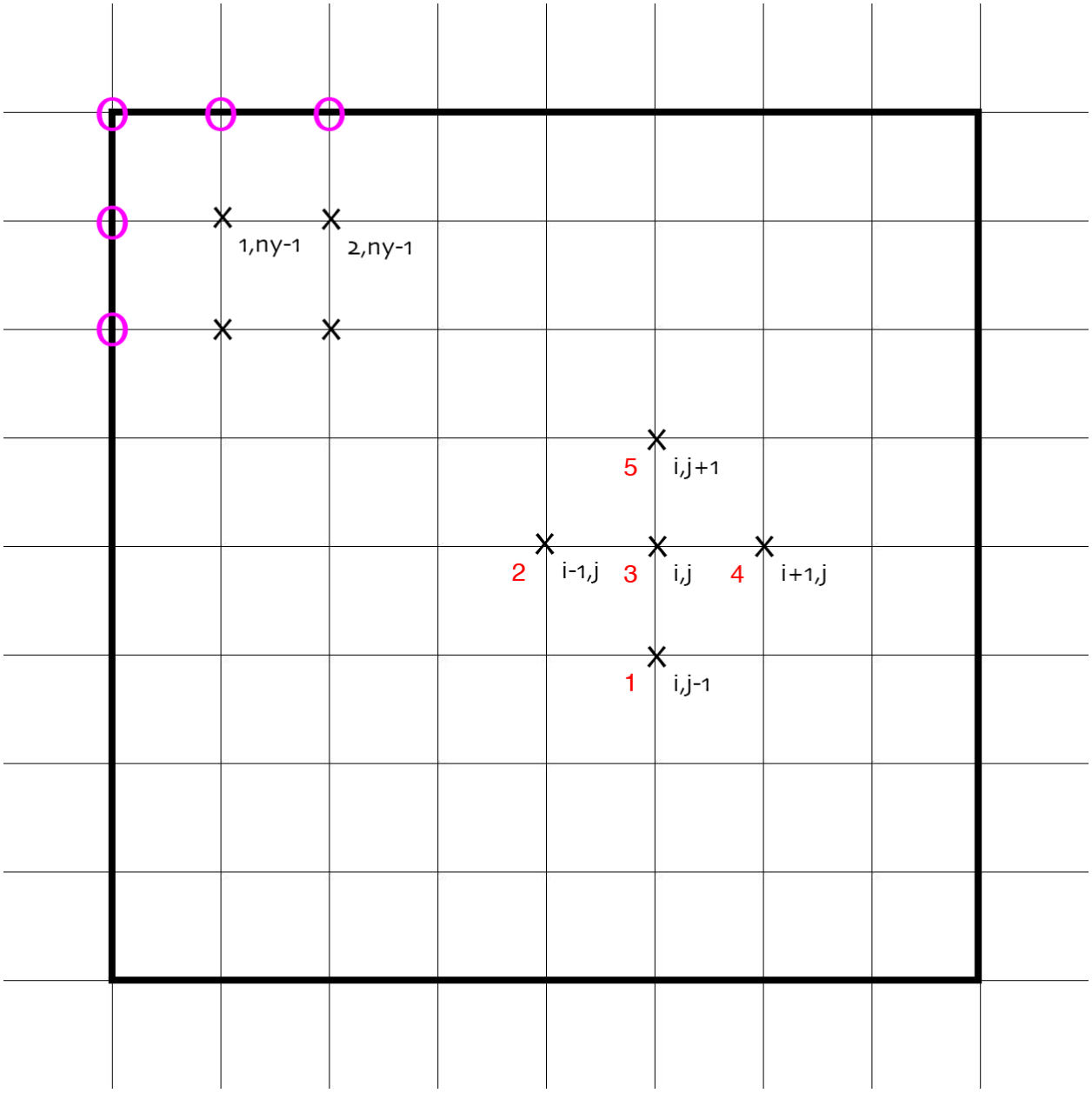

Figure 2.1. Schematic of discretization used in the variational solution to a Poisson-type equation.

3. Synoptic Overview

a. Overview

Hurricane Irma (2017) developed from a tropical wave that departed the west coast of Africa on 27 August. Irma was a long-lived Cape Verde hurricane that reached category 5 intensity on the Saffir-Simpson Hurricane Wind Scale prior to landfall in the northeastern Caribbean island of Barbuda around 0545 UTC 6 September with maximum winds of 155 kt and a minimum pressure of 914 hPa. Irma made landfall as a category 4 hurricane in the Florida Keys and struck southwestern Florida at category 3 intensity. Irma caused widespread devastation across the affected areas and was one of the strongest and costliest hurricanes on record in the Atlantic basin. Irma caused 44 direct deaths, especially in the Caribbean Islands (Cangialosi et al. 2018). In this section, we describe briefly the synoptic environment within which Irma evolved for three 24h synoptic periods beginning at 0000 UTC 05, 09, and 10 September. These will be referred to as Period 1, Period 2, and Period 3 (or P1, P2, P3) henceforth. Period 1 05-06 September was the time period in which Irma intensified into a category 5 hurricane. From 09-10 September 2017 is the time while Irma interacted with islands of the southern Bahamas and northern Cuba. Irma made landfall in south Florida and weakened while moving northward during the period 10-11 September. Below we referenced the National Hurricane Center analysis (Cangialosi et al. 2018) and discuss the synoptic history of Hurricane Irma.

Irma became a tropical depression at 0000 UTC 30 August when it was located west-southwest of Sao Vicente in the Cabo Verde Islands, reaching tropical storm status 6 h later, and hurricane status at 0600 UTC 31 August. Irma was positioned south of the Azores anticyclone, and progressed westward over the eastern Atlantic prior to 31 August. Irma intensified rapidly in favorable environment of low vertical wind shear and moist, lower troposphere while it was over marginally warm waters. Later on 31 August, Irma started rapidly intensification while turning west-northwestward as the ridge to its north weakened slightly. Irma reached category 2 intensity by 1200 UTC 31 August, and reached category 3 intensity by 1800 UTC 31 August.

After reaching category 3, Irma stopped intensifying with the eye occasionally becoming cloud filled and deep convection in the eyewall appearing less intense. Irma's

intensity fluctuated between category 2 and 3 from 0000 1 September to 0000 UTC 4 September. This may be due to eyewall replacement cycles and intrusions of dry air. Meanwhile, Irma turned west-southward as a strong anticyclone to its north built westward over central Atlantic.

On 4 September, Irma strengthened to a category 4 hurricane after completing an eyewall replacement cycle, and moved toward the northern Leeward islands. Irma turned west-northwestward, due to the erosion of the western side of the mid-level ridge, and went through another round of rapid intensification. During 4 September, Irma was in a favorable environment for intensification with high SSTs, abundant mid-tropospheric, and low vertical wind shear. This favorable environment lasted in the succeeding days. On 5 September, Irma reached its maximum lifetime intensity of 155 kt around 1800 UTC 5 September, when it was located east-southeast of Barbuda. Irma made landfall on Barbuda, St. Martin and islands of Virgin Gorda during 6 September. Irma weakened due to its interactions with land, but it remained as a category 5 hurricane. Irma moved to the north of Puerto Rico and the Dominican Republic from 1800 UTC 6 September to 1800 UTC 7 September. Irma passed south of the Turks and Caicos Islands and made landfall on Little Inagua Islands on 8 September. Irma turned slightly the west and moved toward the northern coast of Cuba. This is due to a westward building subtropical ridge. Irma weakened to category 4 and 18 h latter strengthened to category 5 on 8 September. In these days, surface friction weakened Irma, but it remained strong since the environment was still favorable.

Irma intensified a little and made landfall near Cayo Romano, Cuba at 0300 UTC 9 September with maximum wind speed of 145 kt. Irma moved along the Cuban Keys during 9 September. Friction weakened it significantly down to a category 2 hurricane by 1800 UTC. After that time, Irma slowed and began to make a turn to the northwest. On 10 September, Irma moved over warm waters of Florida Straits, and intensified again to a category 4 hurricane by 0600 UTC. Irma turned to the north-northwest in the flow between a subtropical ridge over the western Atlantic and a mid- to upper-troposphere low over the Gulf of Mexico.

Irma weakened to a category 3 hurricane due to increasing southwesterly vertical wind shear around 1800 UTC 10 September, and made its final landfall near Marco Island, Florida at 1930 UTC 10 September with maximum wind speed of 100 kt and minimum pressure of

936 hPa. While moving inland over Florida, Irma weakened quickly due to surface friction and strong vertical wind shear. Irma weakened to category 2 by 0000 UTC 11 September, and to category 1 by 0600 UTC 11 September. Irma weakened to a tropical storm by 1200 UTC 11 September. Irma became a remnant low by 0600 UTC 12 September, and moved northwestward over southeastern Missouri.

Below a more detailed description of the synoptic environment of Irma is discussed for each of the three periods.

b. Period 1 (0000 UTC 5 September – 0000 UTC 6 September 2017)

On 0000 UTC 5 September, Hurricane Irma was located at 16.6°N, 55.1°W and tracking westward. The estimated maximum winds were 125 kt (up from 110 kts 12 hours earlier) and the minimum pressure was now 943 hPa (down just 2 hPa in 12 hours). The cyclone was steered by a subtropical ridge to its north over the central Atlantic. The environment was favorable for Irma's furthering strengthening. The environmental vertical wind shear was relatively low (Fig. 3.1b). The near-cyclone environment was relatively moist as evidenced by the high layer-averaged relative humidity in the mid-troposphere (Fig. 3.1c); however, immediately to the west of Irma was a region of dry air (lower than 60% relative humidity). At this time, Irma traversed increasing SSTs (not shown). In Fig. 3.1d, the outflow from Irma in the 100-to-200 hPa layer, characterized by generally low Ertel PV and a strongly divergent flow on the western side of Irma, was expansive, covering much of the central Atlantic basin. Center and west of the cyclone, the PV of the environment was a local maximum.

In the 5AM AST National Hurricane Center forecast discussion, the forecaster (Avila) noted that, "The hurricane will be moving through an environment of low vertical wind shear, a moist mid-level atmosphere, and increasing upper-ocean heat content, and this is ideal for some additional intensification." The cyclone continued westward, arriving at 16.7N, 57.8W by 1200 UTC 5 September. The minimum pressure had fallen 14 hPa over past 12 h while the maximum wind speed had increased to 150 kt. Except for the thermal shear typical of a warm core vortex, the environmental shear remained weak (Fig. 3.2b). The downstream TC environment was still relatively dry (Fig. 3.2c), while the core of Irma remained moist. The PV in the outflow layer had decreased in the near and far environment of the storm – an

indication of the TC intensification, as well as an indication of more favorable conditions for further strengthening (Fig. 3.2d). The local maximum of PV seen at 0000 UTC had been advected southeastward and was now located over the Windward Islands.

Irma turned west-northwestward and went through another round of rapid intensification. The hurricane reached its maximum intensity of 155 kt around 1800 UTC 5 September, when it was located about 70 n mi east-southeast of Barbuda. Located at 17.3N 60.6W, the TC had gained over half a degree of latitude over the last 12 hours. The hurricane continued to be in a low shear with an expansive low PV environment (Fig. 3.3b). The relative humidity of the downstream environment decreased as the cyclone moved west-northwestward (Fig. 3.3c). As the TC intensified, its PV tower extended into the 100-to-200 hPa layer and the associated cyclonic flow at 150 hPa was also evident (Fig. 3.3d).

c. Period 2 (0000 UTC 9 September – 0000 UTC 10 September 2017)

By 0000 UTC 9 September, Hurricane Irma was located at 22° N, 77.2° W and steered to move west-northwestward along the northern coast of Cuba. The best-track wind estimate of intensity indicated the wind was now 145 kt (up from 135 kts 12 hours earlier) and the central pressure was now 924 hPa – down just 3 hPa in 12 hours. Weakening of Irma is due to the interaction with islands. The NHC Tropical Cyclone Report (Cangialosi et al. 2018) notes that reconnaissance and microwave data indicated that the inner core of Irma had begun recovering following an eyewall replacement cycle during its passage just north of Puerto Rico and the island of Hispaniola. The cyclone was located on the southwestern side of the subtropical ridge which was weakened by a mid- to upper-tropospheric trough over the southeast of United States. The large environmental vertical wind shear surrounding Irma was not favorable for intensification (Fig. 3.4b). The mid-troposphere relative humidity near the hurricane was large around the hurricane (Fig. 3.4c). Moreover, the environment northwest of Irma over Florida was also moist (higher than 70% relative humidity). The outflow from Irma in the 100-to-200 hPa layer was characterized by generally low Ertel PV and anticyclonically divergent flow around the hurricane (Fig. 3.4d).

By 1200 UTC 9 September, Hurricane Irma continued moving west-northwestward along the northern coast of Cuba, arriving at 22.7°N, 79.3°W. The central pressure increased

17 hPa to 941 hPa over this 12-h period with the maximum sustained wind speed decreased to 110 kt. This intensity change resulted in Irma weakening from a category 5 hurricane to a category 3 hurricane. The environmental vertical wind shear was strong south and east of Irma, but small downstream of Irma (Fig. 3.5b). The environment near and downstream of Irma was still moist (Fig. 3.5c). The PV in the outflow layer has increase in the cyclone center and over the downstream (Fig. 3.5d).

After 1800 UTC, Irma moved slowly northwestward and stayed along the north coast of Cuba for about 6 hours. Irma left the northern coast of Cuba and arrived at 23.4°N, 80.9°W by 0000 UTC 10 September. Irma weakened further during the intervening 12h. During that time the maximum wind speed of Irma decreased from 10 kt to 100 kt, and the central pressure of Irma decreased 9 hPa to 932 hPa. The vertical wind shear was large in the center and downstream (over Florida and Gulf of Mexico) of Irma (Fig. 3.6b). The relative humidity of the downstream environment and in the hurricane was high while the cyclone moved toward the Florida Peninsula (Fig. 3.6c). The PV in the 100-to-200 hPa layer was still large in the cyclone center and the environment (Fig. 3.6d).

d. Period 3 (0000 UTC 10 September – 0000 UTC 11 September 2017)

By 1200 UTC 10 September, Hurricane Irma was located at 24.5°N, 81.5°W and moved northward toward the Florida Peninsula. The maximum wind speed was now 115 kt (up from 100 kts 12 hours earlier) and the minimum pressure had decreased by 1 hPa to 931 hPa over the past 12h. The TC was steered with increasing speed by a low-to-mid-level ridge over western Atlantic Ocean and mid-to-upper-level low over Gulf of Mexico coast. The environmental vertical wind shear was relatively strong in the vicinity of the hurricane especially downstream of the hurricane (Fig. 3.7b). The environment of the hurricane and the downstream has characterized by high relative humidity (Fig. 3.7c). In the 100-to-200 hPa layer, there is high Ertel PV around the hurricane (Fig. 3.7d).

Irma continued moving northward and made landfall on the western coast of Florida. By 0000 UTC 11 September, Hurricane Irma had substantially weakened with maximum wind speed of 80 kts and a central pressure of 942 hPa. Located at 26.8°N 81.7°W, the TC had gained 2.3 degree of latitude over the last 12 hours. The vertical wind shear was large and

relative humidity was high in the vicinity of and downstream of the hurricane (Fig. 3.8b). PV was maximized in the hurricane and northwest of the hurricane (Fig. 3.8c). At 150 hPa, there is a cyclonic flow around hurricane Irma, and outflow north of Irma (Fig. 3.8d).

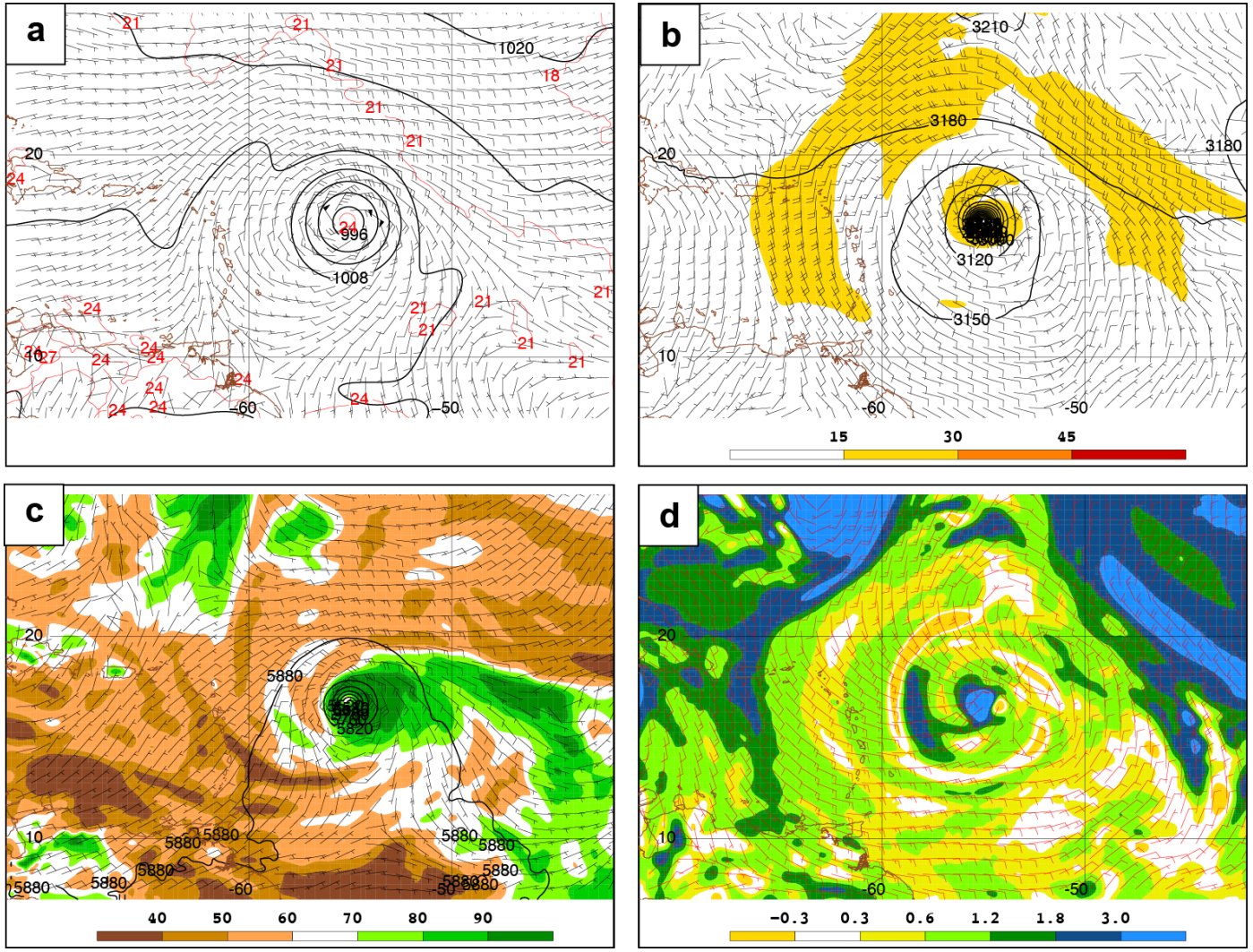

Figure 3.1. Synoptic charts for 0000 UTC 5 September 2017: (a) Mean sea level pressure (black contour, interval 4 hPa), temperature (red contour, interval 3C), and 925 hPa wind (barbs, ms-1); (b) 200-to-500 hPa wind shear (fill, interval, 15 ms-1), barbs, ms-1, and 700 hPa geopotential height (contour, interval 30m); (c) 400-to-900 hPa relative humidity (fill, interval 10%), 500 hPa geopotential height (contour, interval 60m), and 500 hPa wind (barbs, ms-1); and (d) 100-to-200 hPa potential vorticity (fill, PVU) and 150 hPa wind (barbs, ms-1).

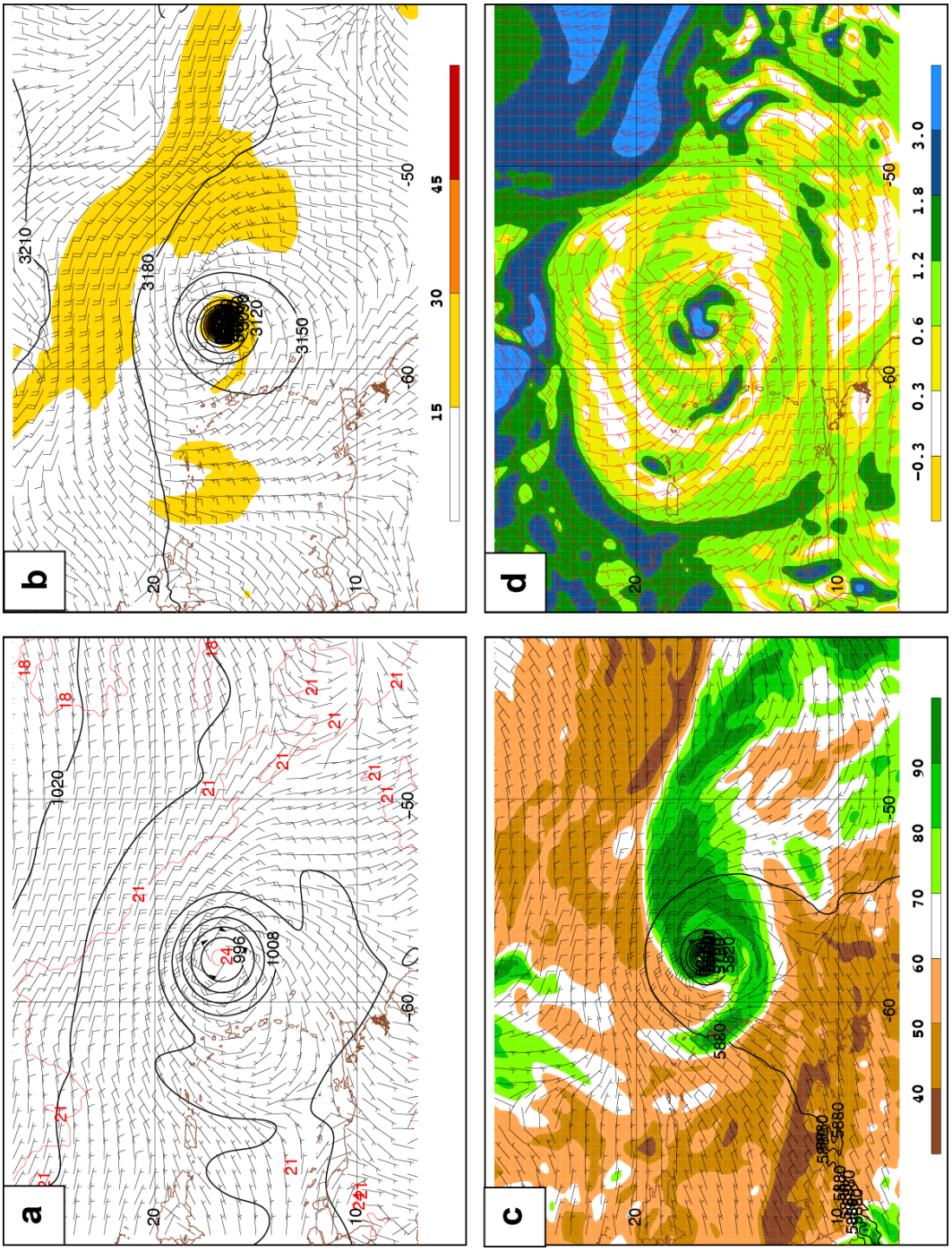

Figure 3.2. As in 3.1, but for 1200 UTC 5 September 2017.

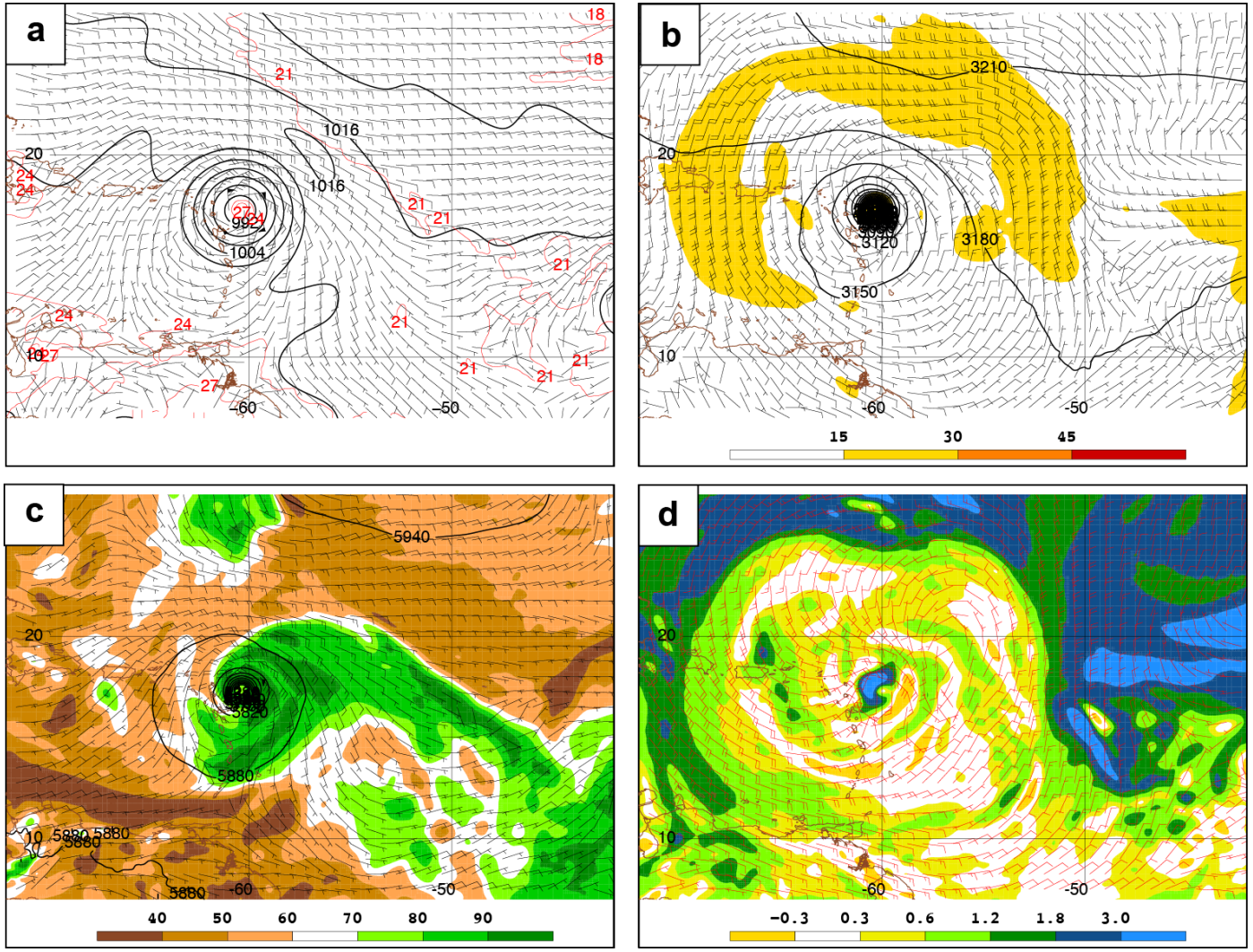

Figure 3.3. As in 3.1, but for 0000 UTC 6 September 2017.

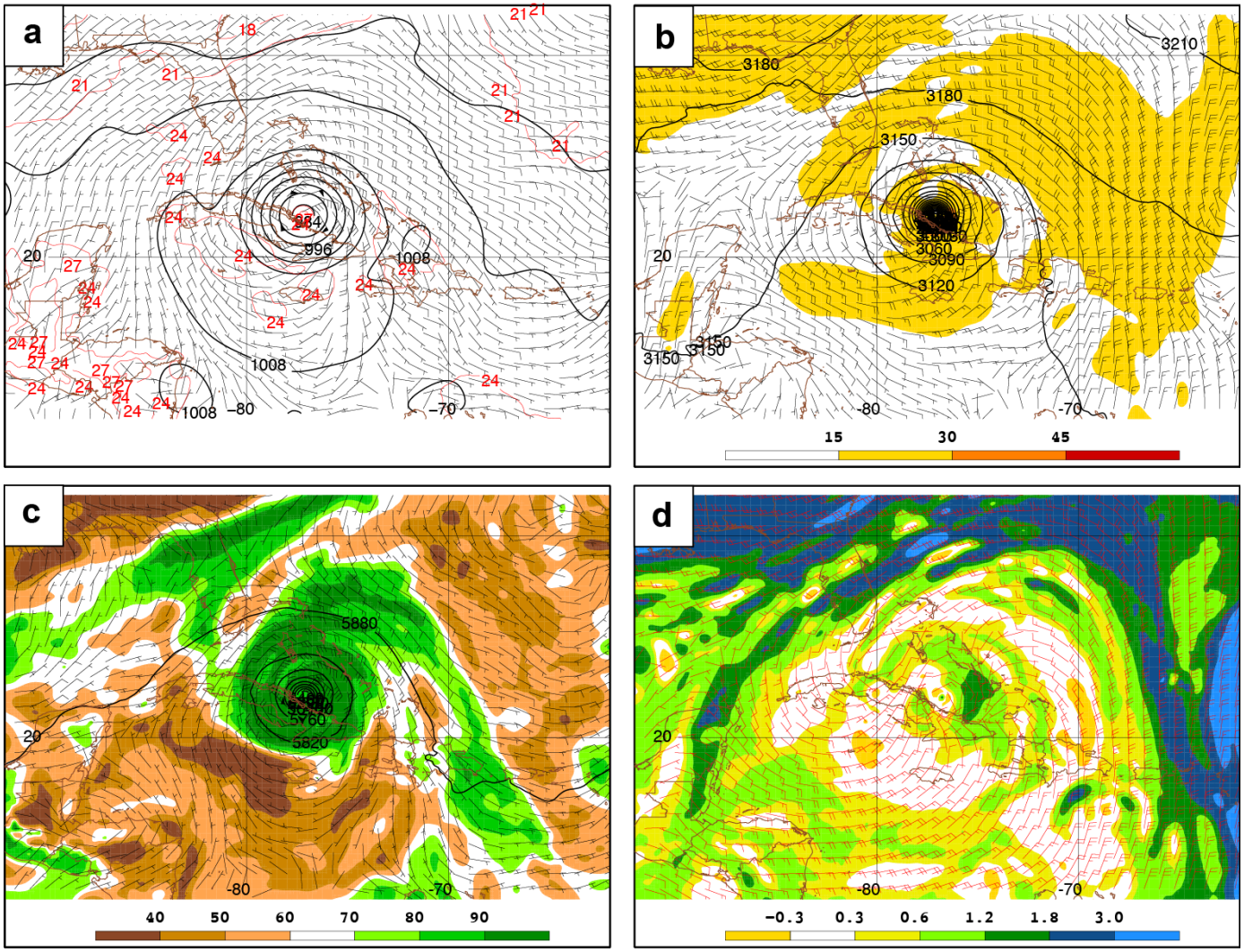

Figure 3.4. As in 3.1, but for 0000 UTC 9 September 2017.

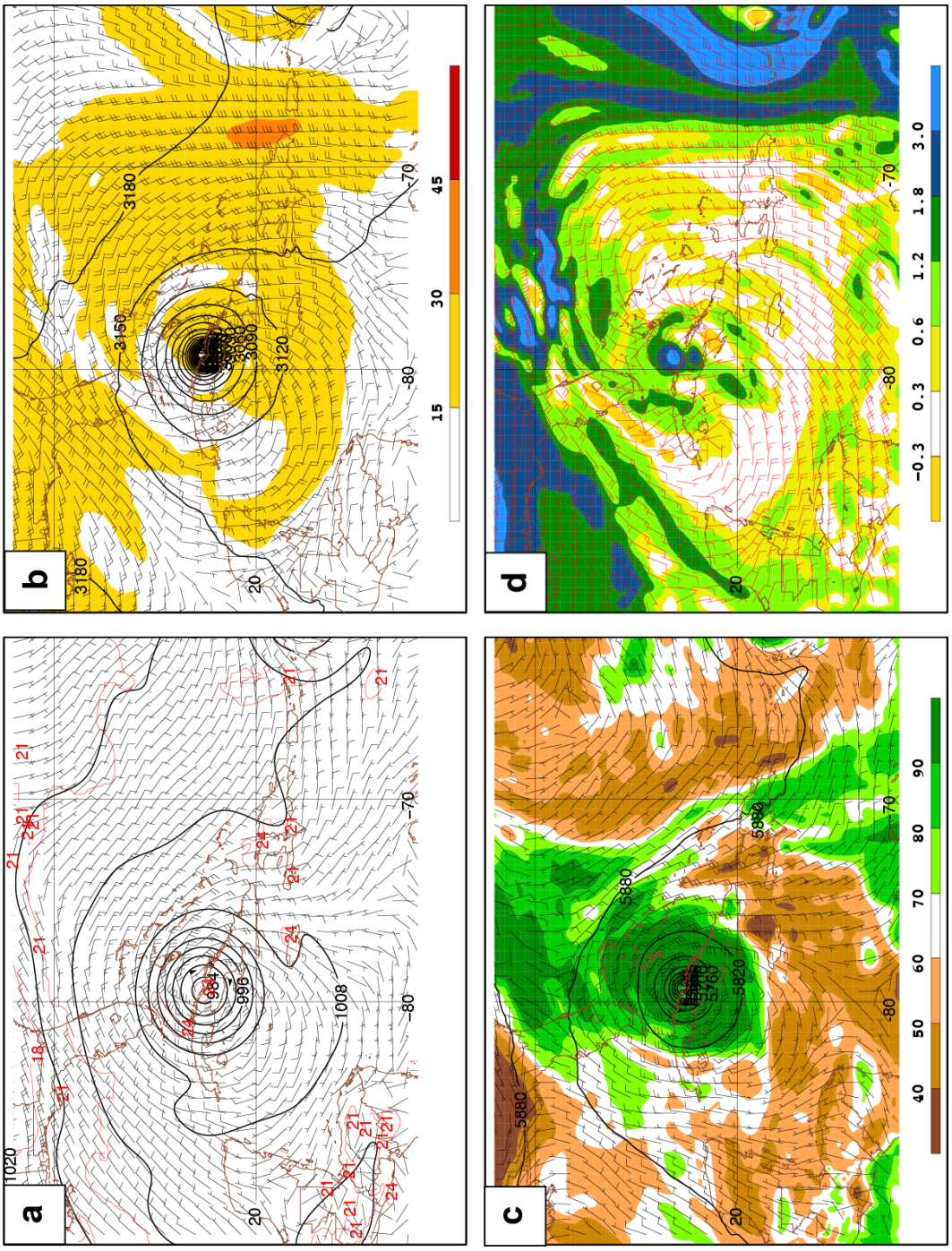

Figure 3.5. As in 3.1, but for 1200 UTC 9 September 2017.

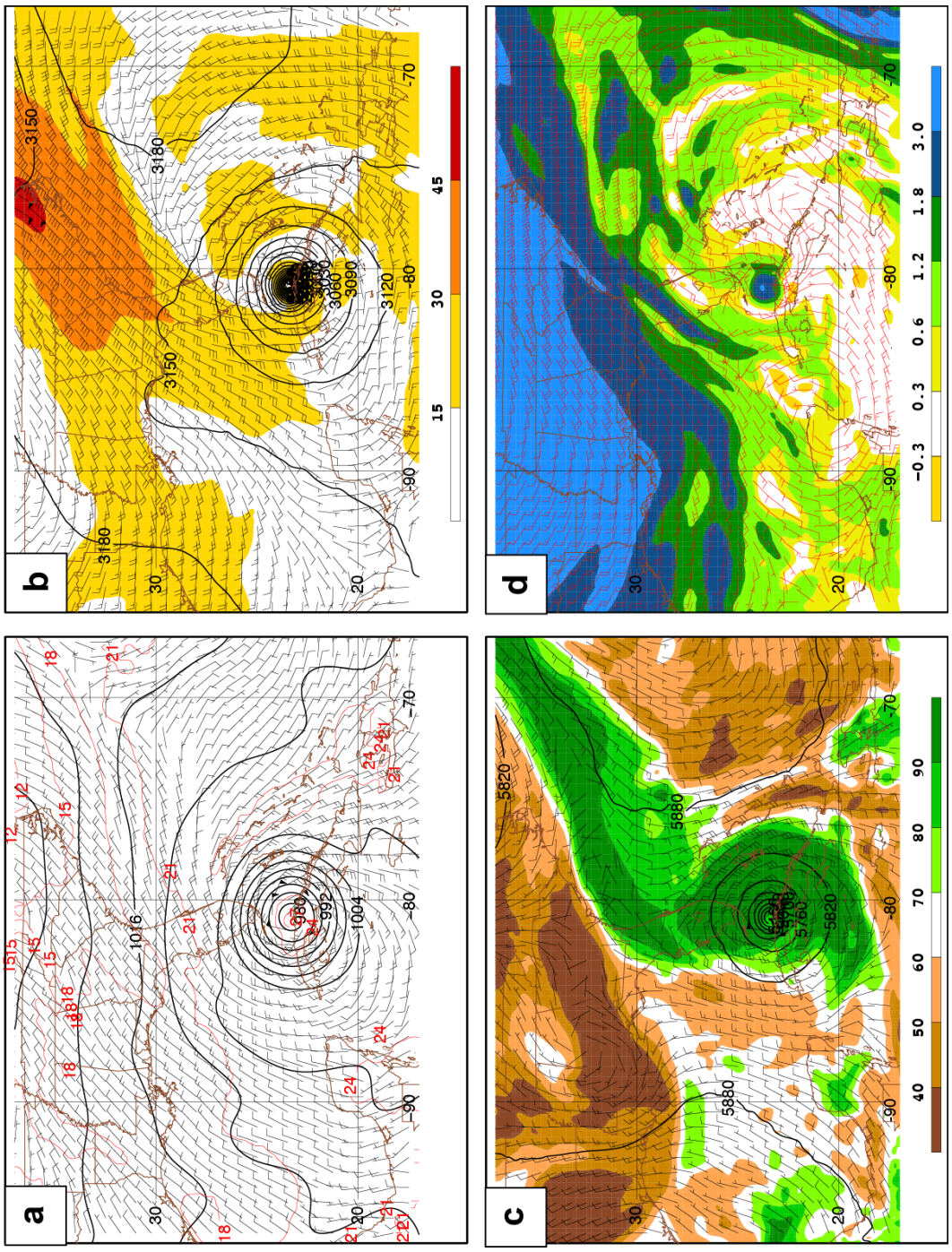

Figure 3.6. As in 3.1, but for 0000 UTC 10 September 2017.

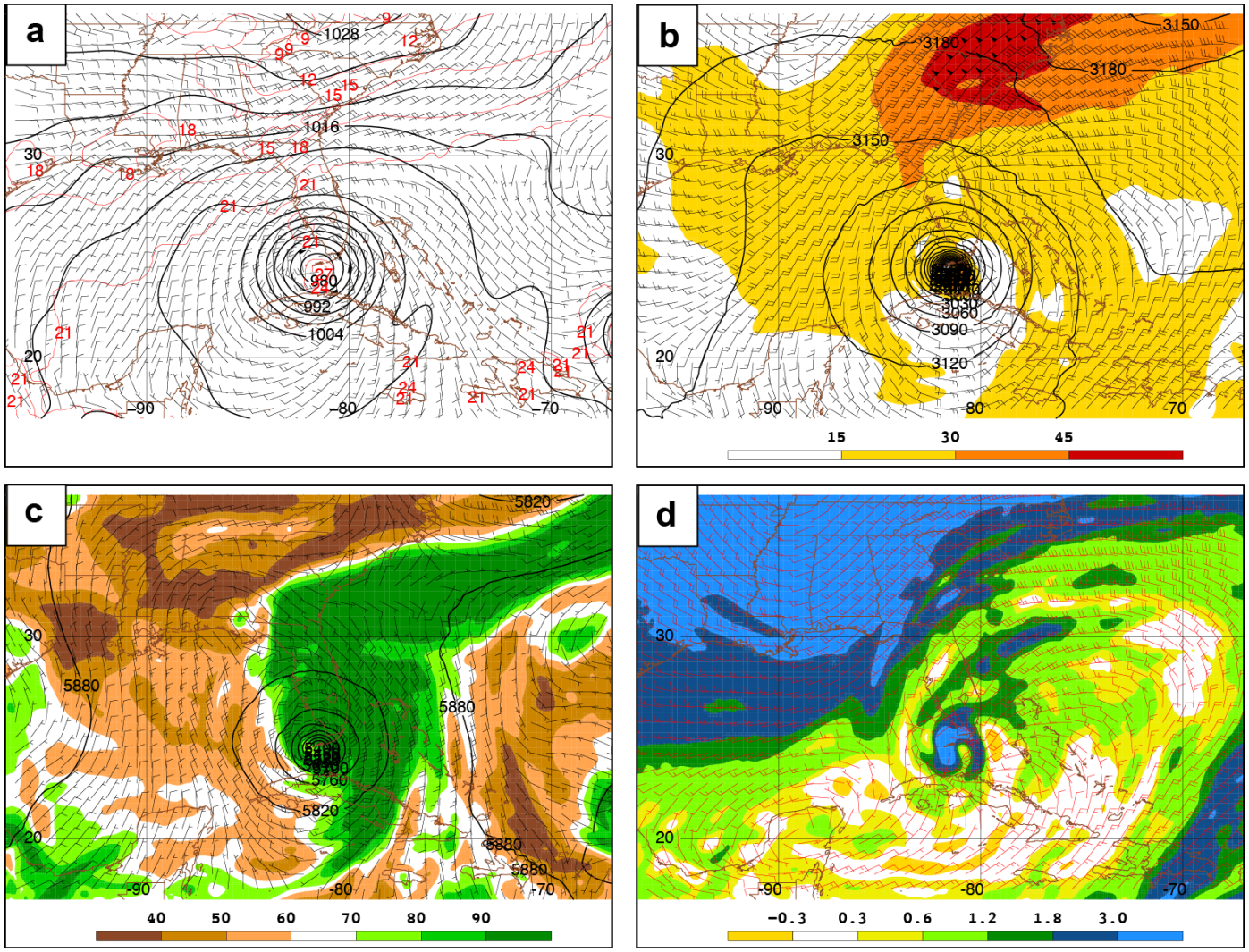

Figure 3.7. As in 3.1, but for 1200 UTC 10 September 2017.

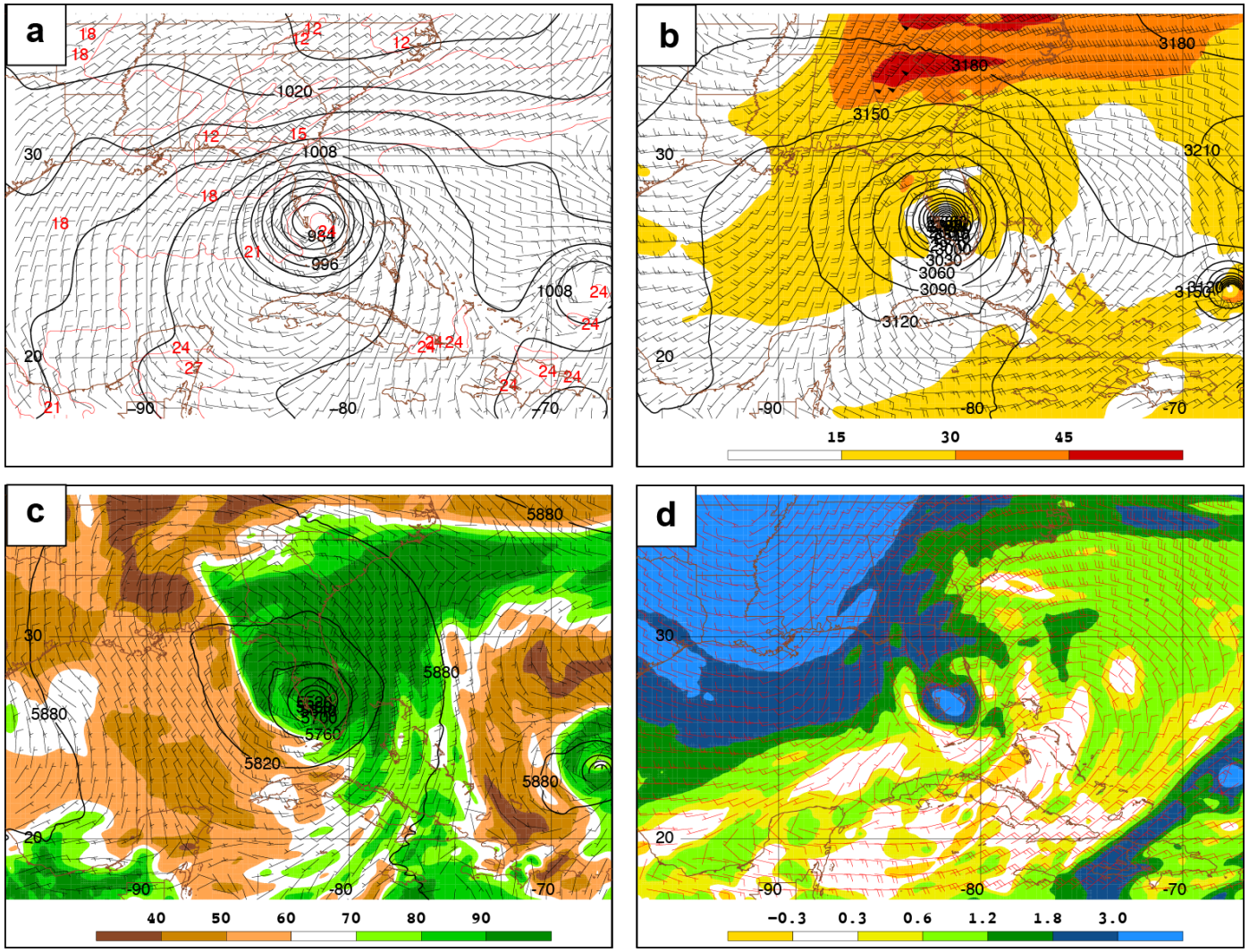

Figure 3.8. As in 3.1, but for 0000 UTC 11 September 2017.

4. Model and Data

a. Nonlinear Model

In this research, the Weather Research and Forecasting (WRF; Skamarock et al. 2008) version 3.8.1) model is used for nonlinear simulation of Hurricane Irma. The WRF model is a fully compressible, nonhydrostatic model with a terrain-following hydrostatic pressure coordinate. The grid staggering is the Arakawa C-grid. The model uses 2nd and 3rd order time integration schemes, and 2nd to 6th order advection schemes in both the horizontal and vertical. The WRF V3.8.1 model is used to conduct three 24h simulations of Hurricane Irma (2017) starting at 0000 UTC 5, 9, and 10 September 2017 using a 30 km, 210 x 144 horizontal grid on a Lambert conformal map projection, with 30 terrain-following vertical levels. The model output is saved every 3 hours. Physical parameterizations used in the simulation are given in Table 4.1. Diffusion and Damping Options are shown in Table 4.2.

Table 4.1 Physics Options

Physics Options	Name
Cloud microphysics	Goddard microphysics scheme
Longwave radiation	RRTM (Rapid Radiative Transfer Model) scheme
Shortwave radiation	Goddard shortwave scheme
Surface layer	MM5 similarity
Land surface	Noah Land surface model
Planetary boundary layer	Yonsei University scheme
Subgrid cumulus parameterization	Kain-Fritsch scheme

Table 4.2 Diffusion and Damping Options

Diffusion and Damping Options	Name
Diffusion Option	Full diffusion
K Option	2D Deformation

b. Tangent Linear Model and Adjoint Model

For this study, the adjoint of the WRF model available through WRFPLUS (Zhang et al. 2013) V3.8.1 is used to calculate the adjoint sensitivity at initial time. The WRFPLUS contains both the tangent linear and adjoint models based on a simplified WRF model, which includes a few simplified physics processes, such as surface drag, large-scale condensation and precipitation, and cumulus parameterization. Because the adjoint of the gravity wave drag for the WRF is not available, it was disabled in the adjoint simulation. The model output is saved every 3 minutes to establish the basic state around which the adjoint model is linearized.

c. Data

Initial and boundary conditions were obtained from the National Center for Environmental Prediction (NCEP) FNL (Final) operational global analyses on 0.25° x 0.25° grids available from the National Center for Atmospheric Research (NCAR) Research Data archive as dataset ds083.3. The data used from this archive include analyses for NCEP's Global Forecast System (GFS) every 6 h (at 0000, 0600, 1200, 1800 UTC daily) and short-term 3 hour forecasts of the GFS from those 6-hourly analyses. In this configuration, our boundary conditions for the simulations are updated every 3 hours.

d. Procedure

Model initial conditions were prepared using the WRF Preprocessing System (WPS) to process the NCEP global final analyses. The WRFPLUS v3.8.1 WRF-ARW forward model was used to create a 24h control forecast trajectory saved every 3 minutes. The WRFPLUS

v3.8.1 adjoint is used to calculate the adjoint sensitivities of an intensity-measuring response function to the model forecast trajectory. The response function, *R*, was chosen as minus the sum of the dry air mass (μ: defined as the pressure difference between the surface and the top of the model) in a 25×25 grid response function box centered on the eye of the simulated TC: $R = \sum_{i,j \in \text{box}} -\mu_{i,j}$, where *i* and *j* represent the zonal and meridional indices of the grid points.

Results of the calculations are described and interpreted in Chapter 5. Finally, in Chapter 6, the optimal initial perturbation method described in Chapter 2 is used to perturb the model initial conditions. The control and perturbed simulations are compared to evaluate and understand the influences of the perturbations on intensifying and weakening the hurricane.

5. Adjoint sensitivity study

a. Overview

A description of adjoint sensitivities to initial conditions during the lifecycle of Hurricane Irma is presented in this section. We focus on adjoint sensitivities to the model variables zonal and meridional wind (u and v respectively), potential temperature (θ), and mixing ratio (r), as well as sensitivities to the derived variables vorticity and divergence. In order to compare the sensitivities at different phases of the hurricane lifecycle, the numerical simulations are performed for three 24h periods beginning at 0000 UTC: 05-06 September 2017 (hereinafter, Period 1 or P1), 09-10 September 2017 (hereinafter, Period 2 or P2), and 10-11 September 2017 (hereinafter, Period 3 or P3).

For a given variable at a given level, we define a *normalized sensitivity* to that variable as the ratio of the horizontally averaged sensitivity to the maximum of the horizontally averaged sensitivities for all model levels. Figure 5.1 shows the vertical profiles of normalized sensitivities to u, v, θ, and r. For all three periods, the sensitivities to the initial distributions of the four variables exhibit a double-peaked structure in the lower troposphere, with peaks at 2 and 4 km. The lower-most peak for P2 (Fig. 5.1b) is weaker than at the other two times. The sensitivities fall off monotonically to about 10% of their peak value at 20 km.

b. Wind sensitivity

1) SENSITIVITY TO VORTICITY

Figure 5.2 shows the horizontal distributions of initial condition sensitivities to vorticity and sensitivities to horizontal winds at the 14th model level ($\eta = 0.4937$) that is close to 500 hPa. For P1 (Fig. 5.2a), the sensitivities to horizontal winds, depicted as "sensitivity vectors" Kleist and Morgan (2005a), are largest nearest Irma with three regions suggestive of confluence to the north, northwest, and southwest of the cyclone. The sensitivities to wind appear to have a positive vertical component to their curl around Irma with the exception of the southeast quadrant of the storm. Consistent with the sensitivities to horizontal winds, the sensitivities to vorticity are positive in the hurricane and the environment around the hurricane. The maxima of sensitivities to vorticity are located in the northern semicircle of the hurricane with minima to the southeast. In addition, sensitivities to vorticity spiral anticyclonically into

the cyclone center against the vortex flow. These sensitivities indicate that perturbations to the winds or vorticity consistent with the orientation and sign of these sensitivities would increase the intensity of Irma 24 hours later. The pattern of vorticity sensitivities is consistent with the distribution of vorticity perturbations in shear flow which would grow the most in finite time (Nolan and Farrell 1999). Nolan and Farrell (1999) cite the work of Orr (1907) who showed that "the growth of a perturbation in linear, inviscid shear flow is determined solely by how far back against the shear the disturbance is originally tilted."

For P2 (Fig. 5.2b) and P3 (Fig. 5.2c), sensitivities to wind and vorticity are similar to that for P1; however, the sensitivities to wind (vorticity) indicate that a stronger cyclonic wind (vorticity) field in the vicinity of Irma would lead to a more intense hurricane at the end of each of the 24h periods. Not only are the sensitivities to vorticity for P2 and P3 are stronger than those for P1, they are also more expansive northwest and east of the hurricane, maximized to north of the hurricane. The sensitivities to wind are maximized in an annulus removed from the core of Irma.

2) SENSITIVITY TO DIVERGENCE

Figure 5.3 shows the horizontal distributions of the sensitivities to initial divergence and sensitivities to initial horizontal wind at the 14th (~500 hPa) level of the model for all three periods. For P1 (Fig. 5.3a), sensitivity to divergence is strongly negative in the center of the domain, and weakly positive on the western and eastern sides of the domain. At the start of P1, Irma lies on eastern edge of the divergence sensitivity minimum. The message conveyed from this distribution is that convergence at model level 14 in the domain center or divergence in the eastern and western most thirds of the domain could intensify the hurricane. The most direct interpretation of this results is that vortex stretching as associated with the pattern of convergence, spins up the TC vortex, as the cyclone heads westward, so that the hurricane strengthens.

For P2 (Fig. 5.3b) and P3 (Fig. 5.3c), sensitivities to divergence are similar to that for P1, though markedly weaker. Furthermore, for P2 and P3, Irma is embedded within the sensitivity minima, not on the edge of it. The structure of the sensitivity to divergence for all three periods does not readily lend itself to interpretation, and further study of this variable is warranted.

3) SENSITIVITY TO TANGENTIAL WIND

(i) Horizontal distribution

Figure 5.4 shows the horizontal distributions of vertically averaged sensitivities to initial distribution of tangential wind. These sensitivities are calculated by evaluating, relative to the cyclone center the component of the sensitivity to the horizontal wind tangential to concentric circles of increasing radii from the cyclone center. During P1 (Fig. 5.4a), sensitivities are located around the cyclone center with a spiral-banded structure. The sensitivity is predominately positive, though to the southeast of Irma, there is a negative sensitivity. Maxima in this field are located northeast of Irma. Sensitivities to this tangential wind are conspicuously absent from the core of the cyclone. An increase of tangential (primary) circulation in band spiraling anticyclonically toward the cyclone center could strengthen the hurricane. This pattern corresponds to sensitivities to vorticity, since increase of tangential wind in this pattern would increase lateral shear along the spiral bands, then increase cyclonic vorticity along the spiral band. It is important to note that the vertical component of the curl of this field does not yield the sensitivity to vorticity (Kleist and Morgan 2005a).

During P2 (Figure 5.4b), sensitivities are positive in a band that spirals anticyclonically into the cyclone center. The positive sensitivities are strongest south of the hurricane. Some weak negative sensitivities are located in the northern semicircle of the hurricane. There are positive sensitivities well to the northwest and northeast of the hurricane. During P3 (Figure 5.4c), sensitivities are positive in an anticyclonically inwardly-spiraling band, and negative immediately to the northeast of the hurricane. The sensitivities south of the hurricane are strongest, and stronger than those diagnosed for either P1 or P2. There are strong positive sensitivities in the space between the trough and the hurricane and in the base of the trough over eastern United States and Sargasso Sea, and weak positive sensitivities northwest of the hurricane over United States.

In general, the three cases have similar sensitivity structures. They indicate that increase of primary circulation in an anticyclonically spiral band could intensify the hurricane. This pattern is consistent with sensitivities to vorticity. Moreover, there are suggestions that the northeast US trough also has some influence on the hurricane intensity during P3.

(ii) Azimuthally averaged, radius-height cross sections

Figure 5.5 shows *azimuthally-averaged,* radial cross-sections of sensitivities to the initial tangential wind. The positive (negative) values indicate a tangential flow into (out of) the plane of the page. For P1 (Fig. 5.5a), initial condition sensitivities to the tangential wind are generally positive in the rainband regions (*i.e.* at 1-7 km in altitude and more than 100 km from the cyclone center), and negative outside of and next to the radius of maximum winds (RMW) and boundary layer of rainband regions (not obvious because negative values are too weak). This means that an increase of primary circulation in the rainband regions could intensify Irma 24 hours hence.

For P2 (Fig. 5.5b), sensitivities are positive in the rainband regions (*i.e.*, at 1-6 km in altitude and more than 250 km from the TC center). Negative sensitivities are located outside of and next to the RMW (at 3-6 km altitude and 100-200 km from the cyclone center). For P3 (Fig. 5.5c), positive sensitivities are located in the rainband regions (*i.e.* at 1-9 km 300-800 km from the center), and 1-4 km 50-250 km from the center. Negative sensitivities are located outside of RMW and between the positive sensitivities (*i.e.* at 4-6 km 200-250 km from the center). Sensitivities for all three periods are similar: positive in the rainband regions and negative outside of and next to the RMW.

To sum up, sensitivities to tangential wind are strong and positive in the rainband regions from lower- to mid-troposphere, weak and negative outside of and next to the RMW. Hence, increase of the primary (azimuthal) circulation in the lower- to mid-tropospheric rainband regions (*i.e.*, outside of the RMW) would strengthen the hurricane. Furthermore, there are weak negative sensitivities in the boundary layer extending from the cyclone center to several hundred kilometers from the center, which means that decrease the tangential wind speed in the boundary layer could strengthen the hurricane.

4) SENSITIVITY TO RADIAL WIND

Figure 5.6 shows radial cross-sections of sensitivities to radial wind with the azimuthally-averaged radial flow (light dashed contours). The negative values mean inflow, and positive values mean outflow. This variable lacks a consistent message, and does not indicate that an increase of the secondary circulation could intensify the hurricane. This is not consistent with the results of Brown and Hakim (2015), which found that an increase in the TC secondary circulation at the initialization time could intensify the Irma 24 hours later. Brown

and Hakim's sensitivities are defined as the correlations between the response function and variables, so their sensitivities are different from our sensitivities which are defined through model dynamics. Their sensitivities could only show the correlations between variables instead of dynamical connections. More intense hurricanes would have stronger secondary circulation, but that does not mean that enhancement of the secondary circulation could strengthen the hurricane. Our results suggest that a stronger secondary circulation is a result of a stronger hurricane, instead of a cause of a stronger hurricane. This interpretation is consistent with the notion that in the context of a TC, a secondary circulation arises to keep the primary circulation in hydrostatic and gradient wind balance in the face of heating and friction. Figure 5.7 shows the sensitivities to radial wind at 850 hPa. The sensitivities are not axisymmetric in the vicinity of Irma. This is consistent with the notion that increase of the secondary circulation at initial time could not intensity the hurricane, since if it could, negative sensitivities to the radial wind ("inflow") around the hurricane center (at this level) would be observed.

c. Sensitivity to potential temperature

1) HORIZONTAL DISTRIBUTION

Figure 5.8 shows the horizontal distributions of all-level vertically averaged sensitivities to the initial distributions of potential temperature (hereafter, θ). For P1 (Fig. 5.8a), sensitivities to θ exhibit a moat-like structure: positive in the cyclone center and in the rainband regions, but weak in a ring-like area around the TC center corresponding to the eyewall region. This pattern is also observed by Doyle et al. (2012). In addition, for this period, the maxima of sensitivities are located in the northeast and southwest of the TC. Therefore, increase of θ in the cyclone center and rainband regions could intensify the hurricane. The reason for the weak sensitivities in the eyewall may be that the eyewall air is already warm, so an increase of θ there would not have much influence on TC intensity.

For P2 (Fig. 5.8b), the structures of the sensitivities in the hurricane are similar to the sensitivities for P1. The strongest sensitivities are located in the cyclone center and south of the hurricane. There are positive sensitivities extending from the base of the east coast trough to the hurricane. For P3 (Fig. 5.8c), sensitivities in the hurricane are similar to P1 and P2's.

The sensitivities in the base of the trough are much stronger than the sensitivities in Irma, they are the maxima in the domain. Largest sensitivities in the vicinity of Irma are its south.

Figure 5.9 shows the 850 hPa distribution of sensitivities to θ. For P1 (Fig. 5.9a), the sensitivities are positive in the cyclone center and banded outer region (*i.e.* rainband regions) of the hurricane with maxima west of the hurricane (*i.e.* where equivalent potential temperature, θ_e, is small, not shown). Therefore, increase of θ in the cyclone center and in its rainband regions could intensify the hurricane, especially on the side closer to small θ_e. During P2 (Fig. 5.9b), sensitivities are positive in the cyclone center and the rainband regions with a maximum southwest of the hurricane (*i.e.* closer to small θ_e). Additionally, there are some weak positive sensitivities from central Virginia southward to the Bahamas. During P3 (Fig. 5.9c), the sensitivities are positive in the cyclone center and in its the rainband regions, and strong south of the hurricane where θ_e is small. The maxima of sensitivities are in the base of the trough over the eastern coast of United States.

In general, sensitivities to θ are large in the cyclone center and the rainband region. These structures indicate that heating in the eye and the rainband could intensify the hurricane. The sensitivities in the base of the mid-latitude trough are strong, which may indicate the interactions between the hurricane and the trough. Sensitivities are strong on the side of the hurricane that is closer to small θ_e, this may be a compensation for weakening effect of small θ_e.

2) RADIAL CROSS-SECTION

Figure 5.10 shows the radial cross-sections of sensitivities to θ with equivalent potential temperature (dashed) For P1 (Fig. 5.10a), sensitivities to θ are positive in the eye and the rainband regions. Maxima of sensitivities to θ are located in the lower- to mid-tropospheric rainband regions (*i.e.* at 1-5 km altitude and 150-650 km from the cyclone center). Sensitivities in the rainband regions slope inward with height in the lower levels. Sensitivities are weak in the eyewall region (*i.e.* at 50-100 km from the cyclone center). The sensitivities to θ appear to be maximized near and around the equivalent potential temperature minimum characteristic of the tropical atmosphere. To conclude, structures of sensitivities show that sensitivities are strong in the cyclone center and in the rainband region. These structures are consistent with

the horizontal distributions of vertically averaged sensitivities to θ. So to intensify the hurricane, we could increase θ in the eye and in the rainband regions.

During P2 (Fig. 5.10b), positive sensitivities are strong in the rainband regions (*i.e.* at 1-6 km 200-700 km from the center). Like the sensitivities in P1, they also slope inward with height in the lower-troposphere, but locate higher and farther from the cyclone center. Moreover, there are strong positive sensitivities in the cyclone center at 1-16 km, which are stronger than the sensitivities in eye in P1. During P3 (Fig. 5.10c), sensitivities are positive at 1-10 km all the way from the center to 800 km from the center, and weaker in the eyewall region (*i.e.* at 50-100 km from the center). Sensitivities are the strongest in the rainband regions (i.e. at 1-5 km 100-500 km from the cyclone center) and in the cyclone center (*i.e.* at 0-50 km from the center). Maxima of sensitivities are located closer to the cyclone center than the maxima of sensitivities in P1 and P2.

Generally speaking, the radial cross-section of sensitivities to θ shows strong positive sensitivities in the rainband regions (*i.e.* more than 100 km from the center) from lower- to mid-troposphere, and in the eye from lower- to upper-troposphere. In addition, in the lower-tropospheric rainband regioins, the sensitivities slope down with radius. To intensify the hurricane, we could heat the eye from lower- to upper-troposphere and the rainband regions from lower- to mid-troposphere.

Increasing the potential temperature in the eye could increase the buoyancy and decrease the downdraft in the eye, thus the pressure in the eye would decrease, and intensity of the hurricane increases (Smith 2006). By mid-level entrainment and low-level transport of eye air into the eyewall, convection in the eyewall would enhance if the eye air is warmer (Persing and Montgomery 2003, Cram et al. 2007). In addition, increase of potential temperature in the rainband regions could increase buoyancy of air parcels, then enhance convection in the rainband, and enhance the inflow above the boundary layer according to Sawyer-Eliassen equation (Fudeyasu and Wang 2011). As a consequence, the enhanced inflow could transport even more sensible heat, latent heat, and angular momemtum toward the core. Furthermore, the inflow would also transport the more buoyant rainband air into the eyewall, enhancing the convection in the eyewall (Emanuel 1991, Riemer et al. 2010). The above two processes could thus strengthen the hurricane.

3) CROSS-SECTION

Figure 5.11 shows sample cross-sections of sensitivities to potential temperature. For P1 (Fig. 5.11a), sensitivities to θ are large in the lower- to mid-tropospheric rainband regions and the cyclone center, but weak near the eyewall. There are some banded structures in the outer region (*i.e.* rainband region). Sensitivities slope inward toward the cyclone center like sensitivities to wind (not shown). This is also observed by Doyle (2012), and possibly due to the fact that the boundary between cyclonic and anticyclonic circulation slopes inward with height (Smith 2006). The structures of sensitivities are consistent with the axisymmetric cross-section. In addition, there are some negative sensitivities in the mid-troposphere of the rainband regions. For P2 (Fig. 5.11b) and P3 (Fig. 5.11c), structures of sensitivities are very similar to the structures of sensitivity in P1. But sensitivities in P2 and P3 are larger than the sensitivity shown in P1.

In general, we would have a stronger hurricane if potential temperature in the eye from lower- to upper-troposphere or in the rainband region from lower- to mid-troposphere were increased.

d. Sensitivity to mixing ratio

1) HORIZONTAL DISTRIBUTION

Figure 5.12 shows the horizontal distributions of all-level vertically averaged sensitivities to mixing ratio, *r*. During P1 (Figure 5.12a), there are large positive sensitivities in the cyclone center and the banded outer region (*i.e.* rainband regions) of the TC, with maxima west and south of the hurricane. However, sensitivities are small in the eyewall region encircling the eye as an annulus. This structure is consistent with the ensemble sensitivity results of Brown and Hakim (2015). There are also some spiral banded structures, which were also observed by Doyle (2012) and Brown and Hakim (2015). The structures of sensitivities to *r* are similar to sensitivities to θ. An increase of moisture in the eye and the rainband regions could intensify the hurricane.

During P2 (Figure 5.12b), structures of sensitivities are similar to the sensitivities in P1, except that the maxima of sensitivities are in the southwest and center of the hurricane. During P3 (Figure 5.12c), sensitivities have similar structures of sensitivities in P1 and P2,

there are strong sensitivities south of the hurricane. But alternating sensitivities in the base of the trough are the strongest, which could mean that interactions between the hurricane and the mid-latitude trough could influence ultimately the hurricane intensity.

Figure 5.13 shows the horizontal distributions of sensitivities to *r* at 850 hPa. During P1 (Figure 5.13a), sensitivities are positive in the cyclone center and the rainband regions, with maxima west of the hurricane where θ_e is relatively small (not shown). So increase of humidity in the cyclone center and the rainband regions could intensify the hurricane, especially closer to the regions of low θ_e. During P2 (Fig. 5.13b), sensitivities are positive in the cyclone center and the rainband regions with maxima southwest of the hurricane (*i.e.*, closer to regions of low θ_e). During P3 (Fig. 5.13c), sensitivities are positive in the cyclone center and the rainband region with strong values south of the hurricane (*i.e.*, closer to regions of low θ_e). However, the maxima of sensitivities are located in the base of the trough, which is consistent with the vertically averaged sensitivities.

In general, there are positive sensitivities to *r* in the cyclone center and rainband regions. Strong sensitivities are on the side closer to the regions of low θ_e of the control simulation. What is more, there are strong sensitivities in the space between the trough and the hurricane, and in the base of the trough. This indicates that mid-latitude may influence TC intensity.

2) RADIAL CROSS-SECTION

Figure 5.14 shows the radial cross-sections of sensitivities to *r*. During P1 (Fig. 5.14a), there are positive sensitivities in the eye (at 1-50 km) and rainband regions (*i.e.* 1-7 km more than 100 km from the cyclone center). This pattern is also observed by Brown and Hakim (2015). The maxima of sensitivities are located at 3-6 km 150-500 km from the cyclone center. In addition, sensitivities slope inward with height in the lower-tropospheric rainband regions, which corresponds to the slope of the boundary between cyclonic and anticyclonic circulation. Therefore, to intensify the hurricane, we would increase water vapor mixing ratio in the eye from the lower- to upper-troposphere, and in the rainband regions from lower- to mid-troposphere.

An explanation for the structures follows: an increase in water vapor mixing ratio could increase latent heat release associated with condensation, thereby increasing θ and air parcel buoyancy. An increase of buoyancy in the eye would reduce the downdraft in the eye and the

central pressure (Smith 2006). Mid-level entrainment and low-level transport of warmer and more moist eye air into the eyewall would enhance the convection in the eyewall (Persing and Montgomery 2003, and Cram et al. 2007). What is more, increase of buoyancy in the rainband regions would enhance the convection, and the inflow above the boundary layer according to Sawyer-Eliassen equation (Fudeyasu and Wang 2011). Therefore, the enhanced inflow can transport more heat into the eyewall, and enhance the eyewall convection (Riemer et al. 2010). Moreover, the inflow could transport more angular momentum toward the core, and spin up the rainband regions (Persing et al. 2013, Montgomery and Smith 2017). So the hurricane is intensified.

Overall, the structures of sensitivities to *r* are similar to the sensitivities for θ. We also know that: an increase of *r* and q individually or jointly are associated with increases in equivalent potential temperature (θ_e): $\theta_e = T\left(\frac{P_0}{P_d}\right)^{R_d/(c_{pd}+r_t c_l)} exp\left[\frac{l_v r_v}{(c_{pd}+r_t c_l)T}\right]$. So we can combine the sensitivities to r with the sensitivities to θ, and study the effects of equivalent potential temperature (θ_e) on TC intensity. Therefore, we can say that increase of θ_e in the eye from lower- to upper-troposphere, and in the rainband regions from lower- to mid-troposphere could intensify the hurricane. Emanuel (1991) notes that an increase of moist entropy (*i.e.*, θ_e) in the mid-troposphere could intensify the hurricane, since the import of low-entropy air from the mid-level into the boundary layer (with high-entropy) by the downdrafts could no longer decrease the entropy of the boundary layer as efficiently. Then the entropy of the boundary layer air and temperature of the lower- to mid-level air would increase together. Then the hurricane intensifies.

Structures of sensitivities in P2 and P3 are similar to the sensitivities in P1. For P2 (Fig. 5.14b), the maxima of initial condition sensitivities are located at 2-7 km above the surface in the cyclone center, and at elevations of 3-6 km some 250-450 km from center, which are stronger than the sensitivities in P1. Besides, the sensitivities in the rainband regions are located farther from the cyclone center than the sensitivities in P1. For P3 (Fig. 5.14c), sensitivities to *r* are the largest at 3-6 km in the cyclone center (0-50 km from the center), and at 1-4 km 100-500 km from the center. The sensitivities in the rainband regions are located lower and weaker than the sensitivities during P1 and P2.

To sum up, strong positive sensitivities to mixing ratio are located in the cyclone center from lower- to upper-troposphere, and in the rainband regions from lower- to mid-troposphere. Sensitivities in the lower-tropospheric rainband regions slope inward. Overall, the structures of sensitivities to *r* are similar to the structures of sensitivity to θ. Given that the sensitivities to both *r* and θ are predominately positive, positive perturbations to *r* and θ ***and hence*** $\boldsymbol{\theta_e}$ in the eye and in the rainband regions from lower- to mid-troposphere would intensify Irma in the simulations.

3) CROSS-SECTION

Figure 5.15 shows the cross-sections of sensitivities to *r*. For P1 (Fig. 5.15a), sensitivities to water vapor mixing ratio are positive in the cyclone center and lower- to upper-troposphere of rainband regions. Maxima of sensitivities are located in the mid-tropospheric rainband regions. Moreover, there are positive sensitivities in the outer region above 15 km, which may relate to the upper-level outflow. Sensitivities also slope inward with height in the rainband regions. Structures of sensitivities in P2 (Figure 5.15b) and P3 (Figure 5.15c) are similar to sensitivities in P1.

In general, sensitivities to *r* are similar to sensitivities to θ, which indicate that both suggest they are related by θ_e. Sensitivities to *r* are positive and large in the cyclone center from lower- to upper-troposphere, and in the rainband regions from lower- to mid-troposphere. Sensitivities are larger on the side closer to dry environment in the lower-levels. This may be a compensation for low θ_e.

e. Discussion

In this chapter, we described the sensitivities to wind, divergence, vorticity, potential temperature, and water vapor mixing ratio. We identified some factors that could intensify simulations of Irma over three periods. The essential messages conveyed by the sensitivities to the initial state were similar for all three periods:

1. An increase in cyclonic vorticity that spirals anticyclonically into the cyclone center while leaning back against the vortex flow would intensify the TC. This pattern corresponds to perturbations of vorticity that could grow the most over finite time and represent a generalization described by Nolan and Farrell (1999) of the Orr

(1907) mechanism. This distribution of an implied vorticity is related to a perturbation to the primary (azimuthal circulation) outside of the radius of maximum winds;

2. An increase of the secondary circulation at the initial time does not appear to be relevant in intensifying the TC. The reason may be that the secondary circulation is a result of stronger hurricane, not a cause of a stronger hurricane.
3. An increase of θ_e in the eye, as well as in the rainband regions from the lower- to mid-troposphere could strengthen the hurricane, particularly on the sides of a TC closer to the lowest θ_e environment. The explanation follows: an increase of θ_e increase the parcel buoyancy within the eye, and decreases the downdraft and the central pressure; mid-level entrainment and low-level transport of higher-entropy eye air into the eyewall would enhance the convection in the eyewall and intensify the hurricane. Increases of θ_e in the lower- to mid-tropospheric rainband regions enhance the convection in the rainband regions and the inflow above the boundary layer (Fudeyasu and Wang 2011). The enhanced inflow transports higher-entropy rainband air into the eyewall and enhances the eyewall convection leading to a stronger hurricane (Emanuel 1991, Riemer et al. 2010); the inflow also transports higher angular momentum toward the core, which spins up the primary circulation in the rainband regions (Persing et al. 2013, Montgomery and Smith 2017).

For P3, there are strong alternating vertically averaged sensitivities to θ and r in the base of the trough (Figs. 5.16 a and c) with similar patterns, which indicates that changes of θ and r in some locations of the trough could change intensity of the hurricane significantly. Figure 5.16b and d show the vertical cross-sections of sensitivities to θ and r. The sensitivities to θ and r are mainly in the boundary layer (0-2 km), and they have similar structures. More work is needed to explore the interactions between the TC and the mid-latitude trough.

In the next section, we use the sensitivities just described to create optimal perturbations to the initial conditions to study the impacts of such perturbations on the development of Irma.

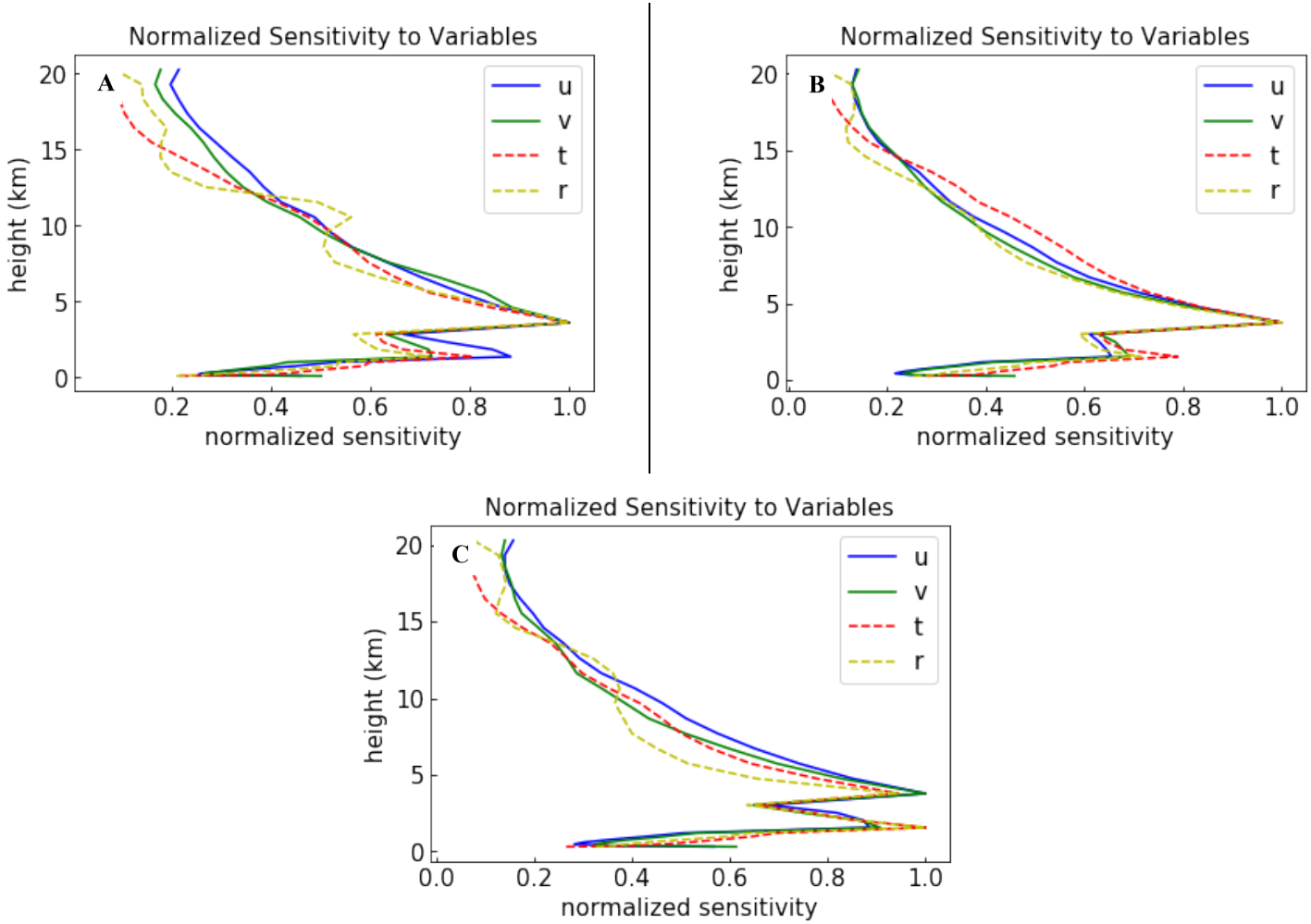

Figure 5.1. Profiles of normalized sensitivity to zonal wind, meridional wind, potential temperature and mixing ratio at initial time of 24h period cases beginning (a) 0000 UTC 05 September 2017, (b) 0000 UTC 09 September 2017, and (c) 0000 UTC 10 September 2017. The u, v, t, r, represent zonal wind, meridional wind, potential temperature and

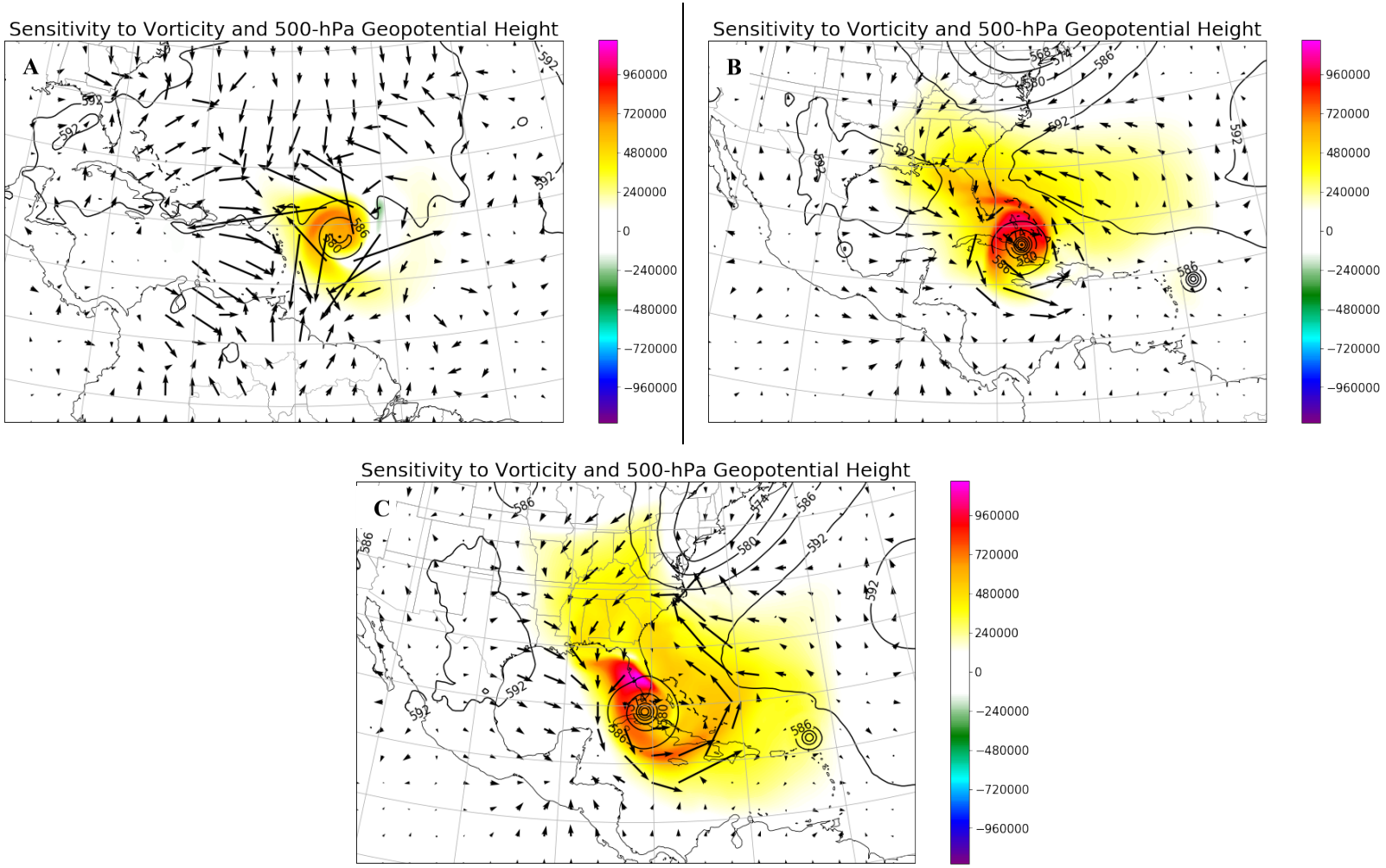

Figure 5.2. The 14th level adjoint sensitivity to vorticity (color scale with interval every 10000 Pa $(s^{-1})^{-1}$), sensitivity to horizontal winds (vectors), and 500-hPa geopotential height (solid line with an interval of 60 m) at initial time of 24h period cases beginning at (a) 0000 UTC 05 September 2017, (b) 0000 UTC 09 September 2017, and (c) 0000 UTC 10 September

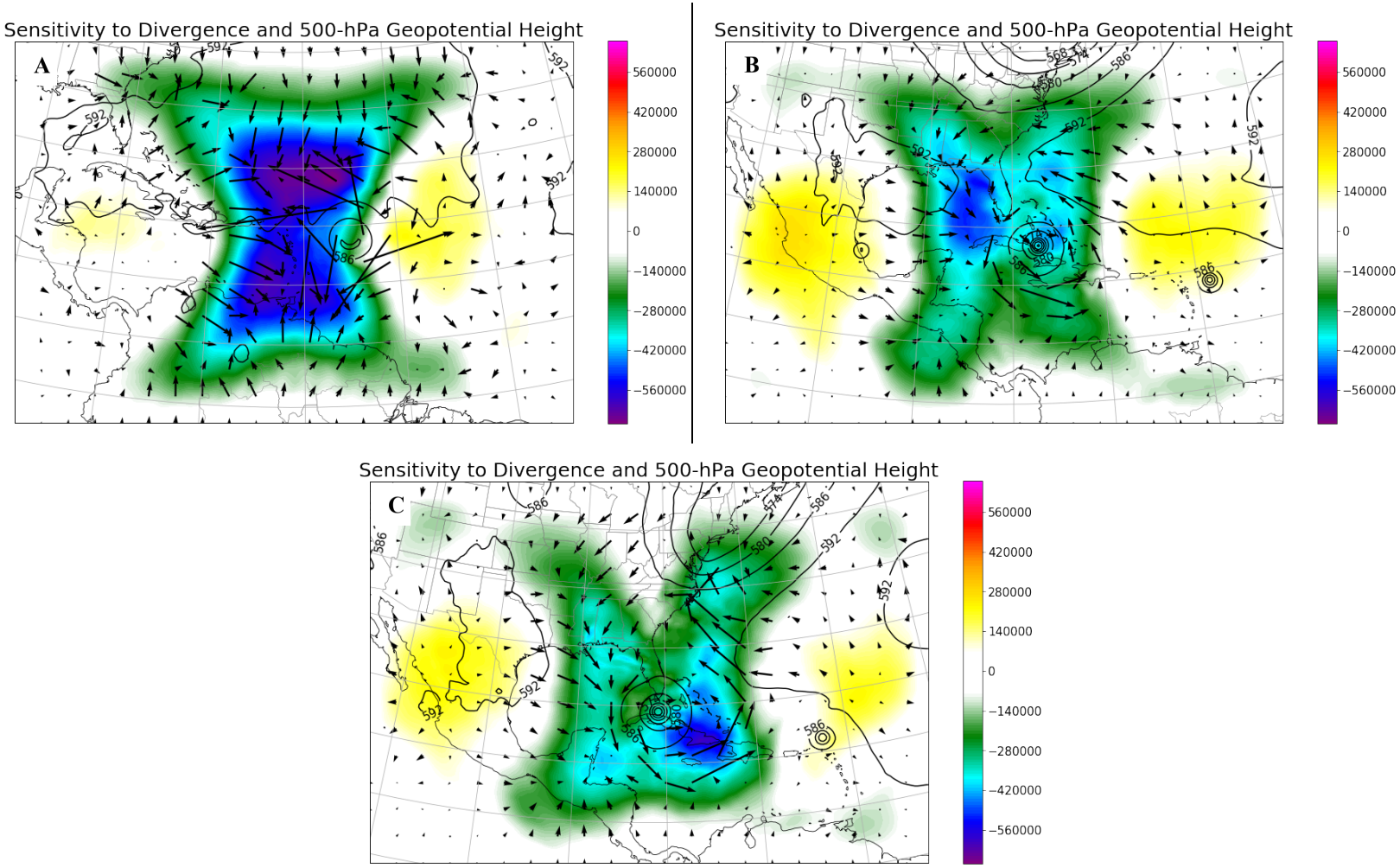

Figure 5.3. The 14th level adjoint sensitivity to divergence (color scale with interval every 10000 Pa $(s^{-1})^{-1}$), sensitivities to horizontal winds (vectors), and 500-hPa geopotential height (solid line with an interval of 60 m) at initial time of 24h period cases beginning at (a) 0000 UTC 05 September 2017, (b) 0000 UTC 09 September 2017, and (c) 0000 UTC 10 September

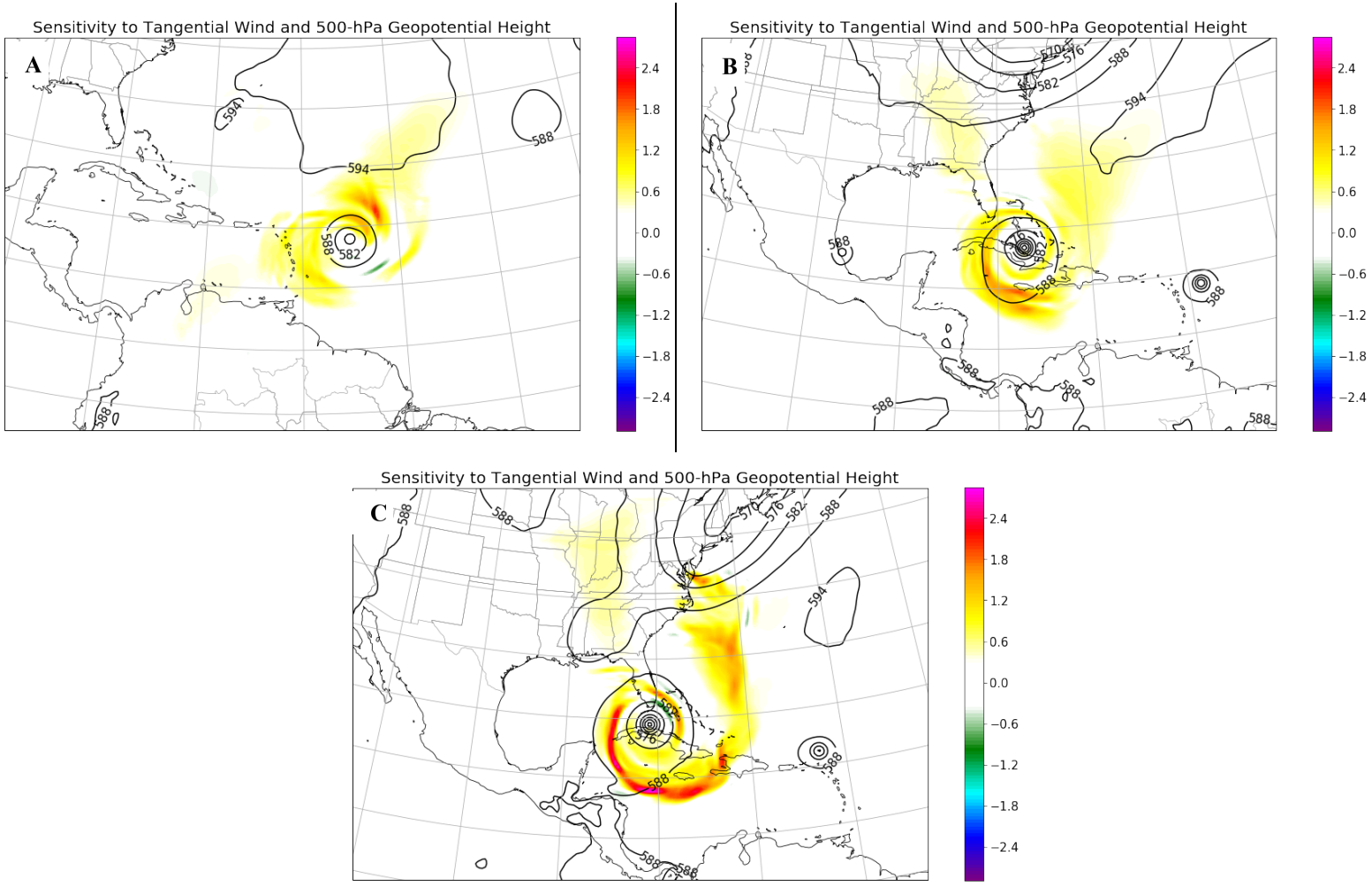

Figure 5.4. The adjoint sensitivity to tangential wind (color scale with interval every 0.05 $\mathrm{Pa(m\ s^{-1})^{-1}}$), sensitivities and 500-hPa geopotential height (solid line with an interval of 60 m) at initial time of 24h period cases beginning at (a) 0000 UTC 05 September 2017, (b) 0000 UTC 09 September 2017, and (c) 0000 UTC 10 September 2017.

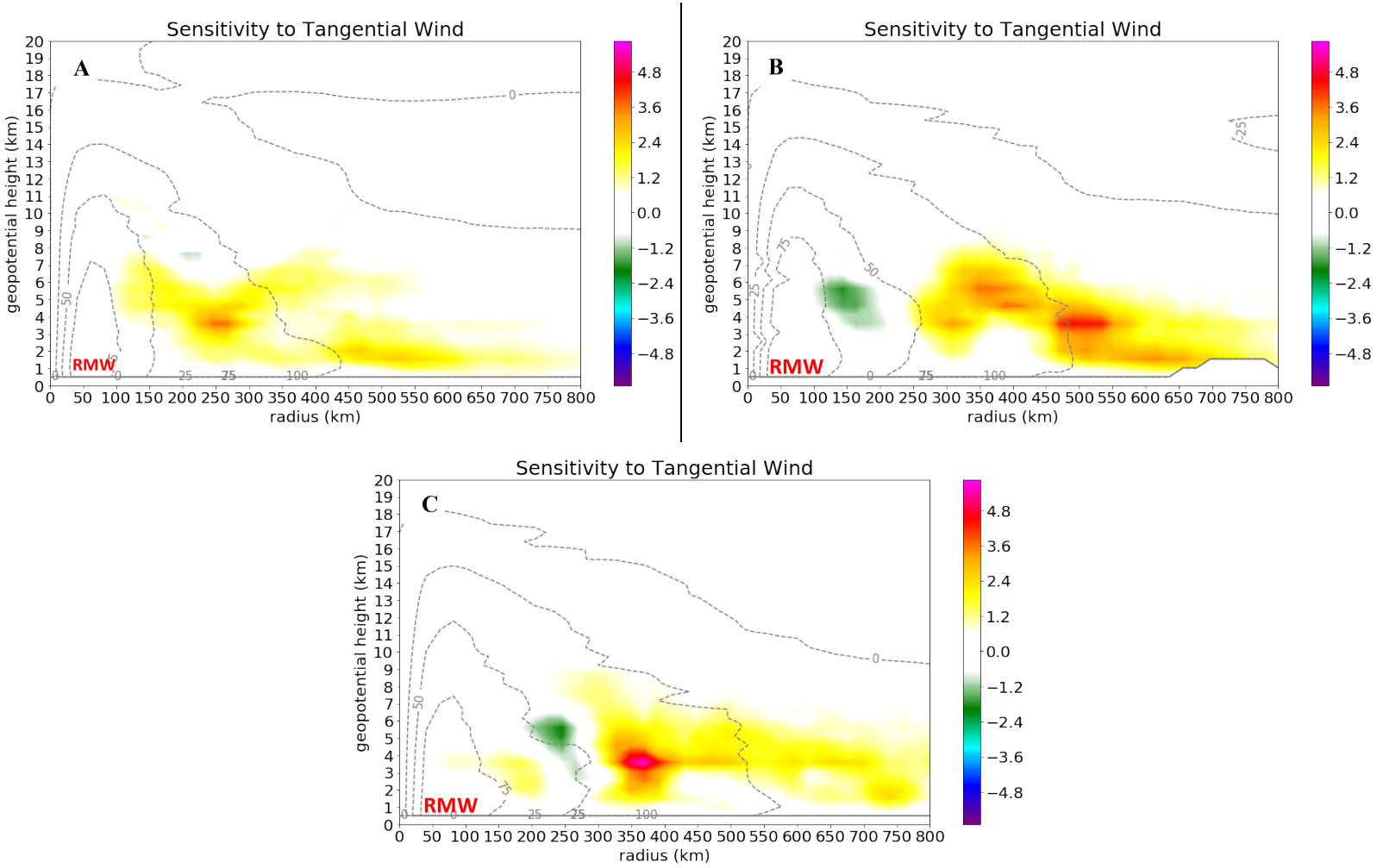

Figure 5.5. Cross-section of azimuthally averaged sensitivity to tangential wind (color scale with interval every 0.05 Pa$(\mathrm{m\ s^{-1}})^{-1}$) and tangential wind (dashed line with an interval of 25 m $\mathrm{s^{-1}}$) at initial time of 24h period cases beginning at (a) 0000 UTC 05 September 2017, (b) 0000 UTC 09 September 2017, and (c) 0000 UTC 10 September 2017.

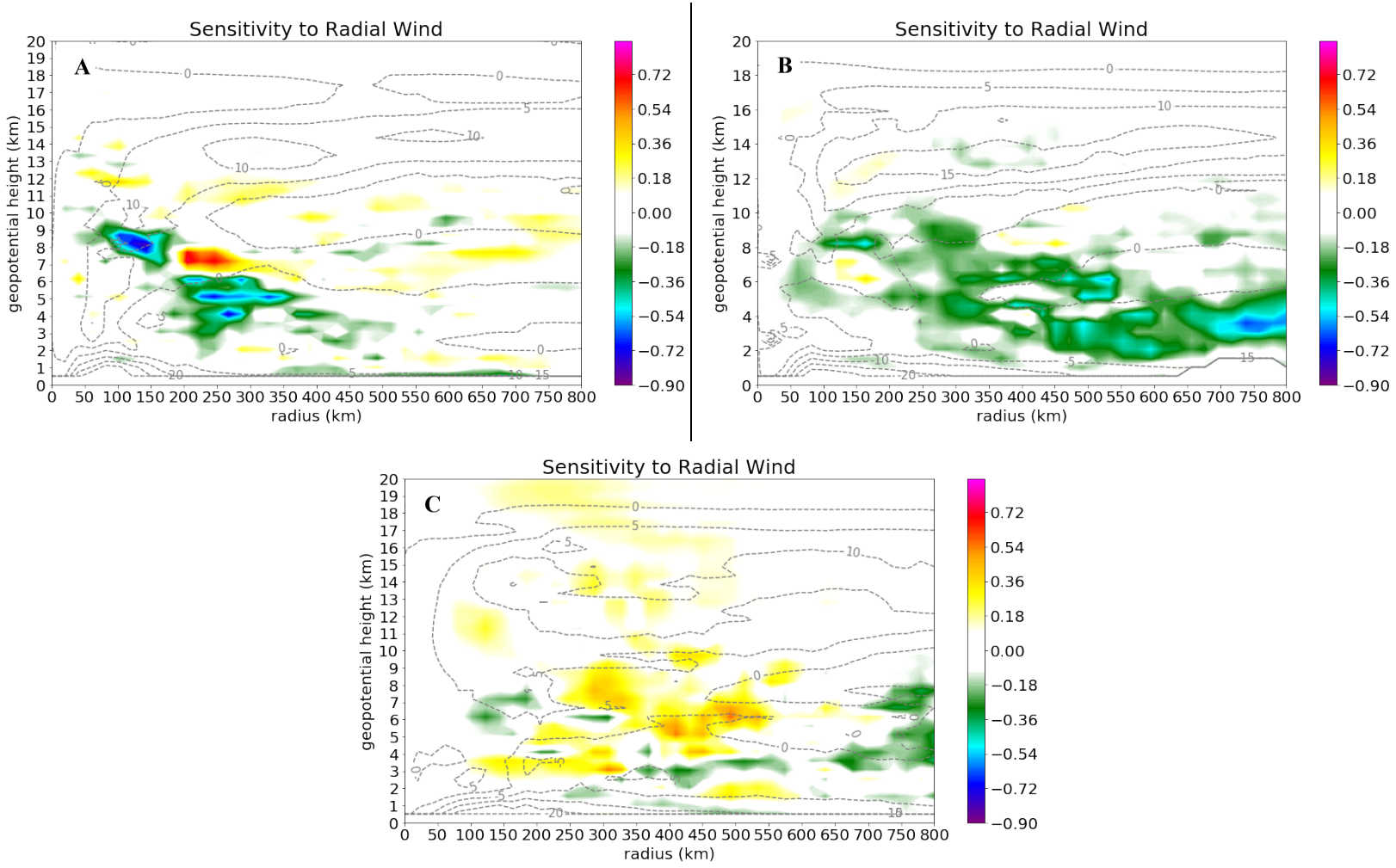

Figure 5.6. As in Figure 5.3, but for sensitivity to radial wind (color scale with interval every 0.005 $\mathrm{Pa(m\,s^{-1})^{-1}}$) and tangential wind (dashed line with an interval of 5 $\mathrm{m\,s^{-1}}$).

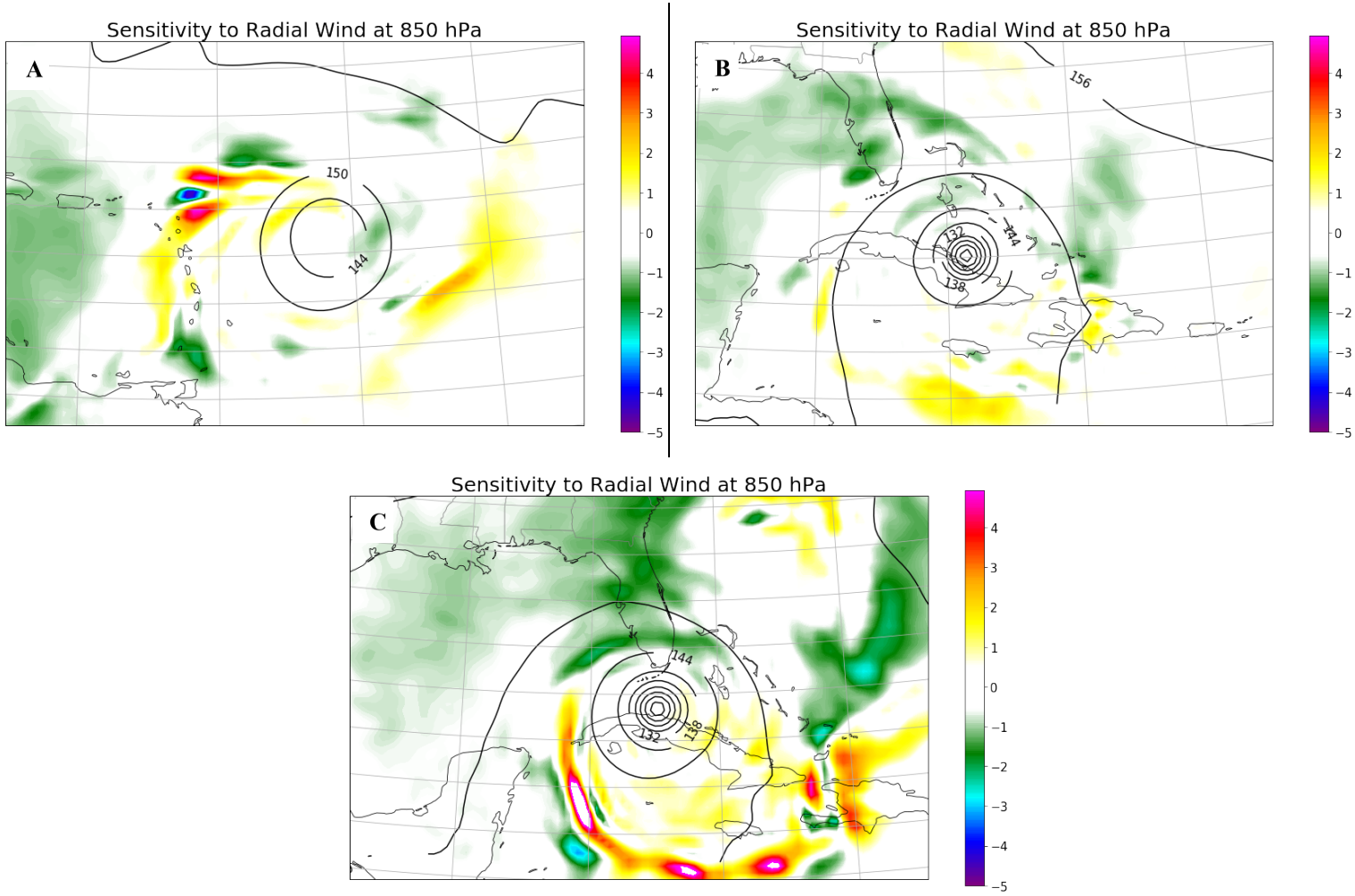

Figure 5.7. Adjoint sensitivity to radial wind (color scale with interval every 0.1 Pa k^{-1}) at 850 hPa (solid line with an interval of 60 m) at initial time of 24h period cases beginning (a) 0000 UTC 05 September 2017, (b) 0000 UTC 09 September 2017, and (c) 0000 UTC 10 September 2017.

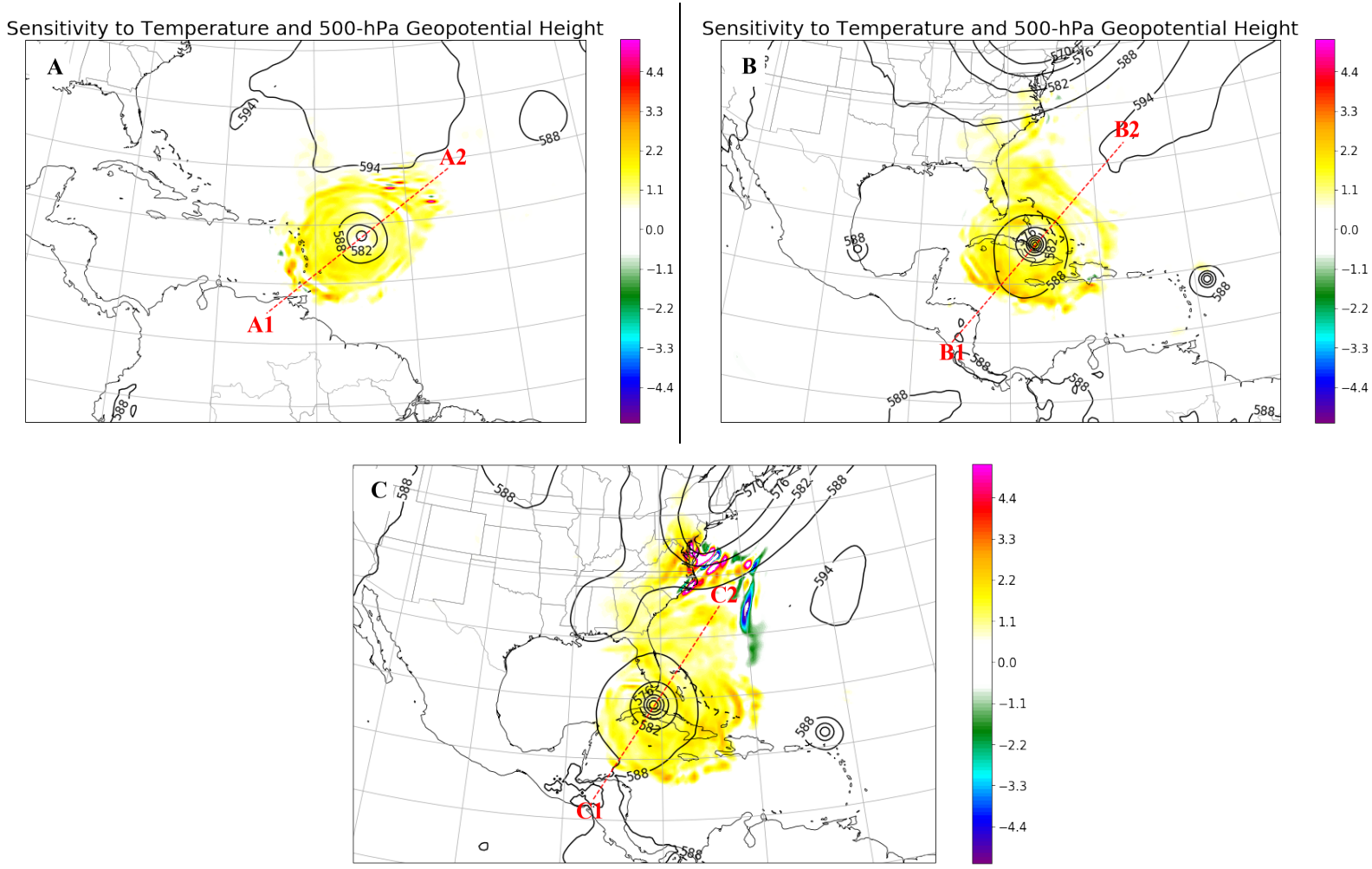

Figure 5.8. Vertically averaged adjoint sensitivity to potential temperature (color scale with interval every 0.1 Pa k^{-1}) and 500-hPa geopotential height (solid line with an interval of 60 m) at initial time of 24h period cases beginning (a) 0000 UTC 05 September 2017, (b) 0000 UTC 09 September 2017, and (c) 0000 UTC 10 September 2017.

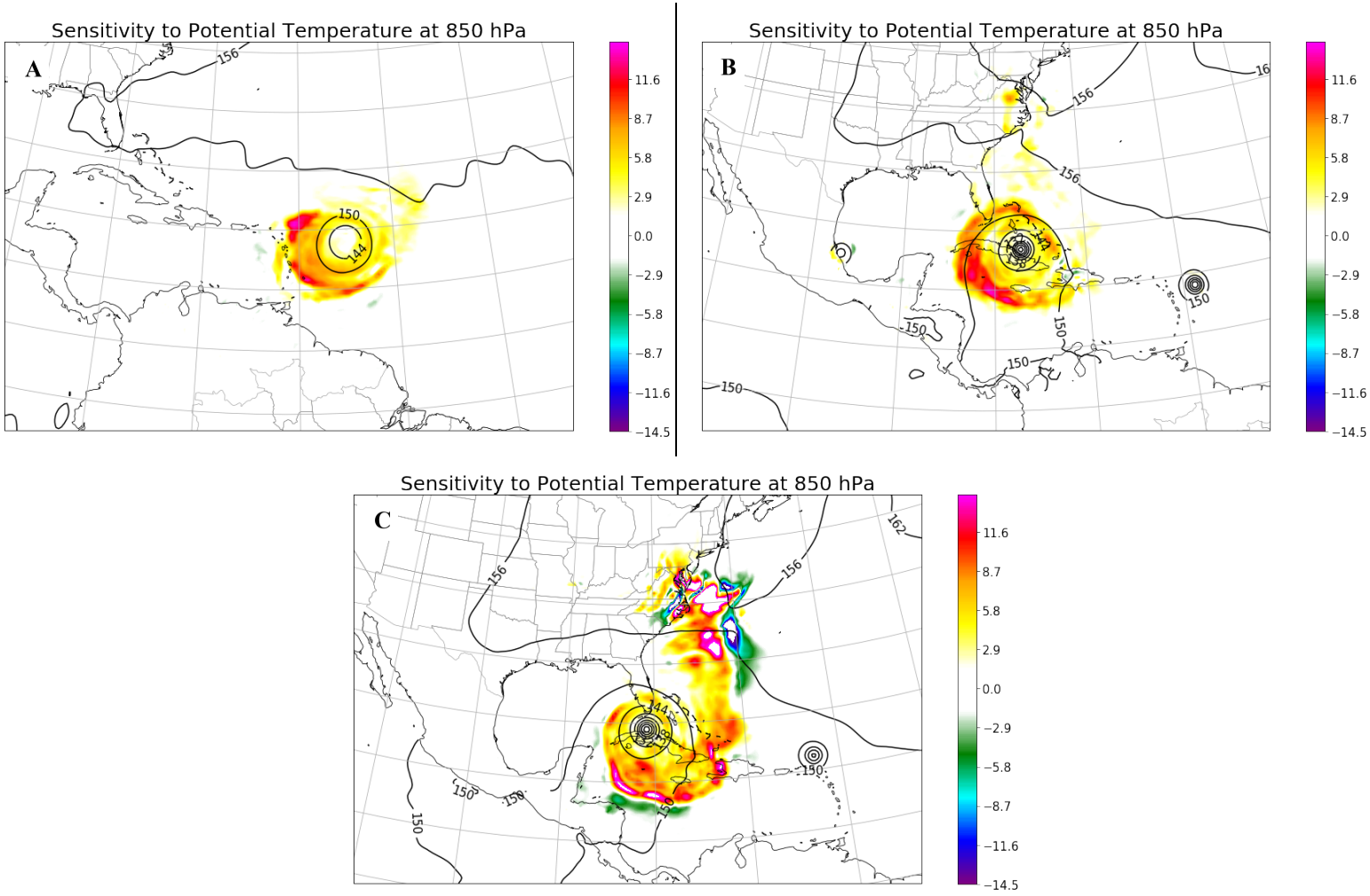

Figure 5.9. Adjoint sensitivity to potential temperature (color scale with interval every 0.1 Pa k^{-1}) at 850 hPa (solid line with an interval of 60 m) at initial time of 24h period cases beginning (a) 0000 UTC 05 September 2017, (b) 0000 UTC 09 September 2017, and (c) 0000 UTC 10 September 2017.

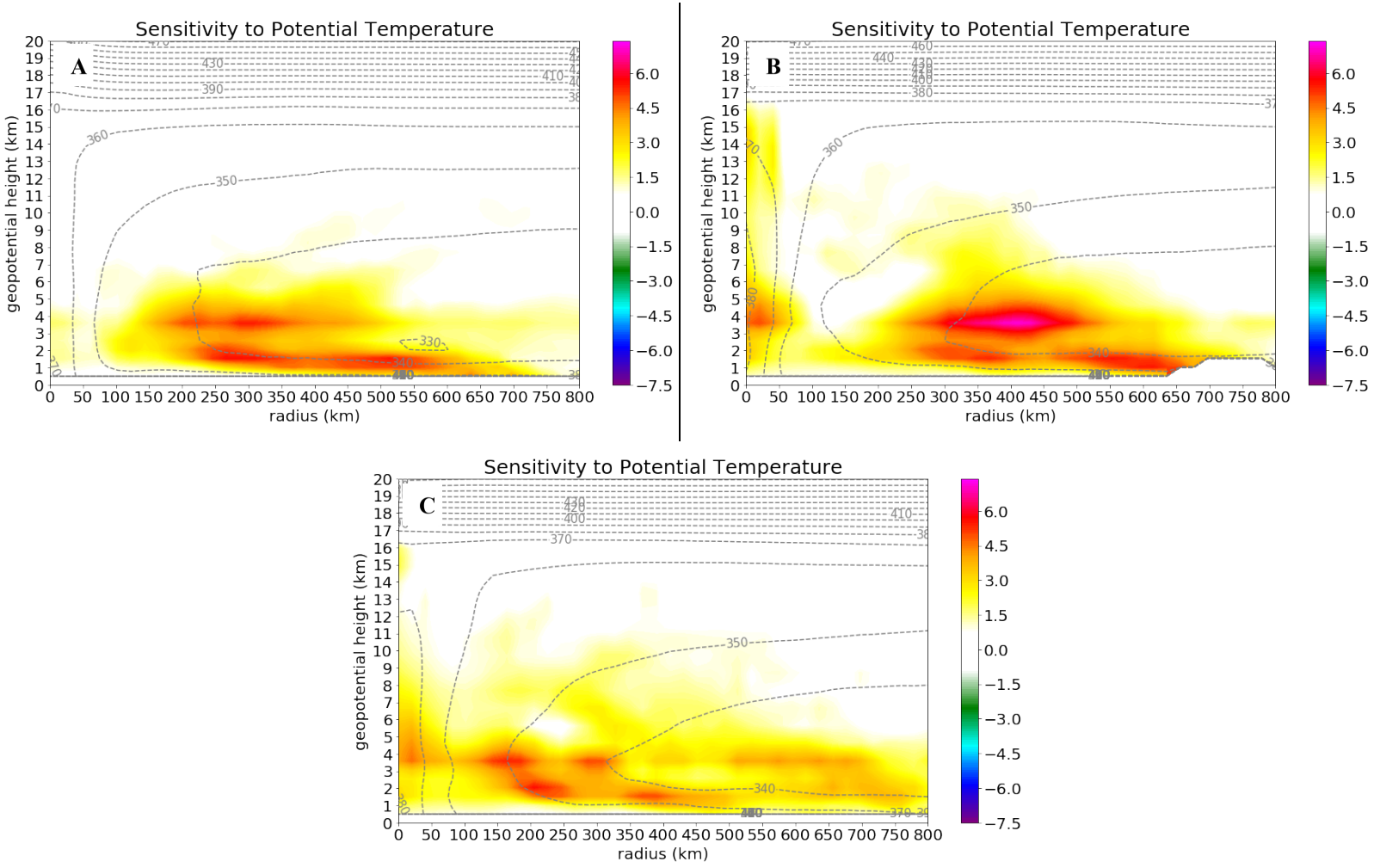

Figure 5.10. Cross-section of azimuthally averaged sensitivity to potential temperature (color scale with interval every 0.1 Pa k^{-1}) and equivalent potential temperature (dashed line with an interval of 10 k) at initial time of 24h period cases beginning at (a) 0000 UTC 05 September 2017, (b) 0000 UTC 09 September 2017, and (c) 0000 UTC 10 September 2017.

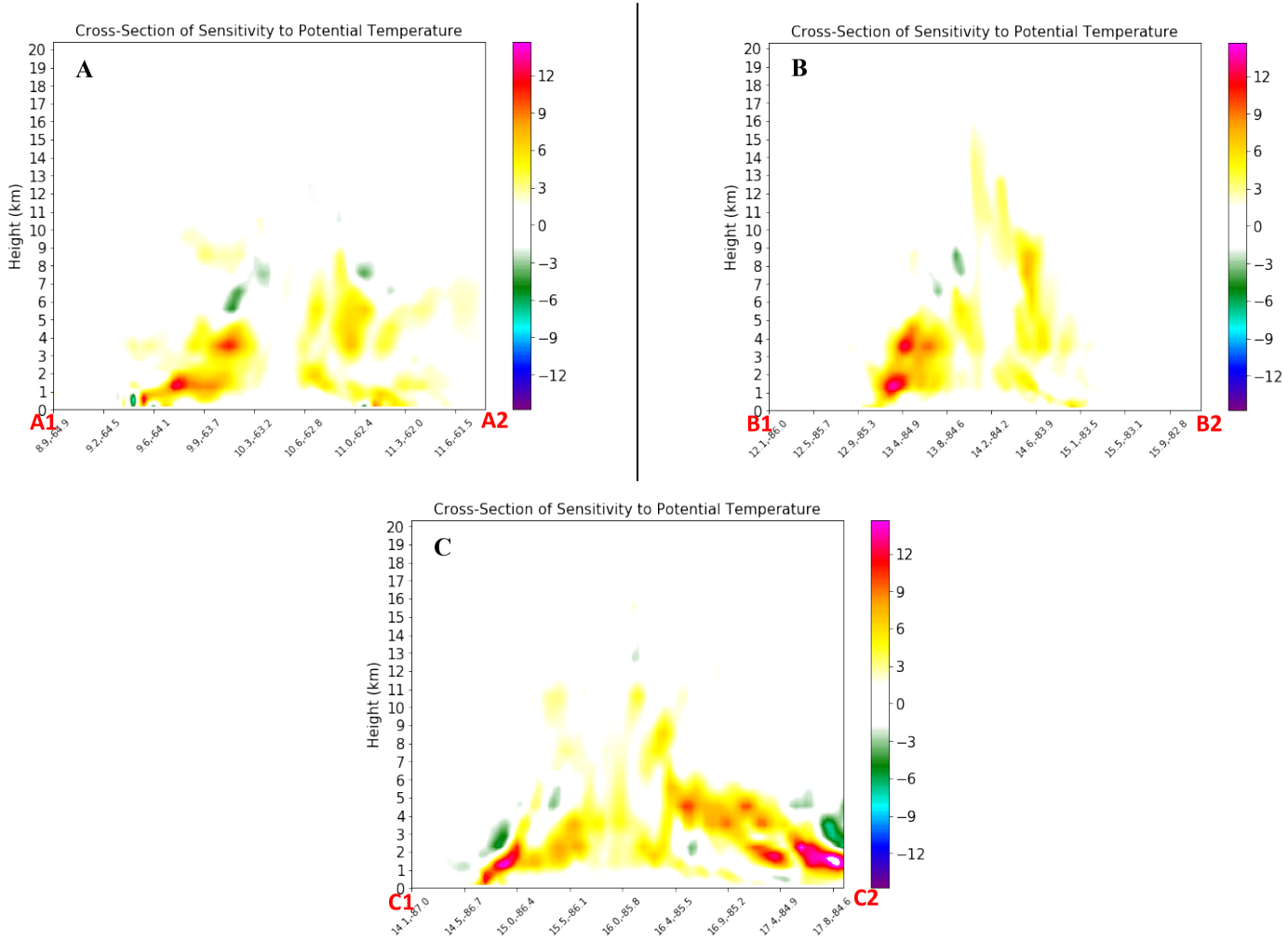

Figure 5.11. Cross-section of adjoint sensitivity to potential temperature (color scale with interval every 0.1 Pa k^{-1}) at initial time of 24h period cases beginning at (a) 0000 UTC 05 September 2017, (b) 0000 UTC 09 September 2017, and (c) 0000 UTC 10 September 2017. Location shown in Fig. 5.8a-c respectively.

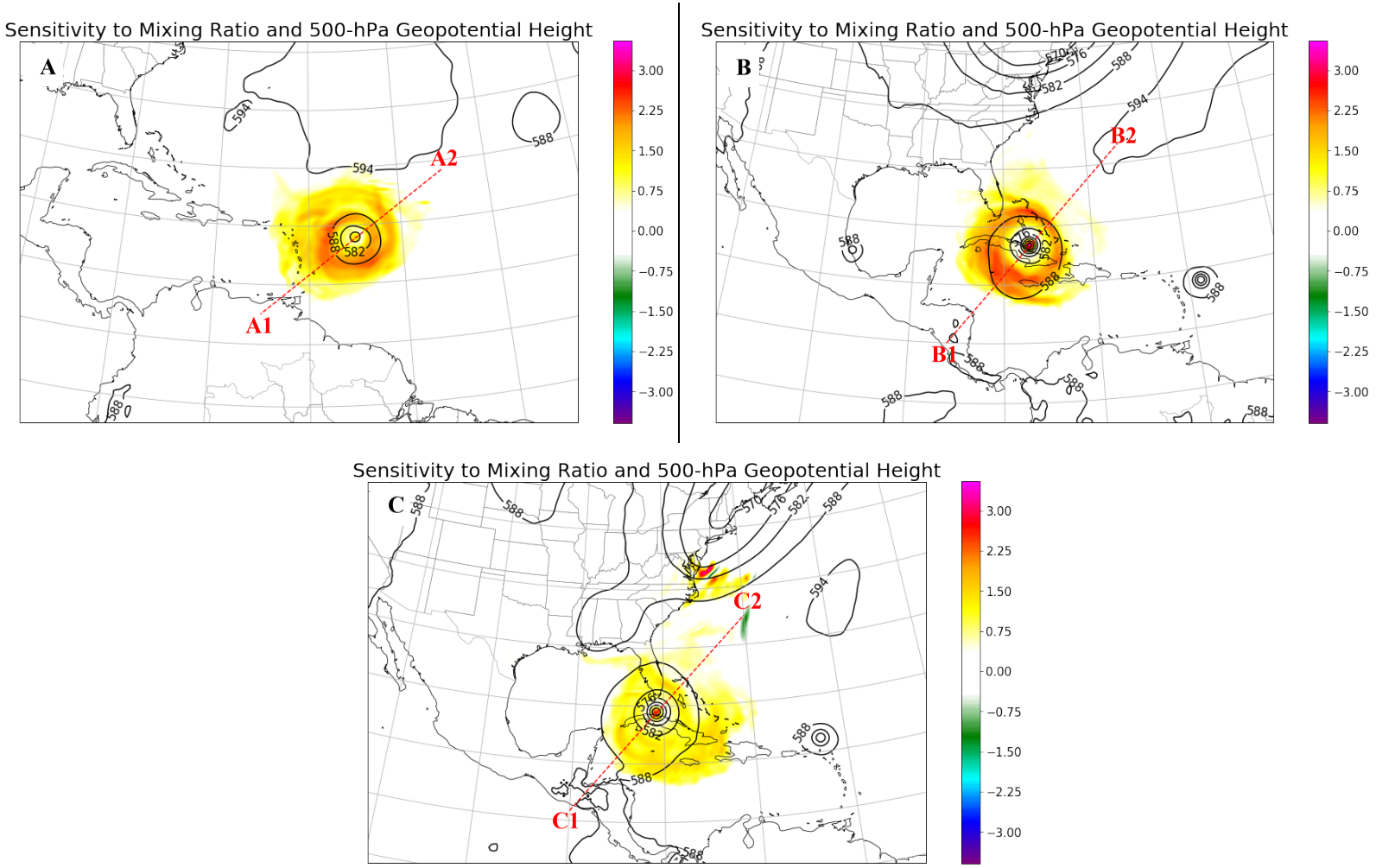

Figure 5.12. As in Figure 5.8, but for sensitivity to mixing ratio (color scale with interval every 0.05 Pa $(\mathrm{g\ kg^{-1}})^{-1}$).

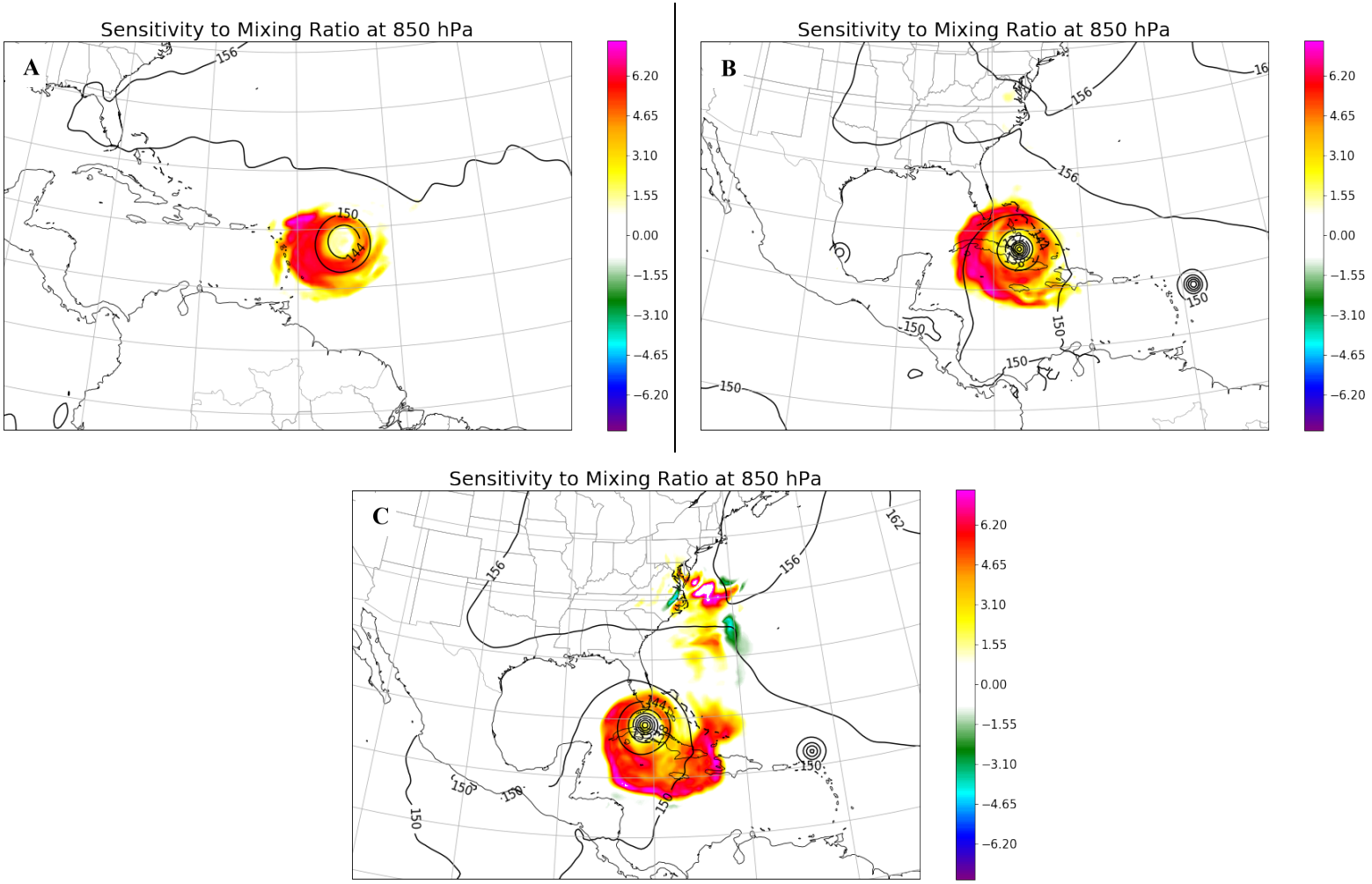

Figure 5.13. As in Figure 5.9, but for sensitivity to mixing ratio at 850 hPa (color scale with interval every 0.05 Pa $(\mathrm{g\,kg^{-1}})^{-1}$).

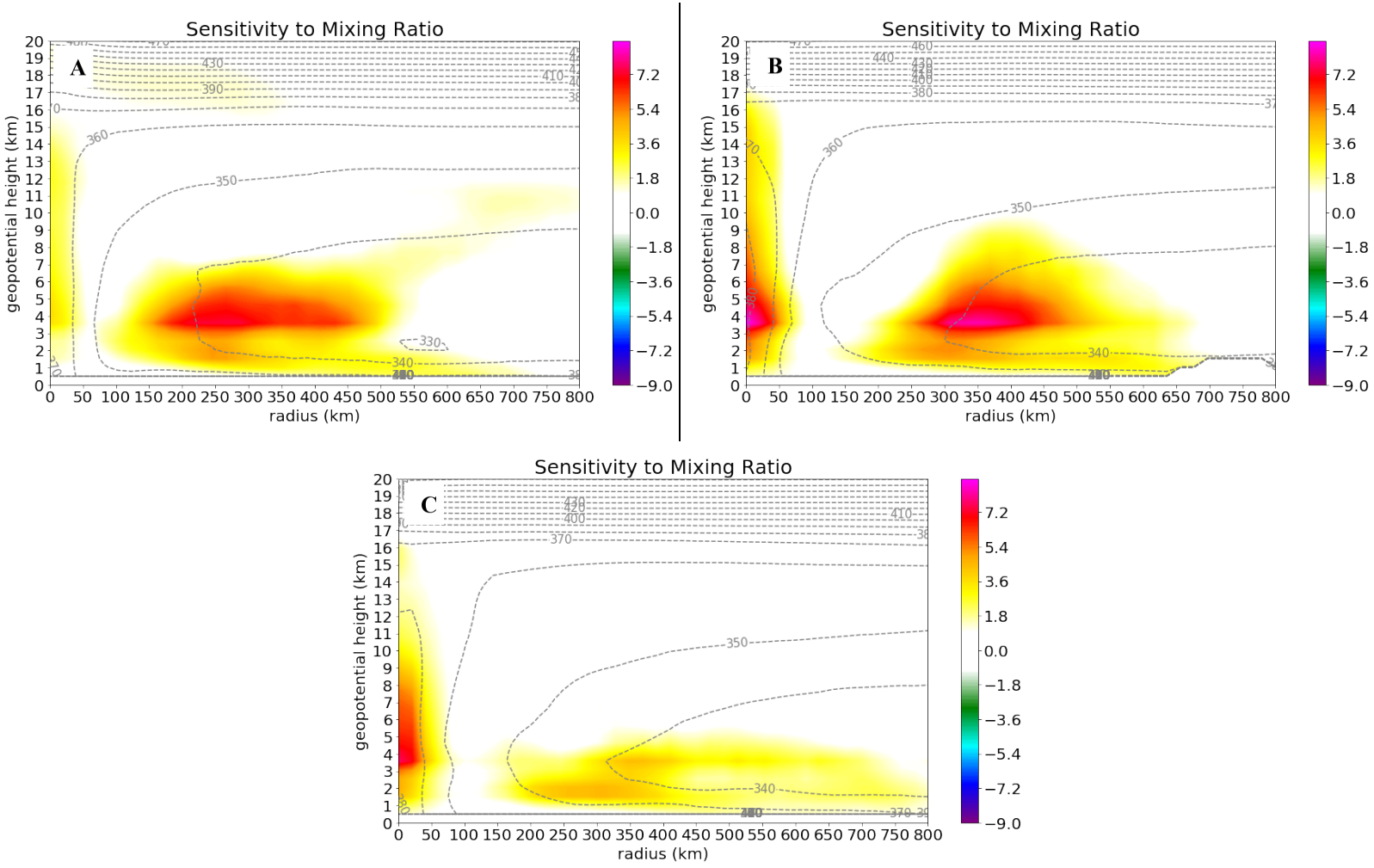

Figure 5.14. As in Figure 5.10, but for sensitivity to mixing ratio (color scale with interval every 0.05 Pa $(\mathrm{g\ kg^{-1}})^{-1}$).

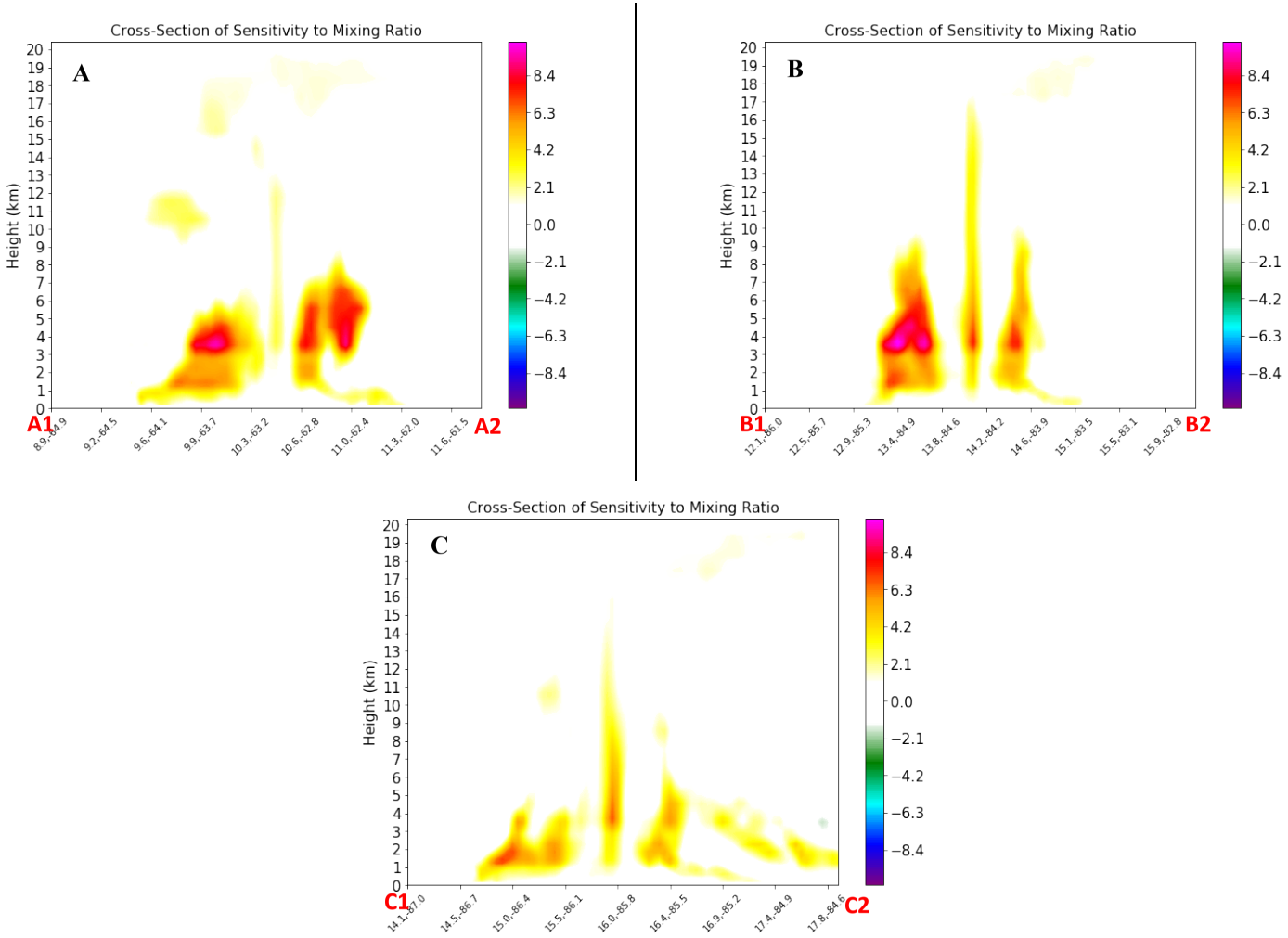

Figure 5.15. As in Figure 5.11, but for sensitivity to mixing ratio (color scale with interval every 0.1 Pa $(\mathrm{g\ kg^{-1}})^{-1}$). Location shown in Fig. 5.13a-c respectively.

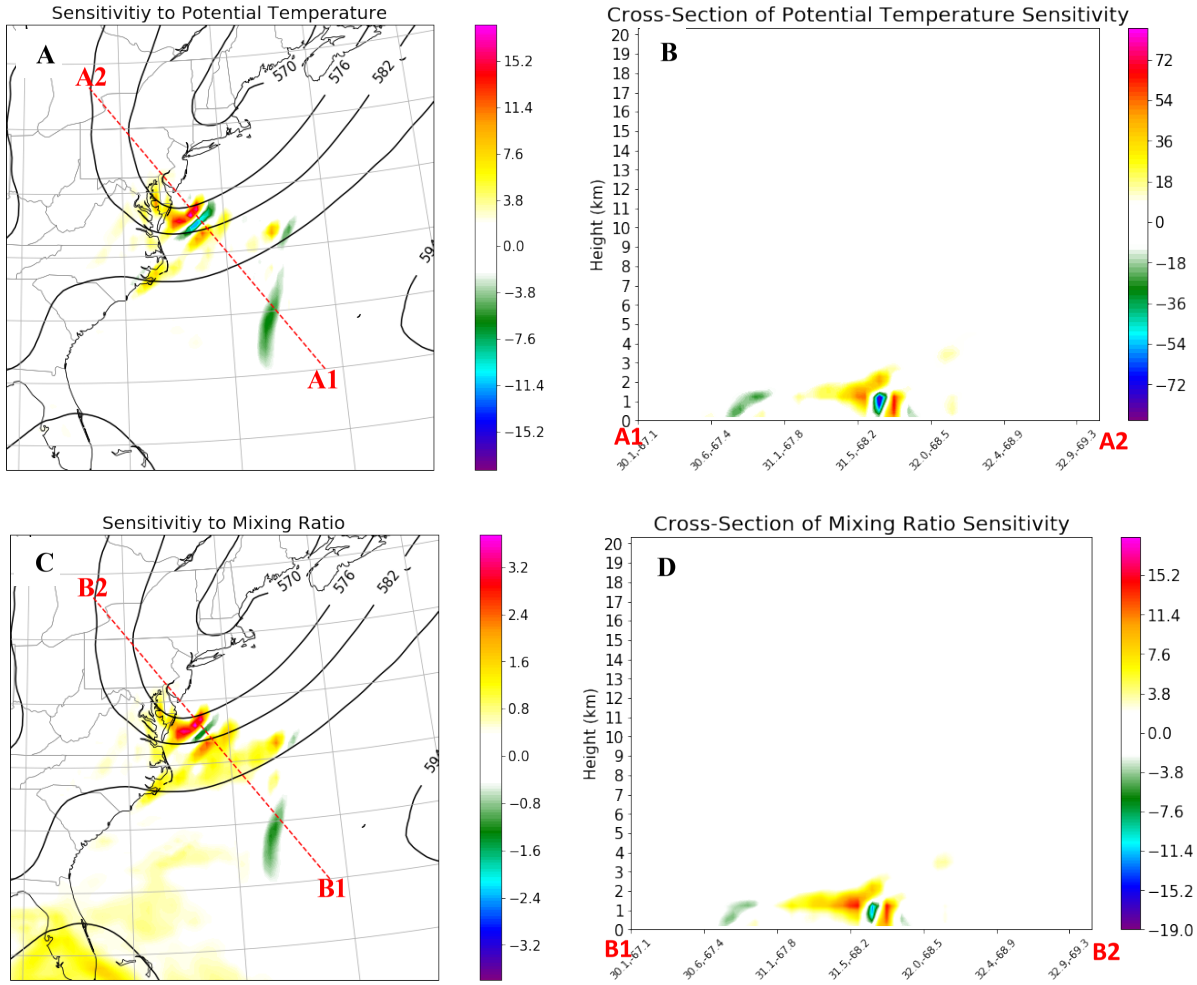

Figure 5.16. Adjoint sensitivity in the base of the trough at initial time of 24h period case beginning at 0000 UTC 10 September 2017. (a) vertically averaged sensitivities to potential temperature (color scale with interval every 0.2 Pa k^{-1}), (b) vertical cross-section of sensitivity to potential temperature (color scale with interval every 1.0 Pa k^{-1}; location shown in Fig. 5.17a), (c) vertically averaged sensitivity to mixing ratio (color scale with interval every 0.05 Pa $(g\ kg^{-1})^{-1}$, (d) vertical cross-section of sensitivity to mixing ratio (color scale with interval every 0.1 Pa $(g\ kg^{-1})^{-1}$; location shown in Fig. 5.17c).

6. Perturbation analysis

a. Overview

In this chapter, we study the impacts of optimal initial condition perturbations (described in Chapter 2) on the nonlinear model forecast trajectory for Hurricane Irma. Sensitivity experiments were performed to either intensify or weaken simulations of Irma. The purpose of these perturbation studies is two-fold: 1) the evolution of the perturbations may give insight into interpretation of the sensitivities (because the perturbations are proportional to the sensitivities) and 2) the resulting change in the response function, R, compared to what was prescribed in the optimal perturbation equation (see Section 2c), provides valuable information about the relevance of the assumptions of linearity in the adjoint calculation.

While performing the first set of optimal perturbation experiments, a response function similar to that defined in Chapter 4 was used: the sum of the negative dry air mass in a box centered on the 24 hour position of the simulated hurricane. For our initial choice of a 12 × 12 gridpoint box we observed for period P1 that the ratios of the actual to the predicted response function changes ($i.e.$, $\Delta R/\delta R$) were very small for intensified cases, such as 18.01% and 11.40%, while the ratios were much larger than 100% for weakened cases, such as 204.65% and 225.36%. If the perturbation evolution were linear, the ratio would be 100%. It was observed that the perturbed hurricane shifted northward nearly 1° during the 24h simulation – *out of the response function box*. Dr. Brett Hoover suggested a reason for these unanticipated results might be that the response function box was not large enough to capture the evolved perturbation mass field associated with the initial perturbation. Because the response function was defined by a box centered on the hurricane's position *with the hurricane in the box*, if the hurricane were to exit the box, the response function would change discontinuously and R would not be well-defined or representative of the cyclone intensity. We chose a larger box (25×25) centered at the cyclone center at 24h of simulation, and repeated the simulation and calculation. The results became more rational.

In this work, optimal perturbation experiments mainly include three type of perturbations – each designed to minimize a different measure of initial perturbation energy. The first type is a kinetic energy perturbation (KE, involving perturbations to only the horizontal wind field). The second type is a dry energy (DE, kinetic and internal) perturbation

(involving perturbations to both the horizontal wind and temperature fields). The third type is a total energy (TE, dry and latent energy) perturbation (involving perturbations to the horizontal wind, temperature, and water vapor mixing ratio fields). For each type of perturbation, we performed six optimal perturbation experiments for changes of response function of -80000 Pa, -40000 Pa, -20000 Pa, +20000 Pa, +40000 Pa, +80000 Pa (hereinafter, -8, -2, -8, +2, +4 and +8 respectively). Recall that the response function was designed so that increases (decreases) in the response function correspond to stronger (weaker) simulations of Irma. For reference, because the response function box has 625 grid points, if the response function were to change by +40000 Pa, the average change of the dry air mass at each grid point would be -0.64 hPa.

b. Comparison of expected vs. observed response function changes

Figure 6.1 shows a scatter plot of the actual response change (ΔR) plotted against the predicted change (δR) at the final time for all three periods (Fig. 6.1a, P1; Fig. 6.1b, P2; Fig 6.1c, P3). For all three periods and for both weakening and intensifying optimal perturbations, it is evident that the optimal perturbations do, in fact, lead to the expected sign of the response function change. Furthermore, the actual changes of the response function are closer to the predicted changes for perturbations designed to weaken Irma than for perturbations designed to intensify Irma. From these results, we infer that the dynamics of weakening the simulated hurricane appear more linear than those associated with intensifying it. This result is consistent with that of Brown and Hakim (2015) using ensemble sensitivity analysis. In addition, for all cases, the actual and predicted changes of the response function are in closer agreement for KE type perturbations (blue circles) than in the cases of DE perturbations (red triangles) and TE perturbations (green stars). This result suggests that perturbations of horizontal winds are more responsible for changing of simulated hurricane intensity than perturbations of temperature and mixing ratio. Brown and Hakim (2015) reported a similar result.

c. Vertical profiles of evolved optimal perturbations at 24h optimization time

We define the normalized evolved optimal perturbation (EOP) of a given variable at a particular level as the ratio of horizontal average of the absolute value of the EOP of that

variable to the maximum of horizontal averages of the absolute value of the EOP of that variable over all levels. Figure 6.2 shows the vertical profiles of normalized EOP for all three periods. Values of the normalized EOP for the horizontal wind components decrease with height from surface to a minimum value at about 4 km. The minimum is most prominent for P1 (Fig. 6.2a) compared with profiles for P2 and P3 (Figs. 6.2b and c). The normalized EOP for the wind components have a double-peaked structure in the upper troposphere at 12 and 17km. The normalized EOP of potential temperature shares a 4km minimum with the EOP for horizontal wind, but unlike the normalized EOP for wind, has a single maximum at about 17km. Finally, unlike the EOP of horizontal winds and potential temperature, the normalized EOP for mixing ratio increases from the surface to a maximum value at 1 km and decreases monotonically above 1 km. The evolved normalized EOP amplitude structure for wind and potential temperature contrast starkly with that of the sensitivities (and by extension the initial condition perturbation) structure – recall (Fig. 5.1) that the amplitudes of the evolved perturbations were maximized in the lower troposphere initially with small amplitudes in the upper troposphere. This suggests an upward propagation of energy from the initial condition perturbations to the upper troposphere and lower stratosphere for wind and temperature.

We used the total energy norm to calculate the total energy of the +4 KE perturbations at the initial and final time of P1, P2, and P3. Figure 6.3 shows the vertical profiles of total energy for all three periods. Values of the total energy are the largest at the lower-troposphere; and P1's values are the largest, P3's are the smallest. Furthermore, the total energy grows from the initial time to the final time, especially at upper-troposphere. This suggests an upward propagation of total energy of perturbations from the lower-troposphere to the upper troposphere during the simulation period. This is also noted by Doyle et al. (2012), but for tropical cyclogenesis.

d. Structure and evolution of optimal perturbation for P1

In this section, for brevity, we focus on the results for the +4 KE perturbation for P1 because the results for other periods are similar. The discussion includes the evolved optimal perturbations (hereinafter, EOP) of dry air mass, potential temperature, mixing ratio, and equivalent potential temperature. Although we calculated a 24h sensitivity of a response

function to the initial conditions and used that sensitivity to calculate optimal perturbations to change that 24h response function, we run optimal perturbation experiments forward from 0h to 36h, and diagnose the evolution of initial optimal perturbations for the full 36h period. The additional 12 hours allows for an evaluation of whether the changes to the response function are lasting or ephemeral.

1) 36h EVOLUTION OF THE EOP FOR DRY AIR MASS

Figure 6.4 shows the evolution of the EOP for dry air mass every 6h from forecast hours 6 to 36. (Figs 6.4 a, b, c, d, e, and f respectively). In the first 12h, the EOP of μ "accumulates" north of Irma. After 18h, the EOP begins a cyclonic rotation about the hurricane center. After 24h, the rotation of the μ perturbation is interrupted – perhaps by interaction of the TC with the approaching Windward Islands. The amplitude of the EOP of μ increases as well. For optimals calculated for P2 and P3 the EOP of μ continues to rotate beyond 24h. This rotation resembles a wavenumber-one vortex Rossby wave (Smith 2006). The persistence of the EOP for dry mass beyond the optimization time of 24h is further evidence of the balanced, and lasting impact of the initial condition perturbation. There was no guarantee the optimal perturbation would have any impact beyond 24h. The emergence of balance is worthy of further study.

The EOP of the kinetic energy perturbation shown here are similar to the EOPs for DE and TE perturbations (not shown). Moreover, the EOP for a -4 KE EOP has almost the opposite signed structure as the +4 KE EOP (not shown) suggesting that the physical processes responsible for the evolution of the +/- 4 perturbations are relatively linear over 24h, and that application of the linear dynamics of the adjoint model is justified.

2) HORIZONTAL DISTRIBUTIONS OF EOP VARIABLES

Figure 6.5 shows the EOP for variables for the +4 kinetic energy perturbation case. In Figure 6.5a, the EOP for dry air mass (μ) is negative southwest of the hurricane and positive northeast of the hurricane. The (negative) dry air mass perturbation minima to the southwest of the control TC center was in excess of 4 hPa. This uneven dipole pattern, coupled with knowledge of the control simulation track, indicates that the perturbed hurricane intensified and shifted slightly southwestward. This slight shift and intensification is also evident for sea level pressure and 500 hPa geopotential height (not shown) as well as in the EOPs for vertically

averaged potential temperature (Fig. 6.5b), water vapor mixing ratio (Fig. 6.5d), and equivalent potential temperature (Fig. 6.5f). The shift is track northward (southward) for weakening (intensifying) perturbations is seen in periods P2 and P3 (not shown). The conspicuous dipole pattern is curiously not evident in the 850 hPa EOPs for potential temperature or water vapor mixing ratio (Figs. 6.5 c and e). The EOP for the 850 hPa horizontal wind field indicates a perturbation cyclonic vortex center to the southwest centered on the mass perturbation – suggestive of a balanced wind and mass perturbation associated with the evolved EOP. The EOP for both vertically averaged and 850 hPa mixing ratio (Figs. 6.5 d and e) as well as the EOP for equivalent potential temperature (Fig. 6.5f) show banded, dipole structures to the northeast of the TC structures. These are high-θ_e spiral bands (Fig. 6.6b) in the rainband regions (Fig. 6.6a) that have been also shifted southwestward with the TC center, where the spiral bands regions can also be seen in the distribution of precipitable water (Fig. 6.6c). The EOP for equivalent potential temperature (Fig. 6.5f) is consistent with the EOP of potential temperature and mixing ratio by construction and indicates that for this case, and this simulation period, the changes in equivalent potential temperature are primarily due to water vapor mixing ratio perturbations associated with shifts in the spiral bands positions rather than increases in potential temperature in the same region.

3) VERTICAL STRUCTURES OF EOP VARIABLES

Figure 6.7 shows the cross-sections of EOP variables for the +4 KE case. In Fig. 6.7a (cross section orientation indicated in Fig 6.5a), the EOP of perturbation pressure is negative southwest of the hurricane from the lower- to upper-troposphere with maxima near the surface, and positive northeast of the hurricane. The negative EOP is stronger and stretches higher than the positive EOP. This is consistent with the southwestward shift and intensification of the perturbed hurricane. In Fig. 6.7b, the EOP of potential temperature (cross section orientation in Fig. 6.5b) is positive in a column extending throughout most of the troposphere. It is notable that the column is weakest in the lower troposphere at approximately the 850 hPa level where the horizontal maps indicated very little evidence of significant potential temperature perturbation amplitude. There is a faint mid-tropospheric negative potential temperature structure to the northeast of the positive columnar structure. This distribution is consistent (again) with the shift of the warm core of the hurricane. There are banded temperature

perturbation structures elsewhere in the lower-troposphere, which relates to the spiral bands of equivalent potential temperature and precipitable water in the rainband regions. In Fig. 6.7c, the EOP of mixing ratio are mainly in the lower- to mid-troposphere. There are positive maxima of the EOP southwest and northeast of the hurricane, and negative maxima of the EOP next to the positive maxima of the EOP northeast of the hurricane. These structures are consistent with the southwestward shift, since humidity is larger in the rainband regions than in the environment. In Fig. 6.7d, the EOP of equivalent potential temperature have features of both EOP of potential temperature (in the eye) and mixing ratio (in the eye and spiral bands regions removed from the center).

In general, EOP of perturbation pressure is mainly tropospheric in depth with a maximum near the surface. The EOP of potential temperature is located mainly in the cyclone center from lower- to upper-troposphere with maxima in the upper-level outflow. The EOP of mixing ratio is located mostly along the margins of the spiral bands regions from the lower- to mid-troposphere and at the mid-levels over the cyclone center. For this intensifying KE perturbation, all perturbation fields show a signature of a southwestward shift of the hurricane and spiral bands structures.

e. Discussion

In this chapter, we perturbed optimally the initial conditions of nonlinear simulations of Irma over three difference periods and studied how these initial optimal perturbations evolved. The optimal perturbations had the intended intensity impact on the simulations of Irma. Comparing the actual and predicted changes of response function in several cases, we found that perturbations of horizontal winds are more effective than perturbations of temperature and humidity for changing TC intensity, and that weakening cases behave more linearly than intensifying cases. Comparing vertical profiles of normalized EOP and total energy of perturbations at initial and final time, we noticed that EOP of horizontal winds and potential temperature are largest in the upper-troposphere, and total energy of the perturbations increases and propagates upward. We found that the intensified hurricane shifts southward relative to the control track, while the weakened hurricane shifts northward. Finally, the

optimal perturbations rotate cyclonically about the hurricane center in a pattern which resembles a 48h period vortex Rossby wave.

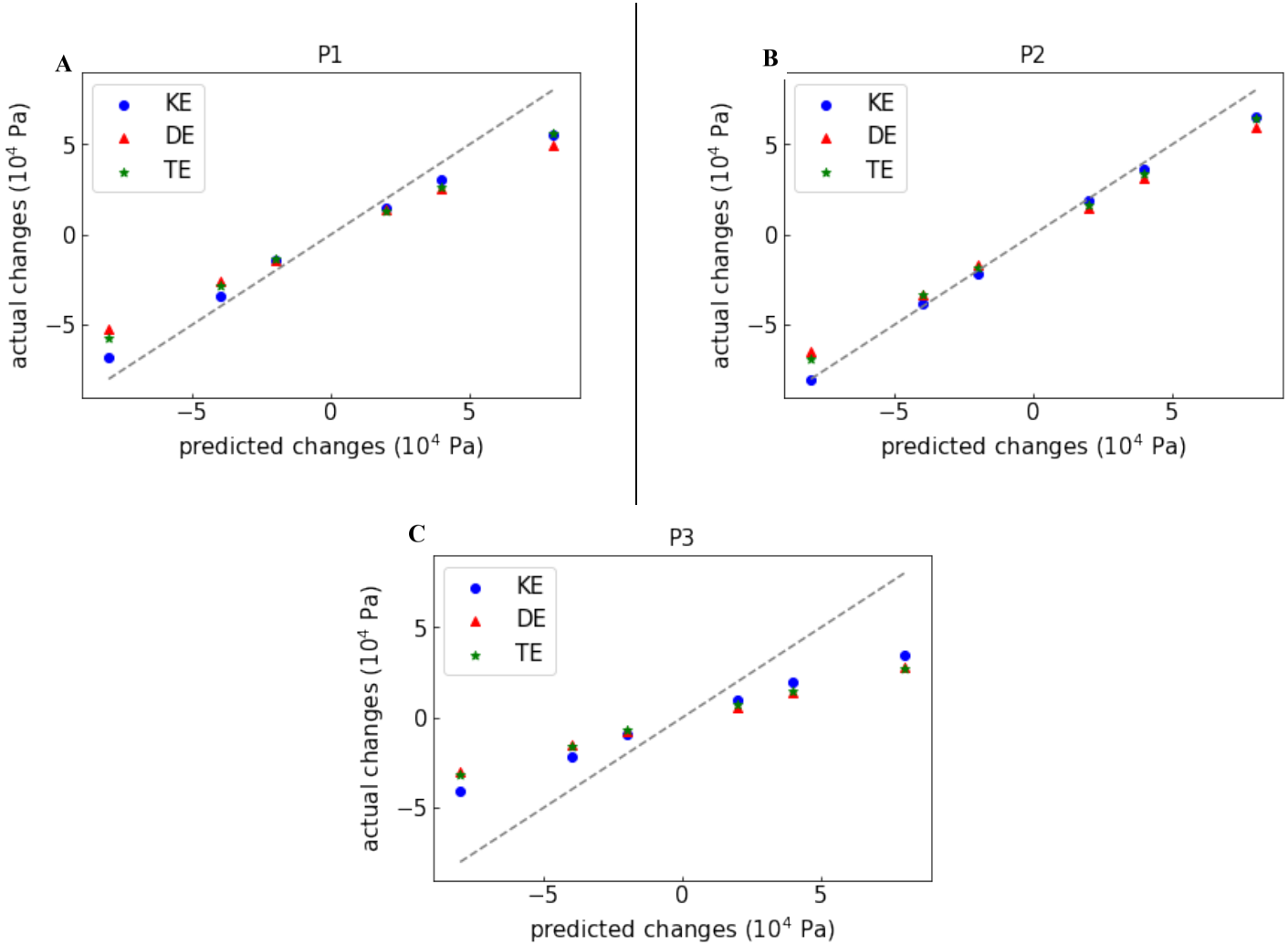

Figure 6.1. The predicted and actual changes of response function for different magnitude of perturbations and for different energy norms (KE: kinetic energy; DE: dry energy; TE: total energy) for (a) P1; (b) P2; (c) P3.

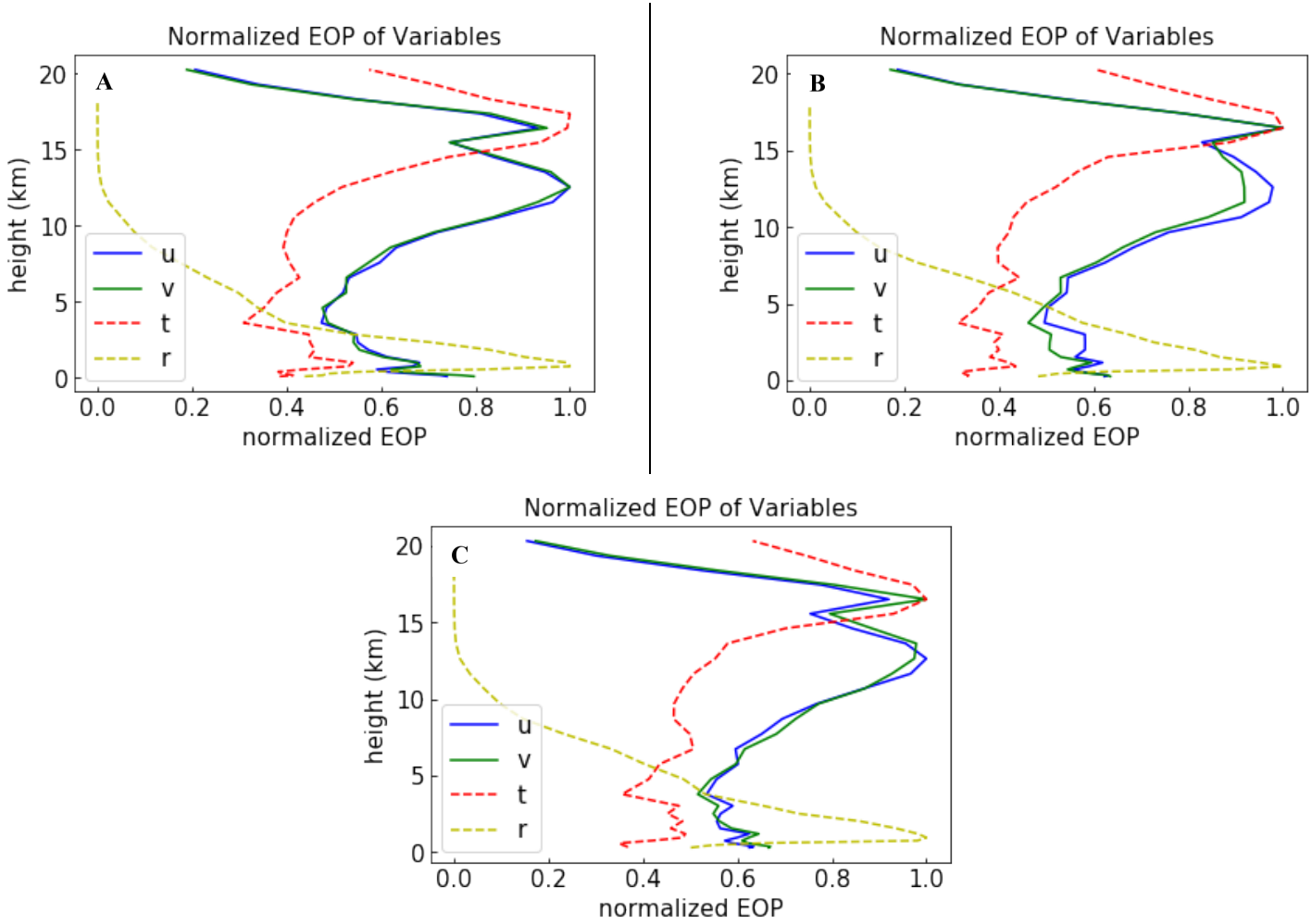

Figure 6.2. Normalized evolved optimal perturbation of zonal wind, meridional wind, potential temperature and mixing ratio after 24h of integration for +40000 Pa kinetic energy optimal perturbation beginning at (a) 0000 UTC 06 September 2017, (b) 0000 UTC 10 September 2017, (c) 0000 UTC 11 September 2017. The u, v, t, r, represent zonal

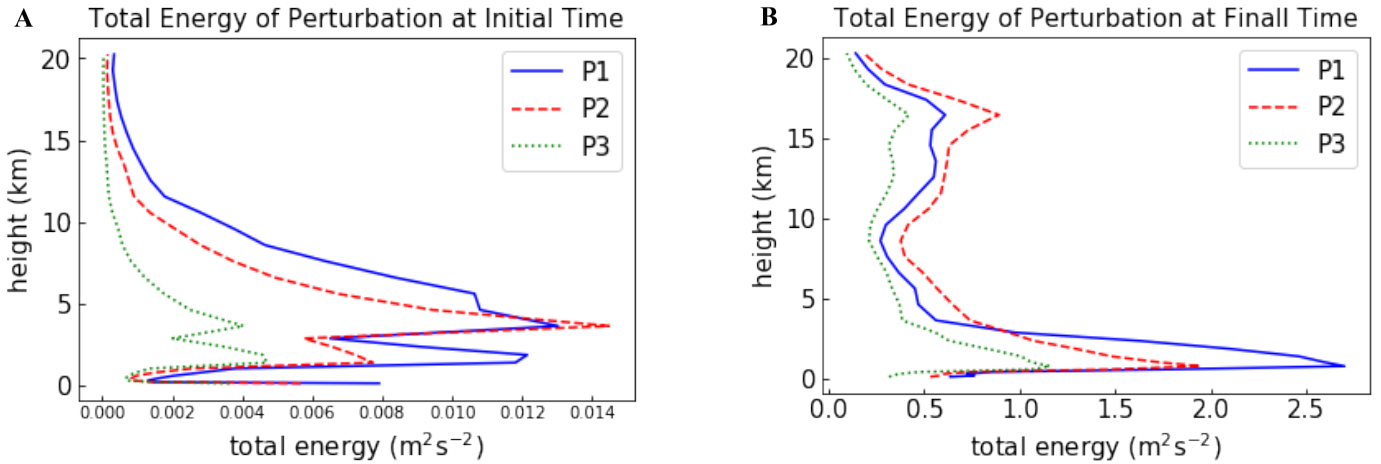

Figure 6.3. Total energy of perturbations for +40000 Pa kinetic energy optimal perturbation at (a) initial time and (b) final time of three 24h periods. The P1, P2, and P3 represent the three 24h periods beginning at 0000 UTC 05, 06, and 10 September 2017 respectively.

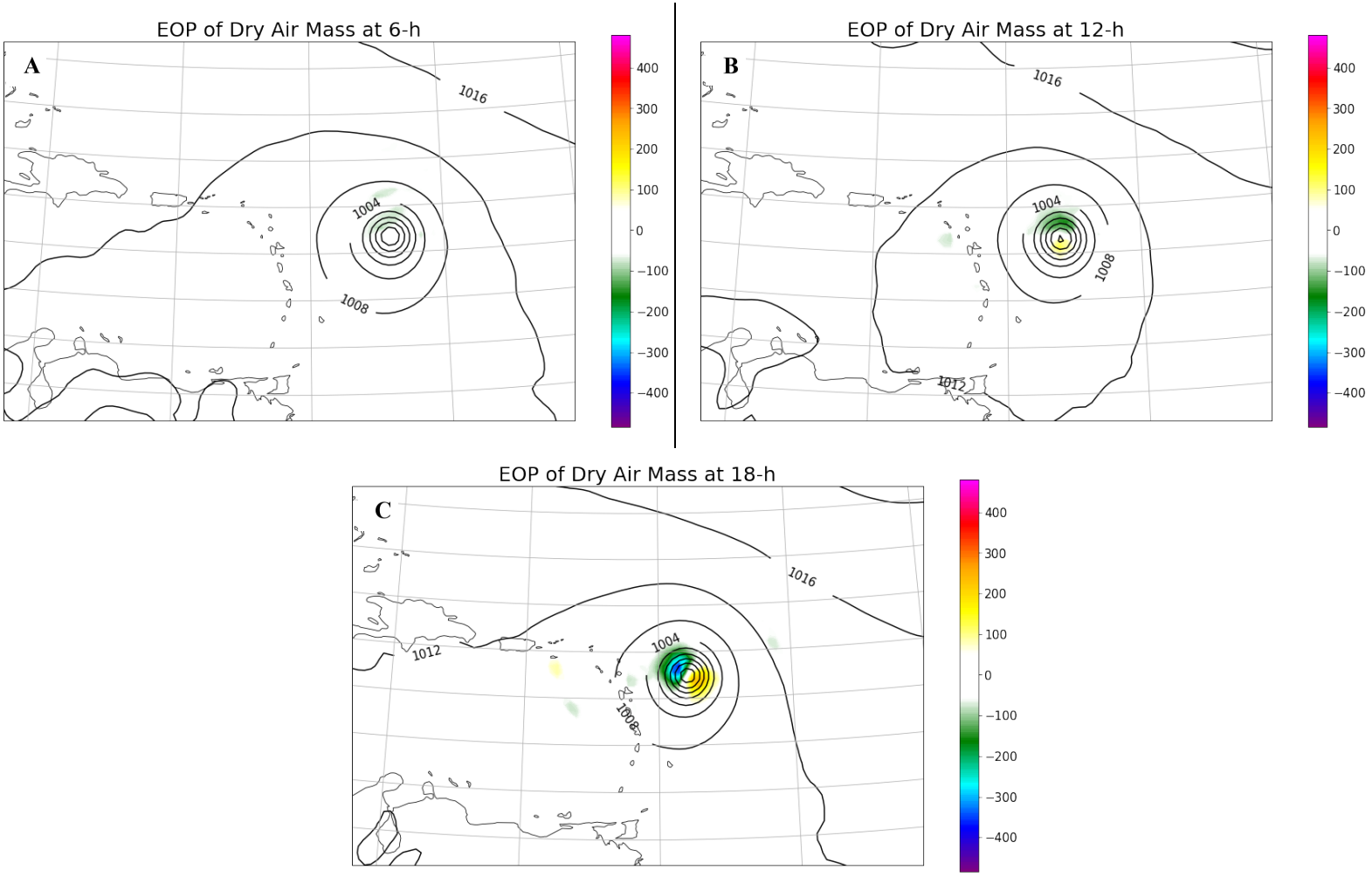

Figure 6.4. Evolved optimal perturbations of dry air mass at (a) 6-h, (b) 12-h, (c) 18-h (color scale with interval every 5 Pa) for +40000 Pa kinetic energy optimal perturbation beginning at 0000 UTC 05 September 2017.

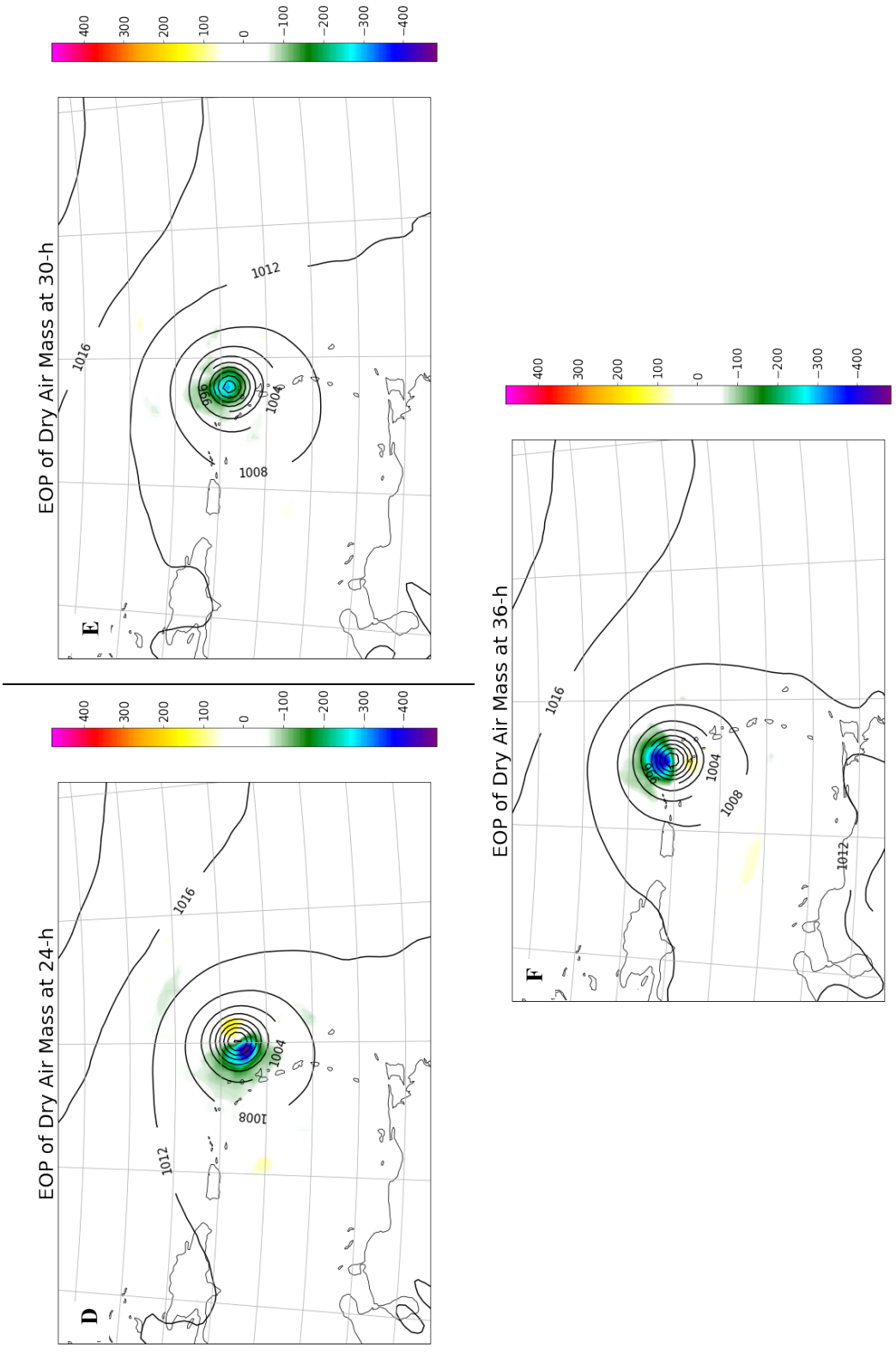

Figure 6.4 continued. As in Figure 6.3a-c, but for (d) 24h, (e) 30-h, (f) 36-h (color scale with interval every 5 Pa).

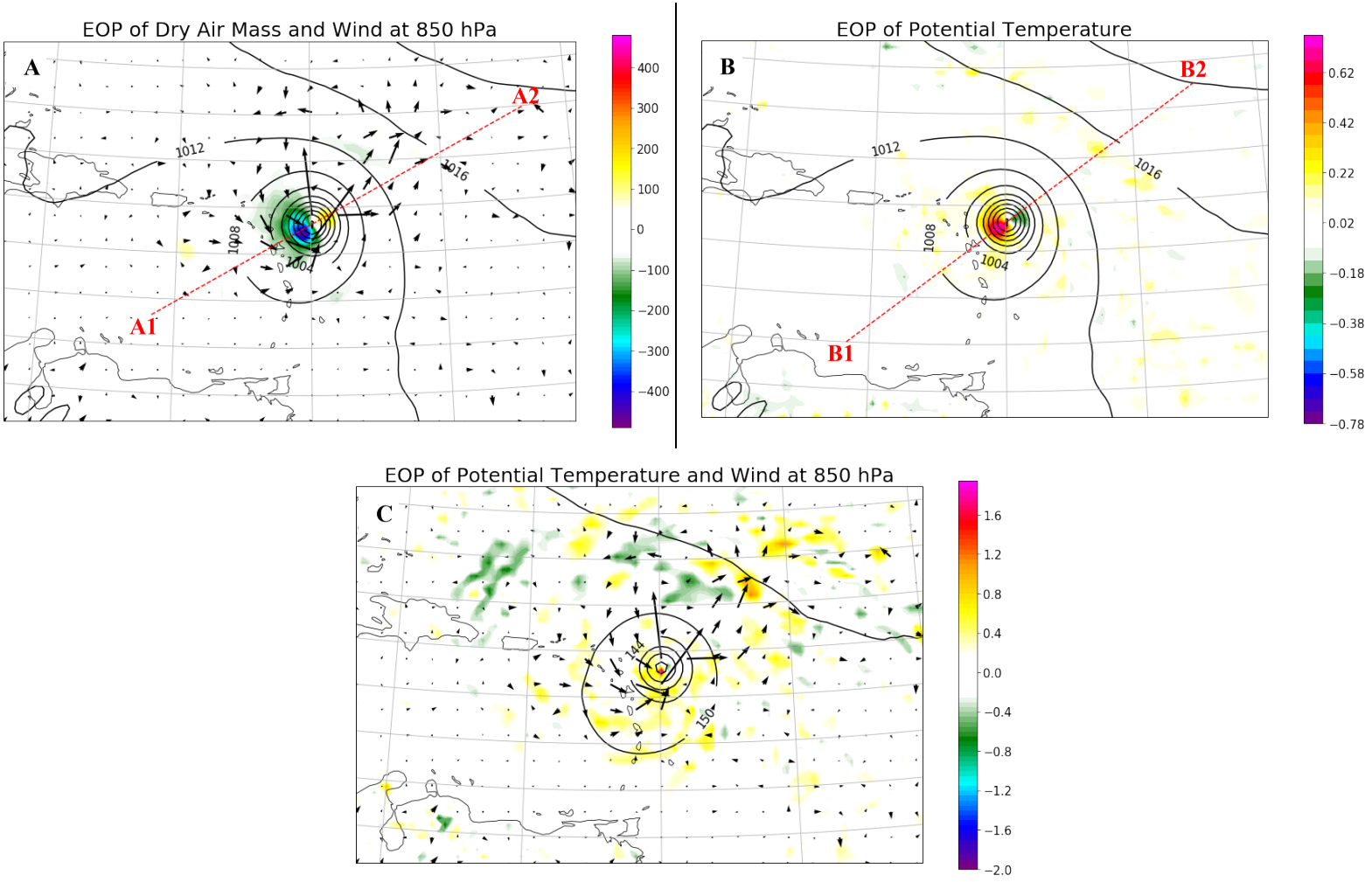

Figure 6.5. Evolved optimal perturbations of (a) dry air mass and wind at 850 hPa (color scale with interval every 10 Pa); (b) vertically averaged potential temperature (color scale with interval every 0.05 k); (c) potential temperature and wind at 850 hPa (color scale with interval every 0.05 k) after 24h integration for +40000 Pa kinetic energy optimal perturbation

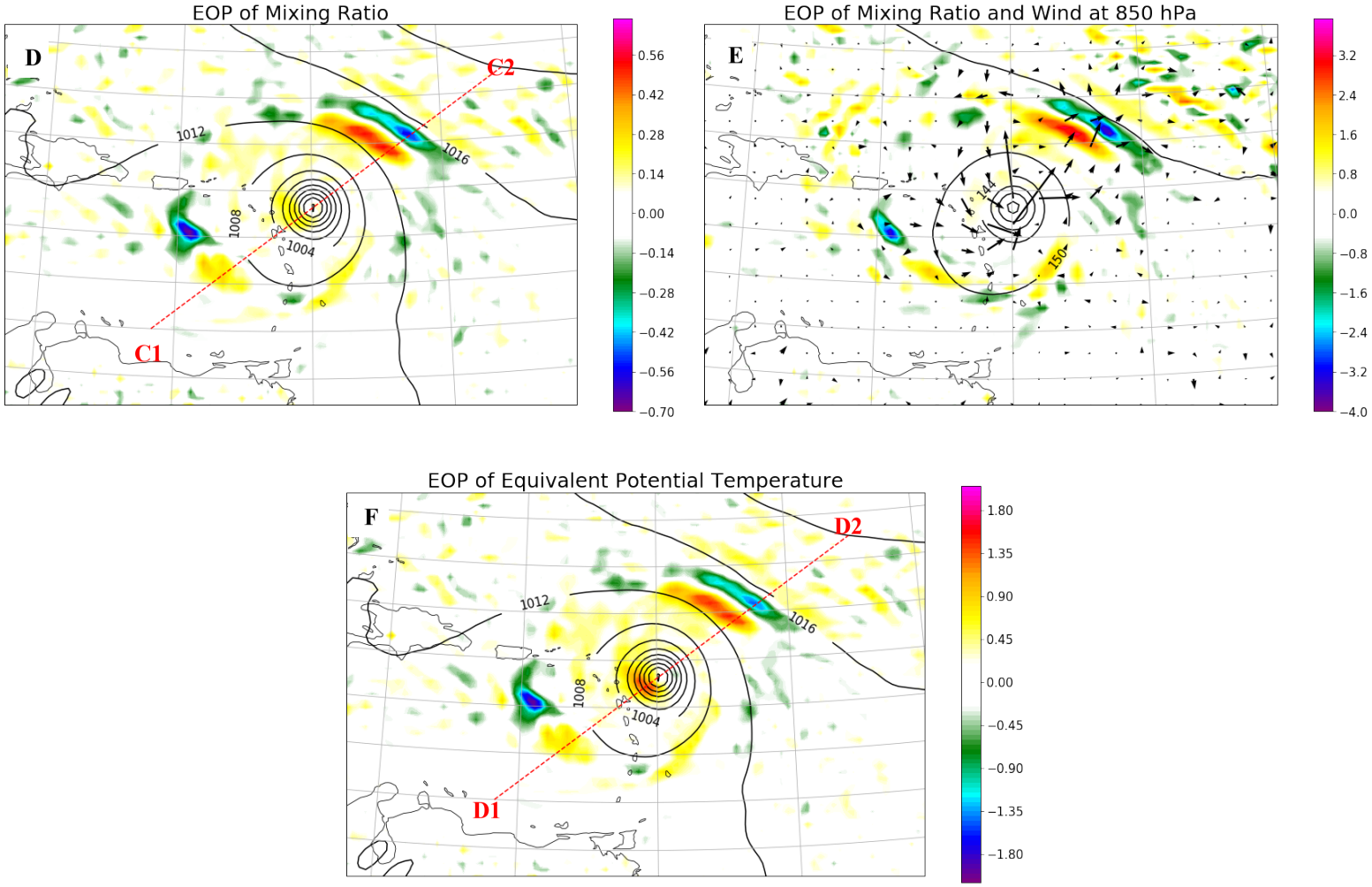

Figure 6.5 continued. As in Figure 6.2a-c, but for (d) vertically averaged mixing ratio (color scale with interval every 0.01 g kg^{-1}), (e) mixing ratio and wind at 850 hPa (color scale with interval every 0.05 g kg^{-1}), (f) vertically averaged equivalent temperature (color scale with interval every 0.05 k).

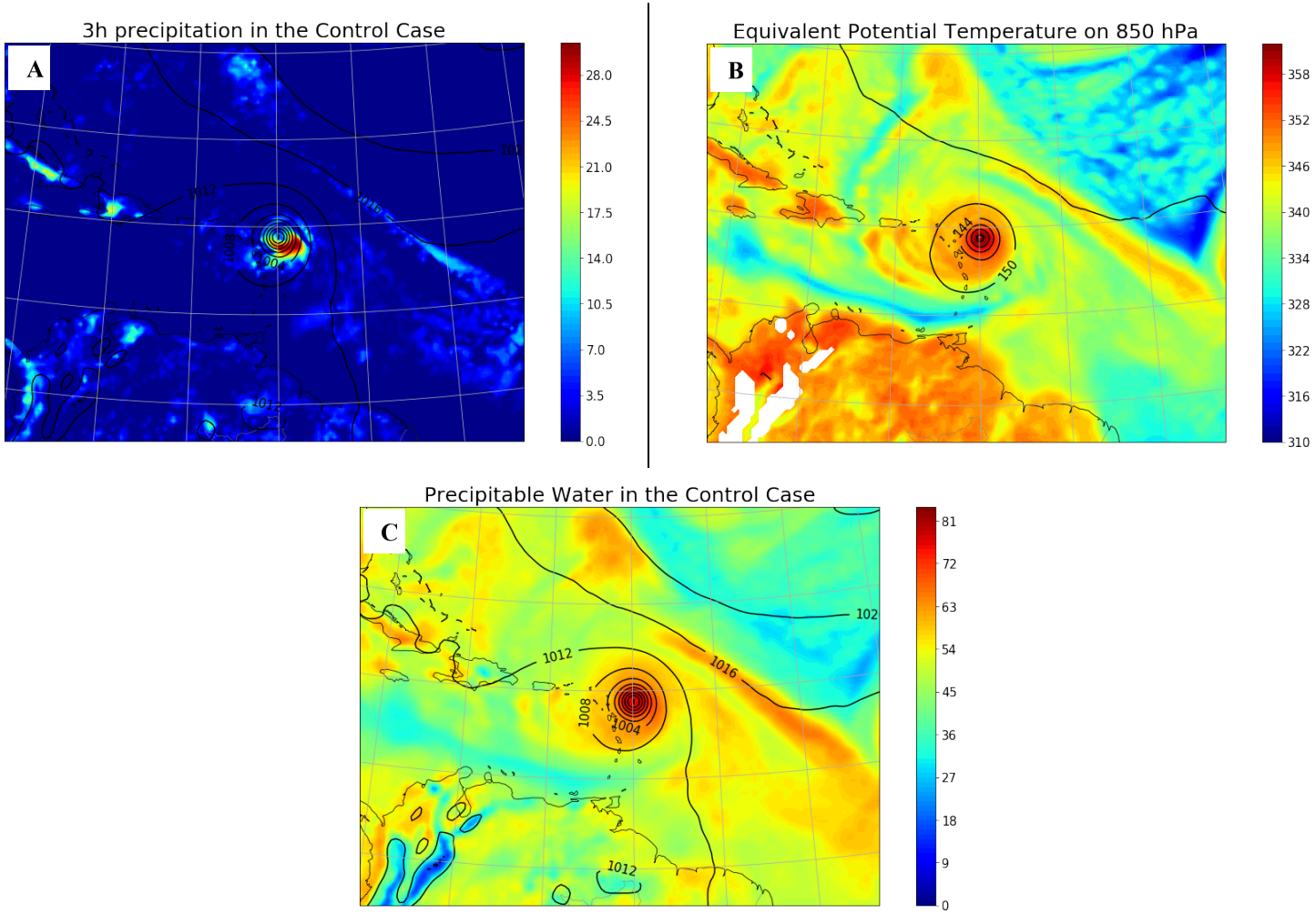

Figure 6.6. Distributions of (a) 3h precipitation (color scale with interval every 0.5 mm), (b) equivalent potential temperature at 850 hPa (color scale with interval every 1 k), (c) precipitable water (color scale with interval every 1.0 kg m^{-2}) of the control case at 0000 UTC 06 September 2017.

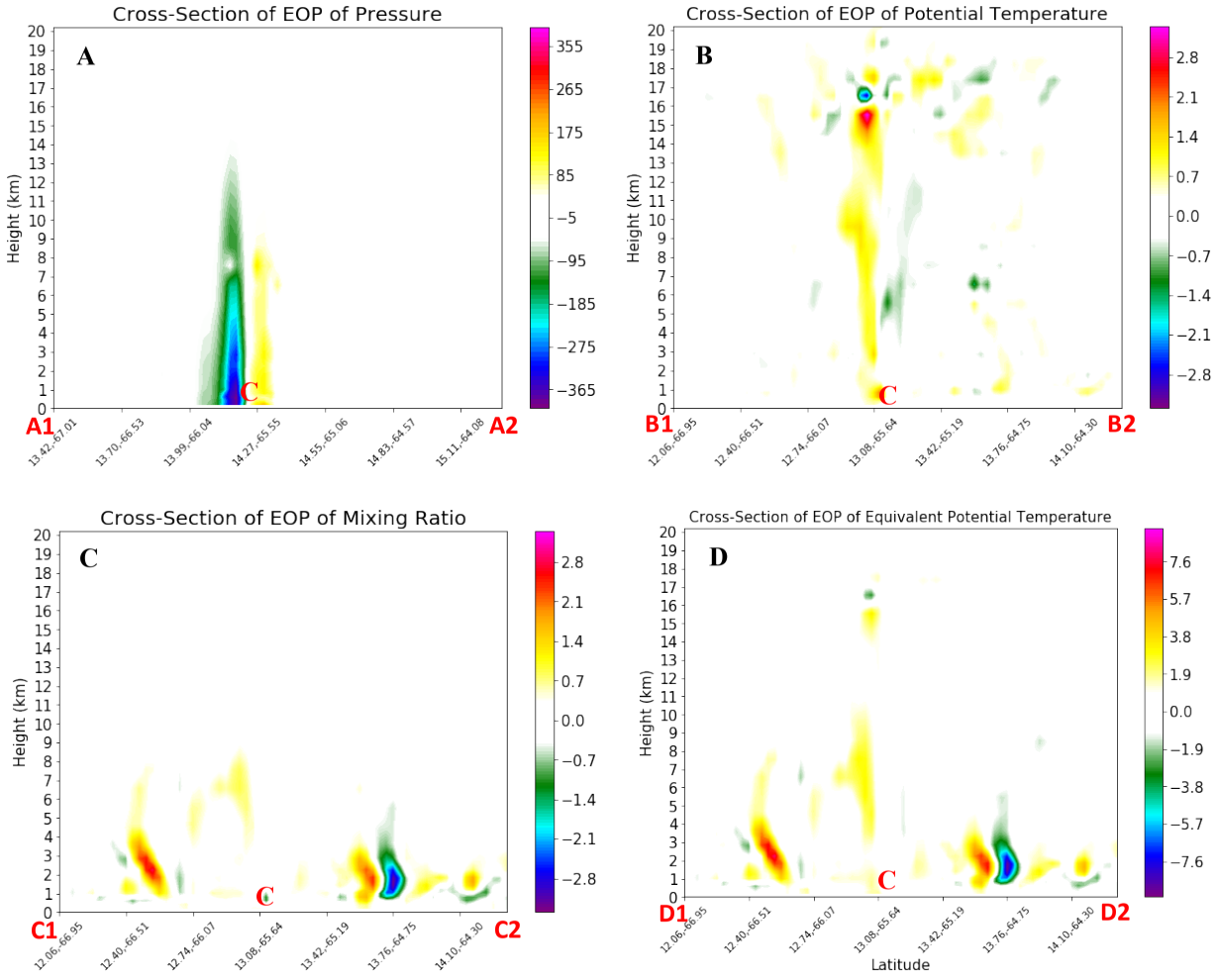

Figure 6.7. Vertical cross-section of evolved optimal perturbations of (a) pressure (color scale with interval every 10 Pa), (b) potential temperature (color scale with interval every 0.05 k), (c) mixing ratio (color scale with interval every 0.05 g kg^{-1}), (d) equivalent potential temperature (color scale with interval every 0.05 k) after 24h of integration for +40000 Pa kinetic energy optimal perturbation beginning at 0000 UTC 05 September 2017. Locations of a-d are shown in Fig. 6.5a, b, d, f respectively.

7. Discussion and summary

The WRF forward model and its adjoint, both contained in WRFPLUS, are used to study 24h adjoint sensitivities of the intensity of Atlantic Hurricane Irma (2017) for three 24h periods beginning 0000 UTC 5, 9, and 10 September 2017. The intensity measure used as a response function in this adjoint study was the 24h mass of dry air (μ) summed over a box centered on the positions of the simulated TC at the end of the three periods. Sensitivities to the horizontal wind, potential temperature, and mixing ratio were considered. The key results are summarized in the following and in Fig. 7.1:

1) *Increasing the primary circulation outside of the radius of maximum winds associated with cyclonic vorticity spiraling anticyclonically back against the vortex would lead to a more intense TC.* The patterns of the sensitivities to tangential wind and vorticity are consistent, and are associated with the type of perturbations that would grow the most in an asymptotically stable inviscid vortex without radial inflow (Nolan and Farrel 1999);
2) *Increasing the secondary circulation will not lead to a more intense TC in 24 hours.* There is some evidence that increasing the secondary circulation will have an impact 3 to 6 hours later, however, longer-term adjoint sensitivities do not reveal a consistent impact; and
3) *Increasing the equivalent potential temperature (θ_e) in eye and in lower- to mid-tropospheric rainband would lead to a more intense TC*. First, increasing θ_e in the eye would increase the buoyancy, then decrease the downdrafts and central pressure; low-level transport and mid-level entrainment of high-entropy eye air from the eye to the eyewall would enhance the convection in the eyewall (Persing and Montgomery 2003, Cram et al. 2007). Second, increasing θ_e in the rainband regions would enhance the convection in the rainbands and inflow above the boundary layer (Fudeyasu and Wang 2011); the enhanced inflow would transport increased entropy eye air to the eyewall and enhance the convection in the eyewall (Emanuel 1991, Riemer et al. 2010), as well as transport higher angular momentum toward the core and spin up the primary circulation in the rainband regions (Persing 2013, Montgomery and Smith 2017).

It is noted that the first two results, concerning increasing the primary circulation outside the radius of maximum wind and the impact of the secondary circulation at the initial time, are at odds with the ensemble sensitivity results of Brown and Hakim (2015) who observed that increasing both the TC primary circulation *at the radius of maximum winds* or the secondary circulation would lead to a stronger cyclone within 24 hours. While the results of the present study should be explored in more cases, the apparent contradiction between this study and that of Brown and Hakim may be related to a weakness of the ensemble sensitivity technique, which is based on correlations between variables. The enhancements of the primary circulation in the eyewall and the secondary circulation are the result of the heating in the eyewall. Specifically, we know that in the eyewall regions an increase of entropy flux from the sea surface (*i.e.* sensible and latent heat fluxes) would enhance the eyewall convection. The heating associated with the eyewall convection drives the secondary circulation as described by the Sawyer-Eliassen equation. The upward transport of angular momentum from the boundary layer and eddy momentum flux increase the primary circulation in the eyewall with the balanced response being a reduction in the central pressure and increase in the inflow, which further enhance the eyewall convection. It is expected, therefore, that the correlations between the hurricane intensity and strength of the primary circulation in the eyewall and the secondary circulation would be large and positive. Furthermore, as the processes described above indicate intensification of a TC over 24 hours is not accomplished by directly enhancing the primary circulation in the eyewall or the secondary circulation.

Adjoint-informed optimal perturbations are used to perturb initial conditions of the nonlinear model. Actual and predicted changes of the response function are in linear relation. We found that perturbations of horizontal winds are more effective than perturbations of temperature and humidity for changes of TC intensity, since predicted and actual changes of response function are the closest in kinetic energy perturbation cases. Weakening the hurricane behaves more linearly than intensifying it, since predicted and actual changes of response function are closer in negative perturbation cases than in positive perturbation cases. Moreover, perturbations of horizontal winds and potential temperature propagate upward, since perturbations of them are largest in the lower-troposphere at initial time, but strongest in the upper-troposphere at later time. The total energy of optimal perturbations also propagates

upward. Comparing the difference of variables in the control and perturbed cases (i.e. evolved optimal perturbations), we found that intensified (weakened) TCs have a southward (northward) shift along the control TC track, and the evolved optimal perturbations rotate around the control TC center which appears to be a 48h period vortex Rossby wave.

While many of the results are consistent with extant research, caution must be exercised in generalizing these results. As a consequence, the universality of the results need to be evaluated by considering additional cases and, and perhaps using other numerical models, like the COAMPS (Hodur 1997, Doyle et al. 2012 and 2014). If they are proven, more complete explanations and theories are needed for these phenomena. For example, the interaction between the mid-latitude trough and the TC is still an enigma, maybe we could perturb the trough by perturbing vorticity in the vicinity of the trough (Komaromi et al. 2011). In addition, we could study these facts in models of higher resolution, especially higher horizontal resolution, and in adjoint models of more complete microphysics, like ice physics. What is more, while adjoint models are typically valid (in terms of linearity) for studies of less than 48h, sensitivity defined in statistical sense (e.g., ensemble sensitivities, Brown and Hakim 2015) may provide additional information about sensitivity of TC intensity for longer times and nonlinear processes. Furthermore, sensitivities to more variables (like heat fluxes and SST) may be beneficial to study dynamics of TC intensity in coupled models (Langland 1995, Ito 2011).

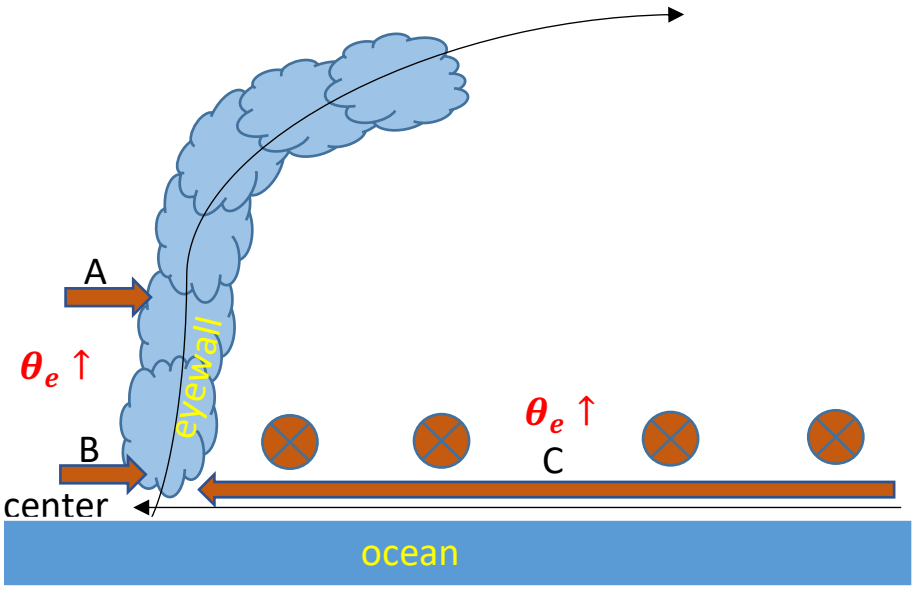

Figure 7.1. Schematic in radius-height coordinates of an axisymmetric TC. The cyclone center is to the left of the figure. The clouds denote the eyewall region, and the blue rectangle indicates the ocean. The black arrows denote the hypothesized path of air parcels in the Carnot cycle. The orange crosses denote increase of the cyclonic tangential wind in the rainband regions. The thick orange arrows denote the entropy (i.e. equivalent potential temperature) fluxes: A denotes mid-level entrainment from the eye to the eyewall, B denotes low-level transport from the eye to the eyewall, and C denotes inflows from rainband regions to the eyewall.

References

Arbogast, P., 1998: Sensitivity to potential vorticity. *Quart. J. Roy. Meteor. Soc.*, **124**, 1605–1615.

Bender, M.A. and I. Ginis, 2000: Real-Case Simulations of Hurricane–Ocean Interaction Using A High-Resolution Coupled Model: Effects on Hurricane Intensity. *Mon. Wea. Rev.*, **128**, 917–946.

Bister, M., and K. A. Emanuel, 1998: Dissipative heating and hurricane intensity. *Meteor. Atmos. Phys.*, **50**, 233-240.

Brown, B. R., and G. J. Hakim, 2015: Sensitivity of intensifying Atlantic hurricanes to vortex structure. *Quart. J. Roy. Meteor. Soc.*, **141**, 2538–2551.

Camp, J.P. and M.T. Montgomery, 2001: Hurricane Maximum Intensity: Past and Present. *Mon. Wea. Rev.*, **129**, 1704–1717.

Cangialosi, J.P., A.S. Latto, and R. Berg, 2018: National Hurricane Center Tropical Cyclone Report: Hurricane Irma (AL112017). https://www.nhc.noaa.gov/data/tcr/AL112017_Irma.pdf.

Charney, J.G. and A. Eliassen, 1964: On the Growth of the Hurricane Depression. *J. Atmos. Sci.*, **21**, 68–75,

Chu, K., Q. Xiao, Z. Tan, and J. Gu, 2011: A forecast sensitivity study on the intensity change of Typhoon Sinlaku (2008). *J. Geophys. Res.*, **116**, D22109.

Cram, T.A., J. Persing, M.T. Montgomery, and S.A. Braun, 2007: A Lagrangian Trajectory View on Transport and Mixing Processes between the Eye, Eyewall, and Environment Using a High-Resolution Simulation of Hurricane Bonnie (1998). *J. Atmos. Sci.*, **64**, 1835–1856.

Demaria, M. and R.W. Jones, 1993: Optimization of a Hurricane Track Forecast Model with the Adjoint Model Equations. *Mon. Wea. Rev.*, **121**, 1730–1745.

Demaria, M. and J. Kaplan, 1994: Sea Surface Temperature and the Maximum Intensity of Atlantic Tropical Cyclones. *J. Climate*, **7**, 1324–1334.

DeMaria, M., 1996: The Effect of Vertical Shear on Tropical Cyclone Intensity Change. *J. Atmos. Sci.*, **53**, 2076–2088.

Doyle, J.D., C.A. Reynolds, C. Amerault, and J. Moskaitis, 2012: Adjoint Sensitivity and Predictability of Tropical Cyclogenesis. *J. Atmos. Sci.*, **69**, 3535–3557.

Doyle, J.D., C. Amerault, C.A. Reynolds, and P.A. Reinecke, 2014: Initial Condition Sensitivity and Predictability of a Severe Extratropical Cyclone Using a Moist Adjoint. *Mon. Wea. Rev.*, **142**, 320–342.

Emanuel, K.A., 1986: An Air-Sea Interaction Theory for Tropical Cyclones. Part I: Steady-State Maintenance. *J. Atmos. Sci.*, **43**, 585–605.

Emanuel, K.A., 1988: The Maximum Intensity of Hurricanes. *J. Atmos. Sci.*, **45**, 1143–1155.

Emanuel, K. A., 1991: The theory of hurricanes. *Annu. Rev. Fluid Mech.*, **23**, 179–196.

Emanuel, K.A., 1995: The Behavior of a Simple Hurricane Model Using a Convective Scheme Based on Subcloud-Layer Entropy Equilibrium. *J. Atmos. Sci.*, **52**, 3960–3968.

Emanuel, K.A., 1995: Sensitivity of Tropical Cyclones to Surface Exchange Coefficients and a Revised Steady-State Model incorporating Eye Dynamics. *J. Atmos. Sci.*, **52**,3969–3976.

Emanuel, K.A., 1999: Thermodynamic control of hurricane intensity. *Nature*, **401**, 665–669.

Emanuel, K., C. DesAutels, C. Holloway, and R. Korty, 2004: Environmental Control of Tropical Cyclone Intensity. *J. Atmos. Sci.*, **61**, 843–858.

Errico, R.M., 1997: What Is an Adjoint Model?. Bull. *Amer. Meteor. Soc.*, **78**, 2577–2592.

Errico, R. M. and K. D. Raeder, 1999: An examination of the accuracy of the linearization of a mesoscale model with moist physics. *Q.J.R. Meteorol. Soc.*, **125**, 169-195.

Fudeyasu, H. and Y. Wang, 2011: Balanced Contribution to the Intensification of a Tropical Cyclone Simulated in TCM4: Outer-Core Spinup Process. *J. Atmos. Sci.*, **68**,430–449.

Gray, W.M., 1975: Tropical Cyclone Genesis. Depart Atmos Sci Paper 234, Colorado State University, Fort Collins, CO, p 121.

Guimond, S.R., G.M. Heymsfield, and F.J. Turk, 2010: Multiscale Observations of Hurricane Dennis (2005): The Effects of Hot Towers on Rapid Intensification. *J. Atmos. Sci.*, **67**, 633–654.

Hack, J.J. and W.H. Schubert, 1986: Nonlinear Response of Atmospheric Vortices to Heating by Organized Cumulus Convection. *J. Atmos. Sci.*, **43**, 1559–1573.

Hart, R., 2006: Hurricanes: A Primer on Formation, Structure, Intensity Change and Frequency. *George C. Marshall Institute*, http://icecap.us/images/uploads/409.pdf.

Hodur, R.M., 1997: The Naval Research Laboratory's Coupled Ocean/Atmosphere Mesoscale Prediction System (COAMPS). *Mon. Wea. Rev.*, **125**, 1414–1430.

Holland, G.J., 1997: The Maximum Potential Intensity of Tropical Cyclones. *J. Atmos. Sci.*, **54**, 2519–2541.

Hoover, B.T. and M.C. Morgan, 2010: Validation of a Tropical Cyclone Steering Response Function with a Barotropic Adjoint Model. *J. Atmos. Sci.*, **67**, 1806–1816.

Hoover, B.T. and M.C. Morgan, 2011: Dynamical Sensitivity Analysis of Tropical Cyclone Steering Using an Adjoint Model. *Mon. Wea. Rev.*, **139**, 2761–2775.

Hoover, B. T., 2015: Identifying a barotropic growth mechanism in east Pacific tropical cyclogenesis using adjoint-derived sensitivity gradients. *J. Atmos. Sci.*, **72**, 1215–1234.

Ito, K., Y. Ishikawa, Y. Miyamoto, and T. Awaji, 2011: Short-Time-Scale Processes in a Mature Hurricane as a Response to Sea Surface Fluctuations. *J. Atmos. Sci.*, **68**,2250–2272.

Jones, S. C., 2000: The evolution of vortices in vertical shear. III: Baroclinic vortices. *Quart. J. Roy. Meteor. Soc.*, **126,** 3161–3185.

Judt, F., Chen, S. S. and Berner, J., 2016: Predictability of tropical cyclone intensity: scale-dependent forecast error growth in high-resolution stochastic kinetic-energy backscatter ensembles. *Q.J.R. Meteorol. Soc.*, **142**, 43-57.

Kleist, D.T. and M.C. Morgan, 2005: Interpretation of the Structure and Evolution of Adjoint-Derived Forecast Sensitivity Gradients. *Mon. Wea. Rev.*, **133**, 466–484.

Kleist, D.T. and M.C. Morgan, 2005: Application of Adjoint-Derived Forecast Sensitivities to the 24–25 January 2000 U.S. East Coast Snowstorm. *Mon. Wea. Rev.*, **133**, 3148–3175.

Komaromi, W.A., S.J. Majumdar, and E.D. Rappin, 2011: Diagnosing Initial Condition Sensitivity of Typhoon Sinlaku (2008) and Hurricane Ike (2008). *Mon. Wea. Rev.*, **139**, 3224–3242.

Langland, R., R. L. Elsberry, and R. M. Errico, 1995: Evaluation of physical processes in an idealized extratropical cyclone using ad- joint sensitivity. *Quart. J. R. Meteorol. Soc.,* **121,** 1349–1386.

Langland, R. H., and R. M. Errico, 1996: Comments on ''Use of an adjoint model for finding triggers for Alpine lee cyclogenesis.'' Mon. Wea. Rev., 124, 757–760.

Langland, R.H., M.A. Shapiro, and R. Gelaro, 2002: Initial Condition Sensitivity and Error Growth in Forecasts of the 25 January 2000 East Coast Snowstorm. *Mon. Wea. Rev.*, **130**, 957–974.

Le Dimet, F.-X., and O. Talagrand, 1986: Variational algorithms for analysis and assimilation of meteorological observations: Theoretical aspects. *Tellus*, **38A**, 97–110.

Malkus, J.S., 1958: On the Structure and Maintainance of the Mature Hurricane Eye. *J. Meteor.*, **15**, 337–349.

Malkus, J.S. and H. Riehl, 1960: On the Dynamics and Energy Transformations in Steady-State Hurricanes. *Tellus*, **12:1**, 1-20.

Miller, B.I., 1958: On the Maximum Intensity of Hurricanes. *J. Meteor.*, **15**, 184–195.

Montgomery, M.T. and J. Enagonio, 1998: Tropical Cyclogenesis via Convectively Forced Vortex Rossby Waves in a Three-Dimensional Quasigeostrophic Model. *J. Atmos. Sci.*, **55**, 3176–3207.

Montgomery, M. T., and R. K. Smith, 2017: Recent developments in the fluid dynamics of tropical cyclones. *Ann. Rev. Fluid Dyn.*, **49**, 541–574.

National Centers for Environmental Prediction/National Weather Service/NOAA/U.S. Department of Commerce. 2015, updated daily. *NCEP GDAS/FNL 0.25 Degree Global Tropospheric Analyses and Forecast Grids*. Research Data Archive at the National Center for Atmospheric Research, Computational and Information Systems Laboratory.

Nolan, D.S. and B.F. Farrell, 1999: Generalized Stability Analyses of Asymmetric Disturbances in One- and Two-Celled Vortices Maintained by Radial Inflow. *J. Atmos. Sci.*, **56**, 1282–1307.

Ooyama, 1982: Conceptual evolution of the theory and modelling of the tropical cyclone. *J. Meteor. Soc. Japan*, **60**, 369–380.

Orr, W, 1907: The Stability or Instability of the Steady Motions of a Perfect Liquid and of a Viscous Liquid. Part I: A Perfect Liquid. *Proceedings of the Royal Irish Academy. Section A: Mathematical and Physical Sciences*, **27**, 9-68.

Palmén, E., 1948: On the formation and structure of tropical hurricanes. *Geophysica*, **3**, 26–39.

Persing, J. and M.T. Montgomery, 2003: Hurricane Superintensity. *J. Atmos. Sci.*, **60**, 2349–2371.

Persing, J., M. T. Montgomery, J. McWilliams, and R. K. Smith, 2013: Asymmetric and axisymmetric dynamics of tropical cyclones. *Atmos. Chem. Phys.*, **13**, 12 299–12 341.

Pielke, R. A., J. Gratz, C. W. Landsea, D. Collins, M. A. Saunders, and R. Musulin, 2008: Normalized hurricane damages in the United States: 1900–2005. *Nat. Hazards Rev.*, **9**, 29–42.

Rappin, E.D., M.C. Morgan, and G.J. Tripoli, 2011: The Impact of Outflow Environment on Tropical Cyclone Intensification and Structure. *J. Atmos. Sci.*, **68**, 177–194.

Riehl, H., 1954: *Tropical Meteorology*. McGraw Hill.

Riehl, H. and J.S. Malkus, 1961: Some Aspects of Hurricane Daisy, 1958. *Tellus*, **13:2**, 181-213.

Riemer, M., M. T. Montgomery, and M. E. Nicholls, 2010: A new paradigm for intensity modification of tropical cyclones: Thermodynamic impact of vertical wind shear on the inflow layer. *Atmos. Chem. Phys.*, **10**, 3163–3188.

Ritchie, E.A. and G.J. Holland, 1997: Scale Interactions during the Formation of Typhoon Irving. *Mon. Wea. Rev.*, **125**, 1377–1396.

Rogers, R., 2010: Convective-Scale Structure and Evolution during a High-Resolution Simulation of Tropical Cyclone Rapid Intensification. *J. Atmos. Sci.*, **67**, 44–70.

Rogers, R.F., P.D. Reasor, and J.A. Zhang, 2015: Multiscale Structure and Evolution of Hurricane Earl (2010) during Rapid Intensification. *Mon. Wea. Rev.*, **143**, 536–562.

Rotunno, R. and K.A. Emanuel, 1987: An Air–Sea Interaction Theory for Tropical Cyclones. Part II: Evolutionary Study Using a Nonhydrostatic Axisymmetric Numerical Model. *J. Atmos. Sci.*, **44**, 542–561.

Schubert, W.H. and J.J. Hack, 1982: Inertial Stability and Tropical Cyclone Development. *J. Atmos. Sci.*, **39**, 1687–1697.

Skamarock, W. C., J. B. Klemp, J. Dudhia, D. O. Gill, D. M. Barker, M. G. Duda, X.-Y. Huang, W. Wang, and J. G. Powers, 2008: A description of the Advanced Research WRF Version 3. *NCAR Tech*. Note NCAR/TN-475+STR, 125 pp.

Smith, R.K., 2006: Lectures on Tropical Cyclones. http://www.meteo.physik.uni-muenchen.de/lehre/roger/Tropical_Cyclones/060510_tropical_cyclones.pdf.

Talagrand, O., and P. Courtier, 1987: Variational assimilation of meteorological observations with the adjoint vorticity equation. I: Theory. *Quart. J. Roy. Meteor. Soc.*, **113**, 1311–1328.

Torn, R.D. and G.J. Hakim, 2008: Ensemble-Based Sensitivity Analysis. *Mon. Wea. Rev.*, **136**, 663–677.

Vigh, J.L. and W.H. Schubert, 2009: Rapid Development of the Tropical Cyclone Warm Core. *J. Atmos. Sci.*, **66**, 3335–3350.

Vukićević, T., and K. Raeder, 1995: Use of an adjoint model for finding triggers for Alpine lee cyclogenesis. *Mon. Wea. Rev*., **123**, 800–816.

Wu, C., J. Chen, P. Lin, and K. Chou, 2007: Targeted Observations of Tropical Cyclone Movement Based on the Adjoint-Derived Sensitivity Steering Vector. *J. Atmos. Sci.*, **64**, 2611–2626.

Wu, C., J. Chen, S.J. Majumdar, M.S. Peng, C.A. Reynolds, S.D. Aberson, R. Buizza, M. Yamaguchi, S. Chen, T. Nakazawa, and K. Chou, 2009: Intercomparison of Targeted Observation Guidance for Tropical Cyclones in the Northwestern Pacific. *Mon. Wea. Rev.,* **137**, 2471–2492.

Zhang, X., X.-Y. Huang, and N. Pan, 2013: Development of the upgraded tangent linear and adjoint of the Weather Research and Forecasting (WRF) model. *J. Atmos. Oceanic Technol*., **30**, 1180–1188.

Zhu, C., R. H. Byrd, P. Lu, and J. Nocedal, 1997: Algorithm 78: L-BFGS-B: Fortran subroutines for large-scale bound constrained optimization. *ACM Trans. Math. Softw.*, **23**, 550–560.